

# Light and Single-molecule Coupling in Plasmonic Nanogaps



**Rohit Chikkaraddy**

Department of Physics  
University of Cambridge

A dissertation submitted for the degree of  
*Doctor of Philosophy*

St. John's College

November 2017



*Dedicated to my parents*



# Declaration

This dissertation is the result of my own research undertaken at the University of Cambridge, United Kingdom and includes nothing which is the outcome of work done in collaboration except specified in the text. This dissertation has not been submitted in whole or part for a degree or other qualification at the University of Cambridge or any other university and does not exceed the prescribed word limit of 60,000 words.

---

Rohit Chikkaraddy



# Acknowledgements

My PhD would not have been possible without the support from several wonderful people. I would like to extend my sincere gratitude to all of them.

First of all, I am extremely thankful to my supervisor Jeremy Baumberg for giving me the opportunity to be a part of his research group at the Nanophotonics Centre. His enthusiasm and constant support for research was a great motivation along the three years of my PhD. I am obliged to him for maintaining an excellent research ambience, providing freedom in choosing research problems and giving quick and constructive feedbacks. His efficiency has always stunned me. I thoroughly enjoyed working with a diverse group of amazing people, who made my stay in and out of the labs unforgettable and joyful.

I am very thankful to Bart, who provided constant help throughout my PhD, be it the fabrication processes or the data analysis, he was always there to help. I express my gratitude to Felix Benz for all the stimulating endless discussions on various topics and for always being there to provide friendly support. I would like to thank William and Yago for constructive dialogues on a wide range of research topics over coffee. A special thanks to Cloudy for proof-reading my thesis. I extend my thanks to Marie-Elena, Hamid, Matthew, Femi, Charlie, Wenting, Sean, Dean, Alexander and Junyang for the joyful hours outside of work.

I have had the opportunity to work with an excellent group of collaborators from in and beyond Cambridge and I am very thankful to all of them. I extremely enjoyed working with Ortwin Hess (Imperial College London, London), Ulrich Keyser (University of Cambridge) and Oren Scherman (University of Cambridge) and their research groups. Special thanks to the people who are involved in this work, notably Vlad, Angela and Nuttawut. Thank you all for our fruitful collaborations and invaluable help to gain a deeper understanding in various topics.

I would like to acknowledge the financial support I received from the Dr. Manmohan Singh scholarship from St. John's College, University of Cambridge. My PhD studies would

## *Acknowledgements*

---

not have been possible without this generous support. It helped me to attend numerous conferences along with a yearly visit to home which I am dearly thankful for. Being a part of the creative graduate community at St. John's College was definitely an enriching experience.

I am deeply grateful to my friend Aswathy for her endless love and support, and I am lucky to have parents who have always supported me to pursue my academic interests and kindled my interest in science.



# Abstract

Plasmonic cavities confine optical fields at metal-dielectric interfaces via collective charge oscillations of free electrons within metals termed surface plasmon polaritons (SPPs). SPPs are confined in nanometre gaps formed between two metallic surfaces which creates an optical resonance. This optical resonance of the system is controlled by the geometry and the material of the nanogap. The focus of this work is to understand and utilize these confined optical modes to probe and manipulate the dynamics of single-molecules at room temperature.

In this thesis, nanogap cavities are constructed by placing nanoparticles on top of a metal-film separated by molecular spacers. Such nanogaps act as cavities with confined optical fields in the gap. Precise position and orientation of single-molecules in the gap is obtained by supramolecular guest-host assembly and DNA origami breadboards.

The interaction of light and single-molecules is studied in two different regimes of interaction strength. In the perturbative regime molecular light emission from electronic and vibrational states is strongly enhanced and therefore is used for the detection of single-molecules. In this regime the energy states remain unaltered, however profound effects emerge when the gap size is reduced to  $<1$  nm. New hybridized energy states which are half-light and half-matter are then formed. Dispersion of these energies is studied by tuning the cavity resonance across the molecular resonance, revealing the anti-crossing signature of a strongly coupled system.

This dressing of molecules with light results in the modification of photochemistry and photophysics of single-molecules, opening up the exploration of complex natural processes such as photosynthesis and the possibility to manipulate chemical bonds.



# List of publications

1. Mapping Nanoscale Hotspots with Single-molecule Emitters Assembled into Plasmonic nanocavities using DNA Origami  
R Chikkaraddy, VA Turek, N Kongsuwan, T de Goor, A Demetriadou, O Hess, UF Keyser, and JJ Baumberg  
*Nano Lett.* 18, 405 (2018)
2. How Ultranarrow Gap Symmetries Control Plasmonic Nanocavity Modes: From Cubes to Spheres in the Nanoparticle-on-Mirror  
R Chikkaraddy, X Zheng, F Benz, LJ Brooks, B de Nijs, C Carnegie, M-E Kleemann, J Mertens, RW Bowman, GAE Vandenbosch, VV Moshchalkov, and JJ Baumberg  
*ACS Photonics* 4, 469 (2017)
3. Strong-coupling of WSe<sub>2</sub> in Ultra-compact Plasmonic Nanocavities at Room Temperature  
M-E Kleemann, R Chikkaraddy, EM Alexeev, D Kos, C Carnegie, W Deacon, A de C de Pury, C Grosse, B de Nijs, J Mertens, AI Tartakovskii, and JJ Baumberg  
*Nat. Commun* 8, 1296 (2017)
4. How Light Is Emitted by Plasmonic Metals  
J Mertens, M-E Kleemann, R Chikkaraddy, P Narang, and JJ Baumberg  
*Nano Lett.* 17, 2568 (2017)
5. Mapping SERS in CB: Au Plasmonic Nano-Aggregates  
C Carnegie, R Chikkaraddy, F Benz, B de Nijs, W Deacon, M Horton, W Wang, C Readman, SJ Barrow, OA Scherman, and JJ Baumberg  
*ACS Photonics* 4, 2681 5, 186 (2017)
6. Near-Field Optical Drilling of Sub- $\lambda$  Pits in Thin Polymer Films  
T Ding, R Chikkaraddy, J Mertens, and JJ Baumberg  
*ACS Photonics* 4, 1292 (2017)

7. Plasmonic Tunnel Junctions for Single-molecule Redox Chemistry  
B de Nijs, F Benz, SJ Steven, DO Sigle, R Chikkaraddy, A Palma, C Carnegie, M Kamp, R Sudhararaman, P Narang, O Sherman and JJ Baumberg  
*Nat. Commun* 8, 994 (2017)
8. Interrogating Nanojunctions Using Ultraconfined Acoustoplasmonic Coupling  
WM Deacon, A Lombardi, F Benz, YVI Redondo, R Chikkaraddy, B de Nijs, M-E Kleemann, J Mertens, and JJ Baumberg  
*Phys. Rev. Lett.* 119, 023901 (2017)
9. Revealing Nanostructures through Plasmon Polarimetry  
M-E Kleemann, J Mertens, X Zheng, S Cormier, V Turek, F Benz, R Chikkaraddy, W Deacon, A Lombardi, VV Moshchalkov, GAE Vandenbosch, and JJ Baumberg  
*ACS Nano* 11, 850 (2017)
10. Suppressed Quenching and Strong-Coupling of Purcell Enhanced Single-Molecule Emission in Plasmonic Nanocavities  
N Kongsuwan, A Demetriadou, Rohit Chikkaraddy, F Benz, V Turek, UF Keyser, JJ Baumberg, and O Hess  
*ACS Photonics* ASAP article (2017)
11. Smart Supramolecular Sensing with Cucurbit[n]urils: Probing Hydrogen Bonding with SERS  
B de Nijs, M Kamp, I Szabo, SJ Barrow, F Benz, G Wu, C Carnegie, R Chikkaraddy, W Wang, W Deacon, E Rosta, JJ Baumberg, and OA Scherman  
*Faraday Discuss.* (2017)
12. Single-molecule Strong Coupling at Room Temperature in Plasmonic Nanocavities  
R Chikkaraddy, B de Nijs, F Benz, SJ Barrow, OA Scherman, E Rosta, A Demetriadou, P Fox, O Hess, and JJ Baumberg  
*Nature* 535, 127 (2016)
13. Single-molecule Optomechanics in 'Picocavities'  
F Benz, MK Schmidt, A Dreismann, R Chikkaraddy, Y Zhang, A Demetriadou, C Carnegie, H Ohadi, B de Nijs, R Esteban, J Aizpurua, and JJ Baumberg  
*Science* 354, 726 (2016)

- 
14. SERS of Individual Nanoparticles on a Mirror: Size Does Matter, but so Does Shape  
F Benz, R Chikkaraddy, A Salmon, H Ohadi, B de Nijs, J Mertens, C Carnegie, RW Bowman, and JJ Baumberg  
*J. Phys. Chem. Lett.* 7, 2264 (2016)
  15. Anomalous Spectral Shift of Near- and Far-Field Plasmonic Resonances in Nanogaps  
A Lombardi, A Demetriadou, L Weller, P Andrae, F Benz, R Chikkaraddy, J Aizpurua, and JJ Baumberg  
*ACS Photonics* 3, 471 (2016)
  16. Polarisation-selective Hotspots in Metallic Ring Stack Arrays  
LJ Brooks, J Mertens, RW Bowman, R Chikkaraddy, A Sanders, and JJ Baumberg  
*Opt. Express* 24, 3663 (2016)
  17. Generalized Circuit Model for Coupled Plasmonic Systems  
F Benz, B de Nijs, C Tserkezis, R Chikkaraddy, DO Sigle, L Pukenas, SD Evans, J Aizpurua, and JJ Baumberg  
*Opt. Express* 23, 33255 (2015)
  18. Unfolding the Contents of Sub-nm Plasmonic Gaps using Normalising Plasmon Resonance Spectroscopy  
B de Nijs, RW Bowman, LO Herrmann, F Benz, SJ Barrow, J Mertens, DO Sigle, R Chikkaraddy, A Eiden, A Ferrari, OA Scherman, and JJ Baumberg  
*Faraday Discuss.* 178, 185 (2015)



# Contents

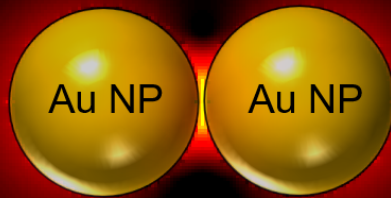
<b>Abstract</b>	<b>ix</b>
<b>1 Outline</b>	<b>1</b>
<b>2 Introduction: Optical Cavities and Molecules</b>	<b>5</b>
2.1 Optics of single-molecules . . . . .	6
2.2 Optical cavities . . . . .	9
2.3 Free electron model for plasmons . . . . .	11
2.4 Introduction to plasmons . . . . .	13
2.4.1 Propagating surface plasmon polaritons . . . . .	15
2.4.2 Localized surface plasmon polaritons . . . . .	16
2.5 Cavity description for plasmonic modes . . . . .	18
2.5.1 Quality factor . . . . .	18
2.5.2 Mode volume . . . . .	19
2.6 Fabricating nanocavities . . . . .	20
2.7 Nanoparticle-on-mirror constructs . . . . .	21
2.7.1 Sensing molecules in the gap . . . . .	22
2.7.2 Effect of nanoparticle size and shape . . . . .	24
2.8 Light-matter coupling . . . . .	27
2.8.1 Weak coupling regime and Purcell effect . . . . .	29
2.8.2 Strong coupling . . . . .	36
<b>3 Supramolecular Assembly and Nano-Optical Spectroscopy</b>	<b>41</b>
3.1 Self-assembled monolayers on metallic surfaces . . . . .	42
3.2 Cucurbit- $[n]$ -uril: Supramolecular host . . . . .	45
3.2.1 Guest-host assembly of CB $[n]$ . . . . .	45
3.2.2 Sample preparation . . . . .	47
3.2.3 Optical properties of the guest-host complex . . . . .	47

3.2.4	Assembly of CB[ <i>n</i> ] on Au surfaces . . . . .	49
3.3	DNA origami . . . . .	51
3.4	Optical nanoscopy . . . . .	52
3.4.1	Dark field spectroscopy . . . . .	54
3.4.2	Electronic and Raman scattering . . . . .	55
3.5	Electromagnetic modelling . . . . .	57
3.5.1	Scattering from NPoM cavities . . . . .	57
3.5.2	Enhanced decay from point dipoles . . . . .	57
3.5.3	Strong coupling from Lorentz absorbing materials . . . . .	58
<b>4</b>	<b>Plasmonic Nanocavity Modes in Ultranarrow Gaps</b>	<b>59</b>
4.1	Need for plasmonic nanocavities . . . . .	60
4.2	Confined waveguide and cavity modes . . . . .	60
4.2.1	Transverse waveguide cavity mode . . . . .	63
4.2.2	Hybridization with antenna mode . . . . .	64
4.3	Nanocube vs Nanosphere-on-Mirror . . . . .	66
4.4	Characterization of nanocavity modes in cube NCoMs . . . . .	68
4.4.1	Symmetry based decomposition of nanocavity modes in NCoMs . . . . .	71
4.5	Variation of gap size . . . . .	72
4.6	Tuning the shape of the nanocavity . . . . .	74
4.7	Figure of merit . . . . .	75
4.8	Conclusion . . . . .	76
<b>5</b>	<b>Single-molecule Surface Enhanced Raman Scattering</b>	<b>77</b>
5.1	Detecting single-molecules . . . . .	78
5.2	Rayleigh and Raman scattering . . . . .	78
5.3	Surface enhanced Raman scattering . . . . .	82
5.3.1	SERS:Electromagnetic and chemical enhancements . . . . .	82
5.4	Single-molecule SERS . . . . .	85
5.4.1	Principal component analysis . . . . .	85
5.4.2	Bianalyte SERS . . . . .	89
5.4.3	Time-resolved SERS . . . . .	91
5.5	Conclusion . . . . .	93
<b>6</b>	<b>Mapping Nanoscale Hotspots using DNA-Origami</b>	<b>95</b>
6.1	Single-emitter in optical cavities . . . . .	96



6.2	Assembly of a single-molecule in NPoM gaps . . . . .	97
6.3	Optical characterization of nanocavities . . . . .	98
6.4	Coherent coupling of NPoM with a single-Cy5 molecule . . . . .	100
6.5	Emission from a single-Cy5 in NPoMs . . . . .	102
6.6	Spatial mapping of local fields . . . . .	104
6.7	Conclusion . . . . .	106
<b>7</b>	<b>Strong Coupling in the Single-molecule Regime</b>	<b>107</b>
7.1	Optical niche for strong-light matter coupling . . . . .	108
7.2	Guest-host chemistry . . . . .	109
7.3	Few molecule strong coupling . . . . .	110
7.4	Single-molecule strong coupling . . . . .	114
7.5	Conclusion . . . . .	116
<b>8</b>	<b>Conclusion and Outlook</b>	<b>117</b>
	<b>Bibliography</b>	<b>123</b>





# 1 Outline

Light is the primary source of energy in our ecosystem. The interaction of light with molecules has an integral role in harvesting light energy. Finding ways to enhance, localize, transport and utilize light at the molecular level is the central theme of this thesis, having immense implications in both fundamental understanding and technological applications. However the way that molecules couple to light is not just inherent to the chemical properties of the molecule. This is highly manipulated by the optical density of states surrounding it. In the context of this thesis, the following questions are addressed:

- ⇒ How to enhance light-molecule interactions at the single-molecule regime?
- ⇒ What are the optimal optical cavity parameters needed to maximise these interactions at room temperature?
- ⇒ How to self-assemble such optical cavities with optimized positions and orientations of molecules within the cavity?
- ⇒ How (and by how much) are the electronic and vibrational scattering rates enhanced in these cavities?
- ⇒ Is the enhancement sufficient to optically address single-molecules?
- ⇒ How to boost cavity-molecule interactions for 'strong' light-matter coupling?

To address these questions, this thesis is divided into seven chapters. To start (**Chapter 2**), a unified figure of merit is defined to allow the comparison of various optical cavity systems. Supporting analytical models are presented to understand light-molecule coupling which are used in later chapters. It is found that the cavities made of plasmonic materials are ideal for addressing single-molecules due to their incredibly low mode volumes. Plasmonic cavities confine optical fields at metal-dielectric interfaces via collective charge

oscillations of free electrons in the metal, termed surface plasmon polaritons (SPPs). In this study nanoparticle-on-mirror (NPOM) cavity is utilized, in which SPPs are highly confined to nanometre sized molecular gaps formed between metallic nanoparticles placed over a metal surface.

**Chapter 3** presents the details of the self-assembly methods used to reliably construct NPOM cavities with gaps  $<5\text{nm}$ . This chapter further discusses the methods utilized to precisely position and orient light-emitting single-molecules into these gaps. Optical fields in the cavity are confined to volumes  $V_m < 100\text{nm}^3$  and are extremely sensitive to the geometrical features and small fluctuations in molecular polarizabilities of different molecules placed in the nanogaps. The techniques for optical characterization of these nanogaps is presented in this chapter. In the following **Chapter 4**, I discuss how changing the nanoparticle shape from sphere to cube in the NPOM geometry alters the coupling of different optical modes resulting in strongly hybridized modes. These optimized modes are used to probe and couple molecular resonance with the optical modes.

The NPOM cavity modes enhance the optical fields by orders of magnitude, a property which is harnessed for the detection of single-molecules through surface enhanced Raman scattering (SERS). **Chapter 5** presents different statistical methods to pin down the signatures of single-molecules in SERS and provides unambiguous proof for single-molecule sensitivity of the NPOM cavity. However the intensity of light emission is strongly dependent on the position of the molecule in the gap, which is addressed in **Chapter 6**. This chapter presents the results of mapping confined fields by precisely positioning a single-molecule at various locations in the gap and quantifying the enhancement of light emission. By measuring the enhancements, the strength of coupling ( $\Omega_R$ ) between the molecule at the optical field maxima is found to be  $\sim 80\text{meV}$ , slightly lower than the NPOM cavity losses. The perturbation in the light scattering by the cavity is monitored by bleaching the single-molecule.

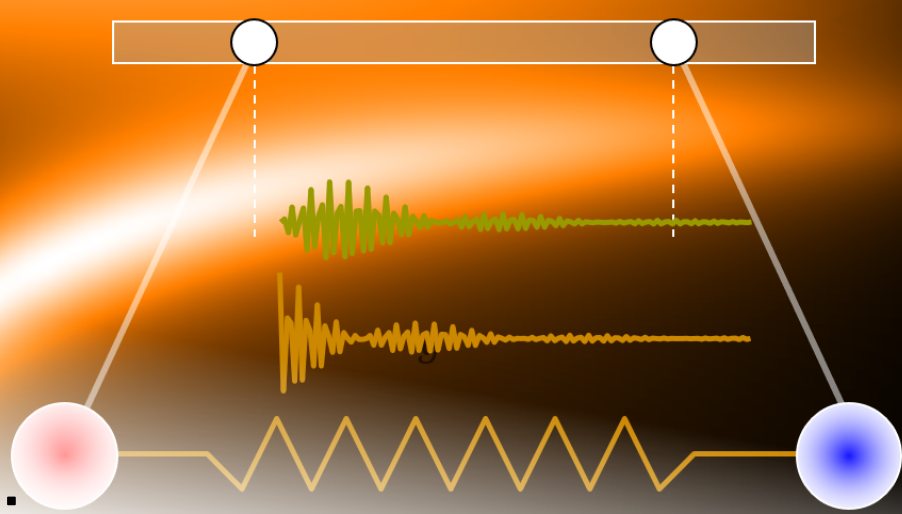
In **Chapter 7**, the coupling strength is increased to values greater than the total losses of the system. This is achieved by decreasing the gap distance to  $<1\text{nm}$  and orientating the molecular dipole along the optical field polarization. This results in the strong coupling regime in which optical and molecular modes are indistinguishable. Moreover, the non-linear increase of  $\Omega_R \propto \sqrt{n}$  is measured by increasing the number of molecules (from  $n=1-10$ ) in the gap via controlled self-assembly.

This work opens new avenues for the manipulation of light-molecule coupling at room temperature and down to the single-molecule level. Such merged aspects of enhanced

---

light extraction and coherent coupling from single-molecules are summarized in **Chapter 8**. This chapter concludes with a discussion on the promising implications of my work for quantum information and quantum photochemistry applications.





## 2 Introduction: Optical Cavities and Molecules

In this chapter, I introduce different optical cavity systems and compare the cavity parameters for optimized light-matter interactions. Plasmonic cavities with narrow gaps ( $<5$  nm) support unique optical modes with ultra-small mode volumes, which can be harvested for coupling with molecules. Such a small round-trip volume makes these cavities potential candidates for useful light-molecule coupling. Here, I present a discussion of the damped coupled harmonic oscillator model to understand the light-molecule coupling, along with a review of relevant works from the literature.

## 2.1 Optics of single-molecules

The question of ‘how to couple, enhance and harness the coupling of light to single-molecules?’ has been a topic of research since the 1950’s when techniques were developed to trap single-atoms and in 1989 optical detection of a single-molecule was demonstrated. Later it was revealed that light can be used not just to probe the natural states of atoms or molecules, but also to change the energy states such that new hybrid energy states will form with appealing quantum properties in both light and matter [1–4]. Before dealing with these hybrid states, first consider the natural energy landscape of a molecule.

Unlike atoms, molecules have complex electronic, vibrational and rotational energy states. The energy levels of a molecule can be described in terms of an energy landscape known as the Jablonsky diagram [5, 6] (Fig. 2.1a). Most of the photophysical properties occur from electronic excitations in which the incident light of energy  $\hbar\omega_i$  excites the molecule to higher electronic states. In most  $\pi$ -conjugated organic molecules, electronic transitions occur in the visible spectrum of light, ranging from 300-800nm. Usually the ground electronic level ( $|S_0\rangle$ ) is filled with paired electron spins resulting in singlet states. The excited state is a spin-preserved singlet state ( $|S_1\rangle$  or  $|S_2\rangle$ ). Depending on how different electronic and vibrational wave-packets are coupled, the relaxation dynamics can be complicated. A typical relaxation process involves (i) fast non-radiative vibronic relaxation ( $v_i^{S_1} \rightarrow v_0^{S_1}$ ) on the timescale of pico-seconds ( $10^{-12}$ s), followed by (ii) a spontaneous radiative decay from the lowest vibrational state in the higher electronic state to the ground electronic state ( $|S_1\rangle^{v_0} \rightarrow |S_0\rangle^{v_i}$ ). This process typically happens on the timescale of nano-seconds ( $10^{-9}$ s) and is termed fluorescence. Apart from this process, an electron in an excited state can undergo spin-flips, resulting in a transition from singlet to triplet state ( $|S_1\rangle \rightarrow |T_1\rangle$ ). The lifetime of  $|T_1\rangle$  is usually 3-4 orders of magnitude longer than the lifetime of  $|S_1\rangle$ . Therefore, the molecule is ‘dark’ when it is in the triplet state. However, certain molecules are highly reactive with oxygen in their  $|T_1\rangle$  state, resulting in the irreversible bleaching of the molecule. All these relaxation processes are also dependent on external environmental factors such as temperature, solvent, and the local ionic environment, which makes processes more complicated. This work deals with the first electronic excitation and its relaxation pathway (as highlighted in grey box of Fig. 2.1a).

The resulting allowed optical transitions can be probed via absorption and emission spectroscopy. At room temperature, the absorption of dye molecules, such as methylene



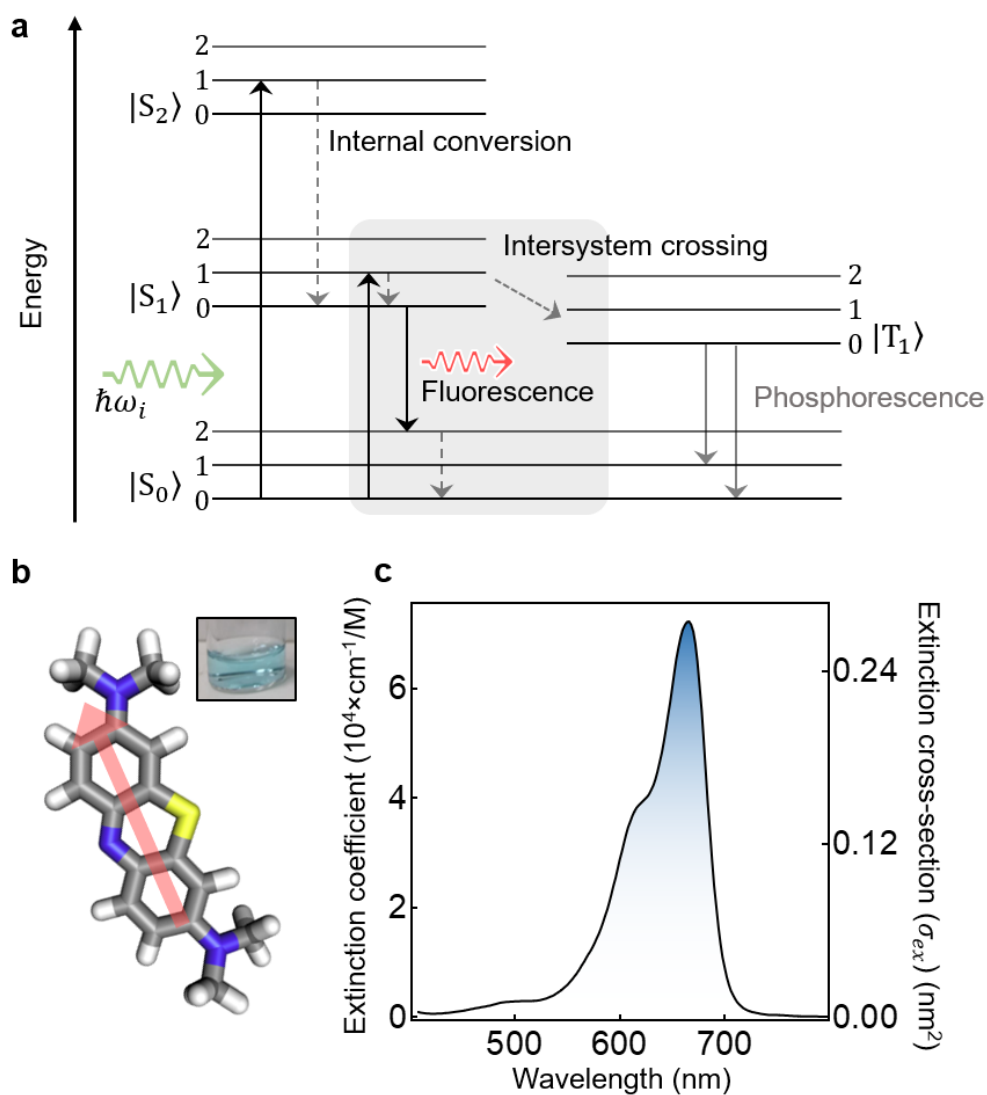


Figure 2.1: **Energy level diagram for molecules.** (a) Jablonsky diagram representing energy relaxation pathways after resonant excitation to higher electronic states. (b) Chemical structure of methylene blue (MB) molecule used in this study. Inset is  $10 \mu\text{M}$  solution of MB in water. (c) Extinction spectrum recorded for MB sample shown in (b).

Table 2.1: Comparing optical transition strengths of different light absorbing materials

Optical System	Dipole moment (Debye)	Exciton size (nm <sup>3</sup> )	Figure of merit ( $\mu/V_e$ )
MB [8]	3.8	1 (1×1×1)	3.80
Cy5 [9]	10.1	2.5 (2.5×1×1)	4.04
<i>J</i> -aggregates [10]	20.5	100 (2× 1× 50)	0.21
Quantum dots (CdSe)[11]	15	125 (5× 5× 5)	0.12
Quantum well (GaAs)[12]	90	25×10 <sup>3</sup> (50×50×10)	3.6×10 <sup>-3</sup>
TMD (WS <sub>2</sub> ) [13, 14]	50	200 (0.5×20×20)	0.25

blue (MB) (chemical structure shown in Fig. 2.1b) is easily detectable by the human eye as a blue colour (10  $\mu$ M solution, Fig. 2.1b inset). However, molecules also scatter/emit light and the probability of such resonant scattering events is proportional to the population in the excited state and the life-time of the excited electronic state. In a simplistic classical description of light-molecule interactions (where the molecule is described as an oscillating point dipole), the scattering cross-section is given by the Abraham-Lorentz equation [7],

$$\sigma_{\text{scat}} = \sigma_{\text{scat}}^0 \frac{\Gamma_s^2}{4\delta^2 + \Gamma_s^2} \quad (2.1)$$

where  $\Gamma_s$  is the total damping rate and  $\delta$  is the detuning between the incident light and the oscillating dipole frequency. The scattering cross-section on resonance ( $\sigma_{\text{scat}}^0 = 3\lambda_0^2/2\pi$ ) depends only on the transition/resonance frequency ( $\lambda_0$ ) of the dipole and is independent of all the other atomic or molecular properties. Therefore this is the maximum achievable scattering cross-section for a single quantum system. The integrated oscillator strength is constant, but the scattering cross-section of the transition is broadened under ambient conditions due to the increased decoherence processes and therefore the peak of the scattering cross-section reduces to smaller values. At room temperature,  $\sigma_{\text{scat}}^0$  is thus scaled down by  $\sim 10^{-6}$  ( $\Gamma_{\text{nat}}/\Gamma_{\text{hom}}$ ), where  $\Gamma_{\text{nat}}$  is the natural (radiative) linewidth and  $\Gamma_{\text{hom}}$  is the homogeneous broadening, which increases due to thermal dephasing thus limiting  $\sigma_{\text{scat}}$  to values  $< 0.2 \text{ nm}^2$ , much smaller than the geometric area of the molecule (Fig. 2.1c).

The transition dipole moment characterizing this optical excitation is given by [15],

$$\mu = \left[ \left( \frac{3}{4\pi^2} \right) \hbar \sigma_{\text{scat}} \gamma_e \varepsilon_0 \lambda_e \right]^{\frac{1}{2}} \quad (2.2)$$

where  $\sigma_{\text{scat}}$ ,  $\gamma_e$  and  $\lambda_e$  are obtained from the experimentally obtained extinction spectrum, respectively corresponding to extinction cross-section, full-width half-maxima of optical resonance at  $\lambda_e$ , resulting in the dipole strength of 3.8 D (=1.27 Cm). In comparison to other strong light emitting molecules with large conjugation length, such as Cyanine-5 dye (Cy5) molecules, MB has a dipole moment which is 2.5 times weaker. For the special class of molecules termed '*J*-aggregates' in which the exciton is delocalized over a large number of molecules (>15), the dipole strength can be as large as 20.5 Debye. However, in the context of this work, the right figure of merit to compare different exciton strengths is the dipole-moment per unit volume of the electronic state (Table 2.1). Molecules have low optical cross-sections compared to inorganic materials such as quantum-wells and 2D transition metal dichalcogenides (TMDs), but they are also much smaller in size. This low optical interaction of molecules with light makes the light-molecule coupling extremely weak at room temperature. To enhance the light-matter interaction requires design of innovative optical cavities with optical fields volumes on the scale of the molecular size, which is discussed in the following section.

## 2.2 Optical cavities

An optical cavity is something that confines light in space typically through multiple reflections. These cavities are essential to effectively couple light with matter (molecules, quantum dots, nitrogen-vacancy centres, etc.). An ideal cavity would confine light for infinitely long times in an infinitesimally small space. Realistic cavities are characterized by two parameters that determine their deviation from such ideal cavities. The first is the quality factor ( $Q$ ) which is proportional to the confinement time in units of optical period and the second is the mode volume ( $V_m$ ) which determines the spatial confinement.

Over the past decade, many optical cavities have been designed to enhance the coupling of single-emitters (Fig. 2.2a), such as planar interfaces [16], near-field probes [17], photonic crystals [18, 19], microcavities [20] and metal nanostructures [21–23]. The

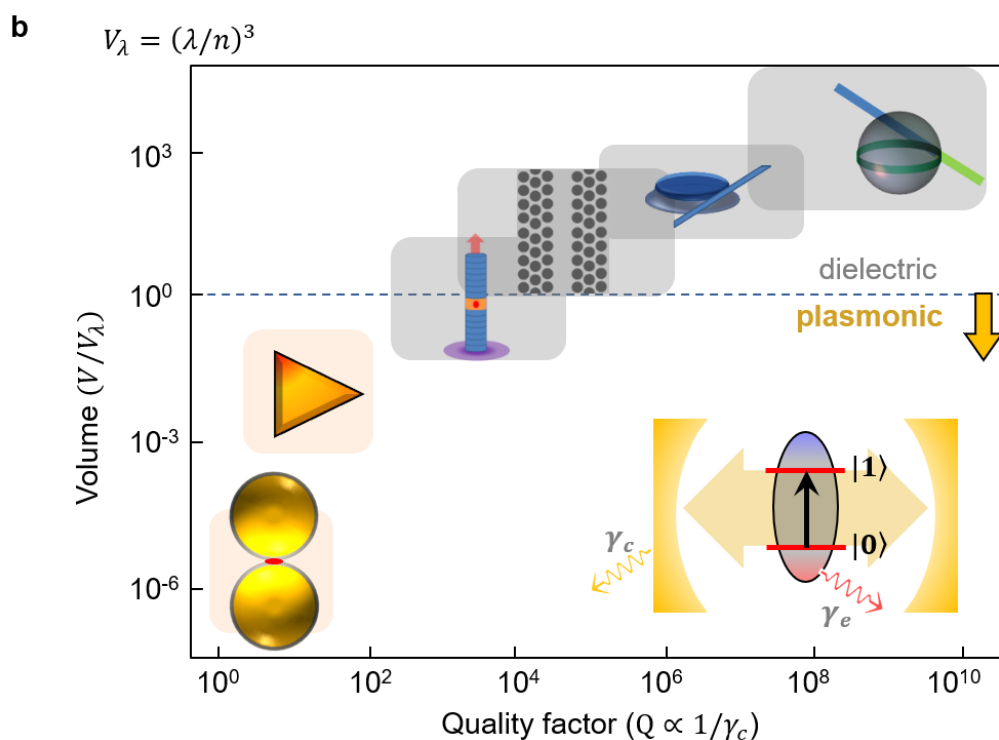
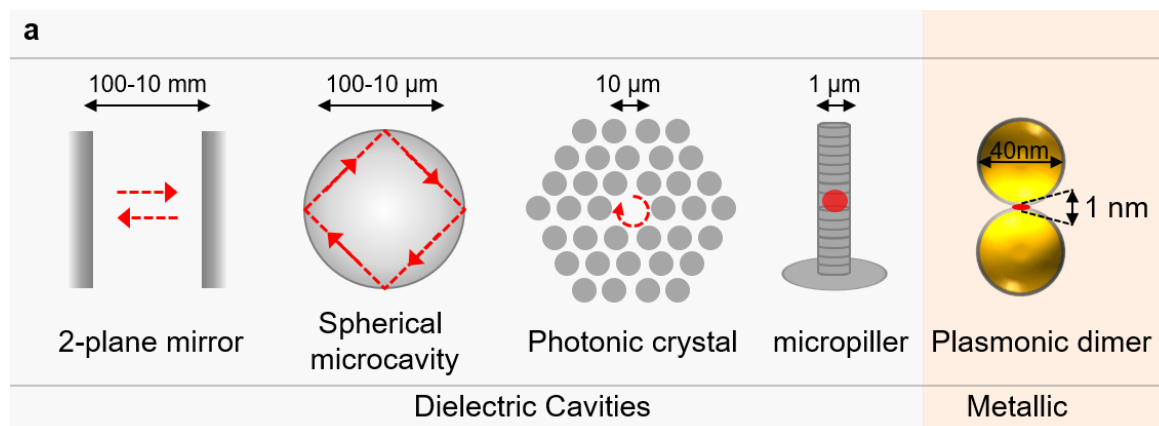


Figure 2.2: **Optical cavities.** (a) Different optical cavities arranged in order of decreasing cavity size. (b) Quality factor,  $Q$ , of a cavity is plotted against its effective volume ( $V/V_\lambda$ ). The icons show realizations of each type of optical cavity: from right, whispering gallery spheres, microdisks, photonic crystals, micropillars, plasmonic nanotriangles and plasmonic nanodimers. Inset shows the coupling of emitter to the cavity with different loss paths.

Table 2.2: Scaling of different optical processes

Optical process	Scaling
Spontaneous emission	$Q/V_m$
Non-linear threshold (lasing)	$Q^2/V_m$
Sensing	$Q/V_m$
Strong light-matter coupling	$Q/\sqrt{V_m}$

rapid development in solid state growth and fabrication techniques allowed the design of optical cavities with  $Q > 10^9$  and cavity volumes reaching diffraction limits ( $V_m/V_\lambda \sim 1$ ; at wavelength  $\lambda$  and refractive index  $n$  with  $V_\lambda = (\lambda/n)^3$ ). Cavities have a variety of applications in modern technology (data storage, integrated optical chips, sensing, lasing, filters etc), however, each of these applications requires different cavity parameters. To choose the correct optical cavity for a particular process, a landscape can be drawn in this plot with appropriate conditions (along with emitter properties) for the right niche. As tabulated in Table 2.2, different aspects of light-emitter coupling have different exponential scaling of cavity parameters. All of these cavities occupy different positions in the  $\log(Q)$  vs  $\log(V_m)$  plot (Fig. 2.2b). In this context, I have found the best niche for strong light-molecule coupling, which I discuss in Chapter 7. In this work, I focus on plasmonic cavities that are unique in comparison to other cavities. Optical field confinement in plasmonic cavities is far beyond the diffraction limited, however  $Q$  is limited to values  $< 100$ . In the following sections, I discuss how plasmons confine light below the diffraction limit, why  $Q$  is  $< 100$  and the rationale behind the choice of plasmonic cavity over dielectric cavity confinement.

## 2.3 Free electron model for plasmons

The optical and conductive properties of a metal are dominated by the electrons in the conduction band. In metals, the conduction band is partially filled and the electrons are relatively free to move within it. The behaviour of these free electrons in the conduction band and the interband excitations of electrons from energetically lower bands to the conduction band determine how the metal interacts with electromagnetic radiation. The properties of the macroscopic light-matter interaction can be described by a complex dielectric function  $\varepsilon(\omega)$ . The conduction band electrons can be treated as a free electron

gas, that gets displaced from their equilibrium position, when they interact with light. This can be considered as a free electron gas moving against a static background of positively charged ions. Upon excitation with light of the correct frequency and momentum, a charge oscillation will be induced in the free electron gas. In a classical picture, this can be described as a harmonic oscillator [24].

$$m^* \frac{d^2x}{dt^2} + m^* \gamma_c \left( \frac{dx}{dt} \right) = -eE \quad (2.3)$$

For an electric field  $E$ , this describes the response of a single electron with charge  $e$ , displacement  $x$  and damping rate  $\gamma_c$ . The fact that electrons are moving in the crystal lattice is taken into account by effective mass  $m^*$ . The displacement of electrons against a positive background leads to a microscopic dipole moment  $p = ex$ . The macroscopic polarization  $P$  considering all the individual dipole moments for  $N$  electrons, assuming that  $x$  and  $E$  has the same time dependence is,

$$P = -ex \left( \frac{N}{V} \right) = -\frac{ne^2}{m^* (\omega^2 + i\gamma_c \omega)} E \quad (2.4)$$

Here,  $n$  describes the electron density (number of electrons  $N$ , per unit volume  $V$ ). The dielectric function  $\varepsilon(\omega)$  can be obtained from  $P$  as,

$$\varepsilon(\omega) = 1 + \left( \frac{P}{\varepsilon_0 E} \right) = 1 - \frac{ne^2}{\varepsilon_0 m^* (\omega^2 + i\gamma_c \omega)} = 1 - \frac{\omega_p^2}{\omega^2 + i\gamma_c \omega} \quad (2.5)$$

The plasma frequency  $\omega_p$  describes the eigenfrequency of harmonic oscillation of a free electron gas in a metal and is characteristic of a given metal. Considering also the background contribution from the bound electrons can be taken as constant for all optical frequencies, therefore, the total dielectric function can be written as,

$$\varepsilon(\omega) = \varepsilon_\infty - \frac{\omega_p^2}{\omega^2 + i\gamma_c \omega} \quad (2.6)$$

The polarization of a metal at frequencies much larger than the plasma frequency is expressed in the parametric value  $\varepsilon_\infty$ , due to a filled d-band below the conducting s-band. For noble metals, interband transitions (below  $\sim 500$  nm for gold) result in increased

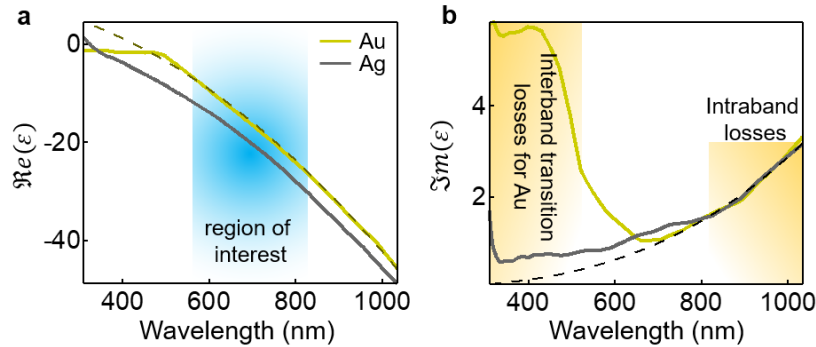


Figure 2.3: **Dielectric function.** (a) Real and (b) imaginary parts of the dielectric function for gold and silver, highlighting the wavelength of interest for this study (blue region in (a)).  $\Re\epsilon(\epsilon)$  and  $\Im m(\epsilon)$  for Au is fitted with Drude-Lorentz model (dashed black line in (a) and (b)). The Drude parameters for Au are  $\epsilon_\infty=9.5$ ,  $\hbar\omega_p=8.97$  eV and  $\hbar\gamma_c=0.069$ eV.

absorption. This Drude-Lorentz model does not take into account interband transitions and hence is limited to longer wavelengths. Fig. 2.3 shows a comparison of the real and imaginary parts of the dielectric function for gold from the experimental data taken by Johnson and Christy [25, 26] with a fit from the Drude-Lorentz model [24]. For the wavelengths of interest in this thesis (region highlighted in Fig. 2.3a), this model serves as a reasonable approximation.

The losses in the system are determined by the  $\Im m(\epsilon)$  part. In the wavelengths of interest, gold possesses the lowest interband and intraband losses (similar for silver). Due to the negative values of  $\Re\epsilon(\epsilon)$ , light does not penetrate into the metals and therefore they are highly reflective. This results in localized charge oscillations on the metal surface, which are discussed in the next section.

## 2.4 Introduction to plasmons

Fundamental limits on the confinement of light given by the classical diffraction limit has been a huge limitation in conventional cavities, especially when the size of the emitter is 100-1000 times smaller than the round-trip of photons in the cavity. However, over the past decade it has become evident that evanescent fields supported by negative refractive index metals can overcome the diffraction limit and confine light fields on the nanometre scale. This is possible due to the collective oscillations of free electrons excited by light, termed surface plasmon polaritons (SPPs) (Fig. 2.4). Surface plasmon polaritons come under the wider class of surface modes in which the interaction between light and matter

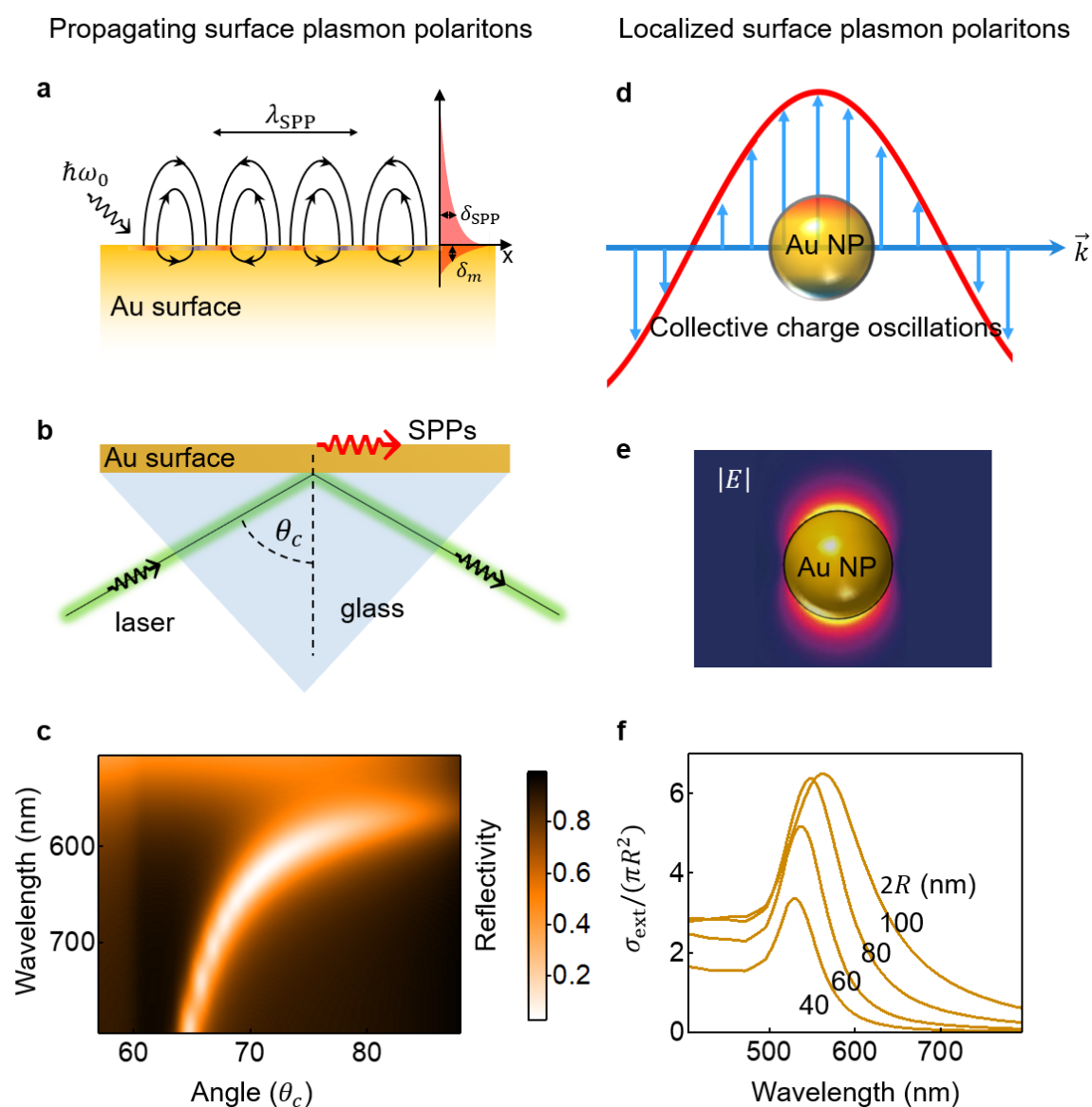


Figure 2.4: **Localized and propagating modes in plasmonic nanostructure.** (a) Schematic interaction of a metal film with light and (b) the propagation of SPP modes on the metal film excited via Kretschmann configuration. (c) Dispersion of SPPs on a 50 nm Au film on glass substrate, with outside environment being water. Calculations are based on solving Fresnel's equation for TM waves in Kretschmann configuration. (d) Schematic representation of metal nanosphere interacting with light and (e) the associated field distribution. The maximum field enhancement ( $E/E_0$ ) near the interface is  $\sim 8$ . (f) Extinction spectrum for different size Au NP is normalized to the geometric area of the nanoparticle, calculated from 3D finite-domain time-difference (FDTD) simulation in water medium.



leads to the possibility of a bound surface mode, such as surface phonon polaritons [27] and surface exciton polaritons [28]. In the context of this work, I will focus on SPPs. There are two fundamental modes of excitation associated with SPPs; (i) propagating surface plasmon polaritons (Fig. 2.4 a-c), in which charge oscillations travel across a metal-dielectric interface, (conventionally termed as SPPs) and (ii) localized surface plasmon polaritons (LSP), where modes are spatially confined (Fig. 2.4 d-f). This confinement is seen in metallic nanostructures of various shapes (spheres, rods, discs, prisms, cubes etc.). Generally, localized modes are harnessed for sensing purposes, whereas propagating modes find their utility in signal transportation. Both these modes exhibit the following two properties which makes plasmon polaritons interesting for coupling with molecules [29]:

1. Near-field: confinement and enhancement
2. Far-field: scattering and directional emission

### 2.4.1 Propagating surface plasmon polaritons

SPPs are propagating optical fields bound to a metal-dielectric interface. However, the dispersion of these modes does not allow direct coupling with freely propagating light. The dispersion relation is given by [24],

$$K_{\text{SPP}} = \frac{\omega}{c} \sqrt{\frac{\varepsilon_1 \varepsilon_2}{\varepsilon_1 + \varepsilon_2}} \quad (2.7)$$

where  $\varepsilon_1$  and  $\varepsilon_2$  are the frequency-dependent relative permittivities of the two media, metal and dielectric respectively. This mis-match in the wave-vector condition can be fulfilled by prism coupling in which evanescent fields at the dielectric interface excite the plasmon polaritons. Various techniques have been developed to effectively excite SPPs such as coupling with gratings, near-field coupling with fiber or emitters, and non-linear coupling.

This dispersion of SPPs is generally mapped in Kretschmann configuration [30] (a common prism coupling techniques), in which the evanescent field produced by total internal reflection is coupled to the metal film in contact above the prism (Fig. 2.4a-b). By adjusting the angle of incidence, the in-plane wavevector of the evanescent field is matched with that of the SPP mode. The SPP excitation is clear from the dip in reflection and calculations for one such Au film system are shown in Fig. 2.4c. The dispersion is similar

to that of free space light at low frequency, but at high frequencies, dispersion bends and reaches the asymptotic limit indicating strong field confinement.

## 2.4.2 Localized surface plasmon polaritons

Another mode of surface plasmon excitation is a confined field around a metallic nanostructure. The curvature of the nanostructure itself enables the direct excitation of this mode. Again the near field properties such as confinement and enhancement of optical fields are associated with the fact that plasmon modes are bound to the interface of metal-dielectric nanostructures. For example, the optical near-field distribution of a single gold nanosphere (Au NP) immersed in water is shown in Fig. 2.4e. The optical resonances of this system are obtained from full-wave finite-domain time-difference (FDTD) simulations. The field strength decays exponentially into the surrounding media. The decay length into the dielectric medium for LSP modes is considerably smaller than the SPP modes [31, 32]. The confinement of the optical field to the proximity of the surface is evident from the evanescent nature of the field. Field distributions around the nanostructure strongly depend on the geometry of the nanostructure.

The coupled oscillations of free electrons and light are generally treated as electromagnetic dipoles, which coherently radiate light at the frequency of the charge oscillations, giving rise to far-field scattering. The typical cross-sections are larger than the geometric area of the nanostructure itself, and are orders of magnitude greater than the absorption for any known molecule. For simple spherical nanoparticles, scattering and absorption cross-sections are given by [24],

$$\sigma_{\text{scat}} = \frac{8\pi}{3} k^4 R^6 \left| \frac{\varepsilon_1 - \varepsilon_2}{\varepsilon_1 + 2\varepsilon_2} \right|^2 = \frac{k^4}{6\pi} |\alpha_1|^2 \Rightarrow \sigma_{\text{scat}} \propto \frac{R^6}{\lambda^4} \quad (2.8)$$

$$\sigma_{\text{abs}} = 4\pi k R^3 \Im \left\{ \frac{\varepsilon_1 - \varepsilon_2}{\varepsilon_1 + 2\varepsilon_2} \right\} = k \Im \{ \alpha_1 \} \Rightarrow \sigma_{\text{scat}} \propto \frac{R^3}{\lambda} \quad (2.9)$$

Here  $\alpha_1$  is the dipolar polarizability of a metallic nanoparticle of radius  $R$ , and  $\varepsilon_1, \varepsilon_2$  are the frequency dependent relative permittivities of the metal and the surrounding dielectric respectively. Wavevector ( $k$ ) is related to the frequency ( $\omega$ ) and the speed of light in vacuum ( $c$ ) as  $k = \omega/c$ . It is important to note that, for plasmonic nanoparticles with dimensions greater than 20 nm, scattering cross-sections dominate and their absorption

cross-sections can be neglected, whereas for those with dimensions less than 5 nm, absorption cross-sections dominate and scattering is negligible.

Furthermore, scattering by plasmonic nanostructures can be uniquely tuned and modified either by the geometry of the nanostructure or by organising nanostructures into the desired architecture. Some structures are designed to achieve omni-directional light scattering. Such unique properties are studied under the title of ‘plasmonic antennae’ [23], which has gained relevance in the channelling of single-photons at desired angles for efficient collection and quantum processing.

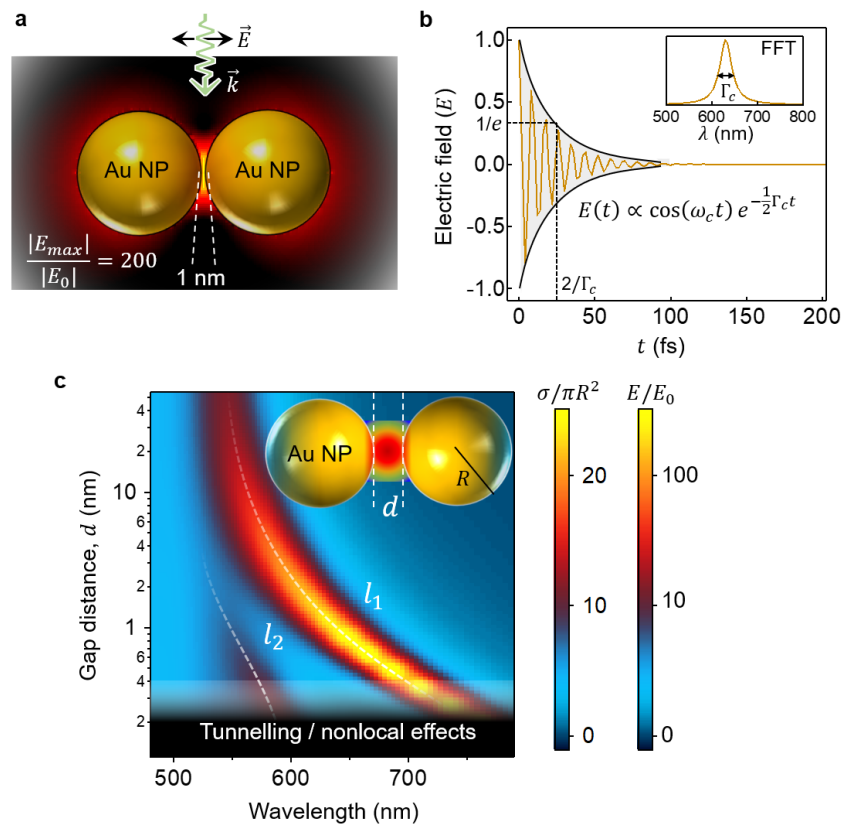


Figure 2.5: **Plasmonic nanodimer cavity.** (a) Spatial distribution of electric field enhancement in an Au plasmonic dimer system with 1 nm gap, obtained from full-wave FDTD simulation at bonding dipolar plasmon resonance ( $l_1$ ) at 650 nm. (b) Temporal decay of the optical-fields in the gap, which is used to estimate the quality factor. (c) Wavelength dependent normalized extinction cross-section of plasmonic nanocavity modes for different gap sizes. The colour scale in the inset indicates the field map.

## 2.5 Cavity description for plasmonic modes

A single nanostructure provides significant field enhancement ( $E/E_0 \sim 10$ ) and confinement ( $V_m \sim R^3, V_m/V_\lambda \sim 10^{-2}-10^{-3}$ ) of fields surrounding the nanostructure [33, 34]. However, significant improvement in near-field intensities is obtained from nanoparticle dimers, where plasmonic resonances from each nanoparticle hybridize to form a bonding dipolar mode ( $l_1$ ) which confines fields into the gap between the nanostructures (Fig. 2.5a). This in-phase dipole-dipole coupling results in a lowering of the plasmon resonance energy, whereas out-of-phase coupling results in a higher energy mode which is generally 'dark' and optically inaccessible in the far-field. Associated with this confinement is an enhancement in the strength of the electric field adjacent to the surface. With appropriate geometries of nanostructures, near-field enhancements can be made as high as  $10^2-10^4$  with spatial confinements as low as  $10 \text{ nm}^3$ . How to extract and quantify cavity parameters  $Q$  and  $V_m$  is discussed in the following section.

### 2.5.1 Quality factor

The quality factor  $Q$ , in simple terms measures the rate at which the optical energy decays from the cavity due to losses such as absorption, scattering or leakage. This can be quantitatively expressed as the ratio of energy stored inside the cavity to the energy loss per oscillation cycle.

$$Q = 2\pi \frac{u(t)}{-\left[\frac{du(t)}{dt}\right]T} = \frac{2\pi}{\Gamma_c \cdot T} = \frac{\omega_c}{\Gamma_c} \quad (2.10)$$

Here,  $u(t) \propto e^{(-\frac{1}{2}\Gamma_c t)^2}$  is the energy density and  $\Gamma_c$  is the decay time, with  $-\frac{du(t)}{dt} \propto \Gamma_c e^{\Gamma_c t}$  being the decay of energy density, and  $\omega_c$  is the resonant frequency. For a plasmonic nanodimer cavity, these decay rates are dominated by the material absorption losses (Joule heating) and radiative scattering rates. They can be estimated by monitoring fields in the gap using time domain simulations. Here I use FDTD simulations (Fig. 2.5b). This time-domain response is equivalently represented in the frequency domain via Fourier transforms (Fig. 2.5b inset). Here  $Q$  is experimentally extracted from the linewidths and resonance frequency obtained through scattering spectroscopy.

The extinction spectrum for an Au dimer (with  $2R=40 \text{ nm}$ ) is obtained from FDTD simulation for various gap sizes,  $d$  (Fig. 2.5c). The cross-section ( $\sigma$ ) of the coupled plasmon mode ( $l_1$ ) becomes stronger for  $d < 5 \text{ nm}$  indicating that the strong electrostatic coupling

between the nanoparticle and  $Q$  increases up to values of  $\sim 30$ . This is also because the  $\Im m(\epsilon)$  of Au is at a minimum in the window of 600-800nm. In fact, in this spectral range both Au and Ag have relatively weak intraband and interband losses. Typically  $Q \sim 15$ -30 for an Au nanodimer at the  $l_1$  cavity resonance at  $d < 5$  nm.

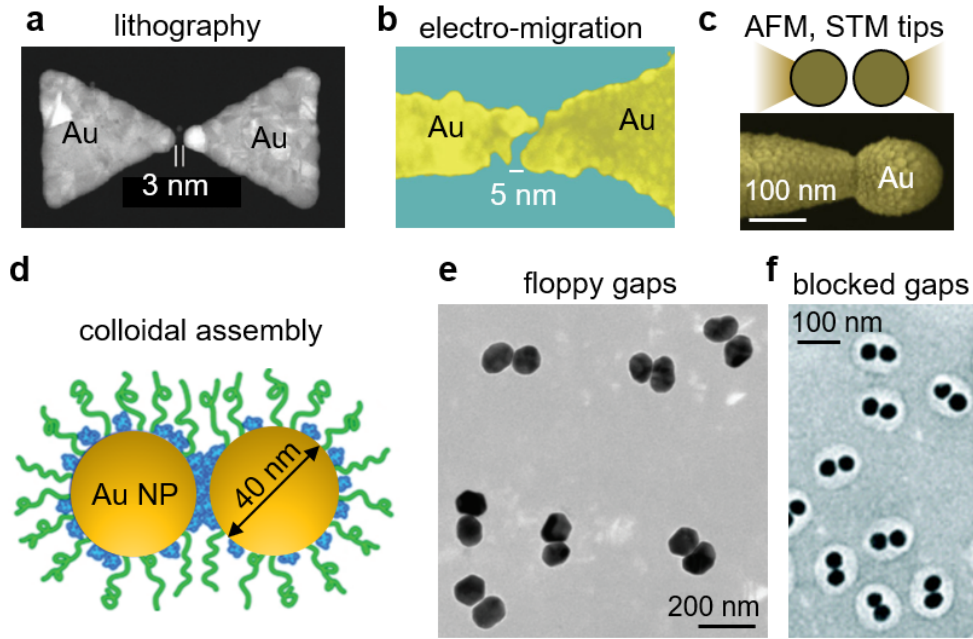


Figure 2.6: **Plasmonic nanogaps.** (a) Scanning transmission electron microscope (TEM) images of a plasmonic bow-tie antenna fabricated using e-beam lithography. Reproduced from [35]. (b) Scanning electron microscope (SEM) image of a nano-gap formed from electron migration. Reproduced from [36]. (c) SEM image of atomic force microscope tips coated with plasmonic nanoparticles. Reproduced from [37]. (d) Colloidal assembly of nano-dimer gaps with poly(ethylene glycol) (PEG) and poly(methyl methacrylate) (PMMA) and (e) SEM images of dimers obtained. Reproduced from [38]. (f) TEM image of nanodimers purified using differential centrifugation after encapsulating with polystyrene-block-poly(acrylic acid). Reproduced from [39].

## 2.5.2 Mode volume

In simple terms, the mode volume ( $V_m$ ) of a cavity is the volume in which the optical energy density is confined. The energy density of the system is given by [40],

$$W(r, \omega) = \frac{1}{2} \left( \frac{\partial[\omega \epsilon(r, \omega)]}{\partial \omega} \epsilon_0 |E(r, \omega)|^2 + \mu_0 |H(r, \omega)|^2 \right) \quad (2.11)$$

where  $\varepsilon(r, \omega)$  is the permittivity at a position  $r$ . To correctly account for the negative permittivity and dispersive character of plasmonic metals, one needs to use the term  $\frac{\partial[\omega \varepsilon(r, \omega)]}{\partial \omega}$  for the electric energy density inside the metal [34, 41–44].  $V_m$  is obtained by integrating the energy density over the volume of the nanoplasmonic structure, and normalizing it to the maximum value of  $W(r)$  at each  $\omega$  as,

$$V_m(\omega) = \frac{\int W(r, \omega) d^3r}{\max[W(r, \omega)]} \quad (2.12)$$

It is important to note that  $W(r, \omega)$  is complex inside the metal, due to their complex  $\varepsilon$ , hence  $V_m(\omega)$  is complex. Here,  $\Re(V_m)$  and  $\Re(W)$  are associated with the energy density in the system, and  $\Im(V_m)$  and  $\Im(W_m)$  with the energy dissipation in the metal. So,  $\Im(V_m)$  is commonly neglected and the equation reduces to the general definition of  $V_m$  as,

$$V_m(\omega) = \frac{\int \varepsilon(r) [E(r)]^2 d^3r}{\max[\varepsilon(r) [E(r)]^2]} \quad (2.13)$$

Note that this is exactly applicable only for lossless dielectric cavities.

To obtain an accurate value for  $\int W(r, \omega) d^3r$ , the electric and magnetic fields should be calculated in a 3D volume followed by integration. Accurately calculating these values using FDTD requires high mesh density for metallic nanostructures, especially when the gaps are  $<2$  nm. The mesh accuracy of the simulations defines the resolution of the confined fields in the gap, and therefore dramatically affects the value of  $V_m(\omega)$ . For gaps<sup>1</sup> of 1 nm, calculations were converged at a 0.3 nm meshing for nanoparticle dimers of size  $2R=40$  nm. The effective mode volume is minimum at  $\lambda_c=655$  nm giving rise to  $V_m=35.7 \pm 5$  nm<sup>3</sup>.

## 2.6 Fabricating nanocavities

Reliable fabrication of nanogaps with such high degrees of repeatability is a severe practical issue. To this end, various techniques have been developed based on both bottom-up

---

<sup>1</sup>Mode volume calculations are done in collaboration with Angela Demetriadou, Imperial College London, London, UK

synthesis and top-down fabrication. Top-down techniques including (Fig. 2.6), (i) high resolution electron beam lithography [35], (ii) computer programmed electro-migration process [36] and (iii) electrochemical deposition/etching on AFM tips [37] are all used to make gaps  $<5$  nm. However, these methods are not reliable for large scale fabrication (making  $>1000$  gaps with well controlled geometry at nanoscale). More importantly, defects and grain boundaries are hard to control in top-down processes.

On the other hand, bottom-up process such as colloidal synthesis produce fairly uniform ( $\pm 10\%$ ) nanostructures in large quantities (litre scale). However, methods to produce nanogaps are still limited to binding nanostructures with organic linkers such as dithiol, block co-polymers [39] and DNA linkers [45], which generally results in a low yield ( $<30\%$ ) and 'floppy' gaps. There are also separation techniques developed to increase the yield of nano-gap dimers including gel-electrophoresis and differential centrifugation [39], in which the formed structures are generally 'shell-isolated' with polymers for stabilization in high ionic concentration.

To overcome these challenges, I use a system termed the nanoparticle-on-mirror geometry (NPoM), the optical properties of which are similar to plasmonic nano-dimers. The fabrication of this geometry is much simpler than the fabrication techniques required to create other nanogap geometries.

## 2.7 Nanoparticle-on-mirror constructs

An equivalent system to the nanoparticle dimer is a nanoparticle placed over a metal surface with a small dielectric gap (Fig. 2.7). Analogous to the coupling in a nanoparticle dimer, charge oscillations in the nanoparticle are coupled with image charges in the film in NPoM, resulting in an effective dimer system.

The simple dipole coupling analogy does not provide the complete picture of mode coupling in the NPoM geometry (mode coupling is discussed in the following chapters). The fundamental mode  $l_1$  has similar charge distribution to a plasmonic dimer. Electromagnetic properties of this system were studied back in the 1980s by Aravind and Metlu, who predicted strong optical field enhancements and confinement in the gap [46, 47]. Nevertheless, studies on the complete picture of mode hybridization [48, 49] and practical limits on the enhancements [50] in the gap only emerged recently.

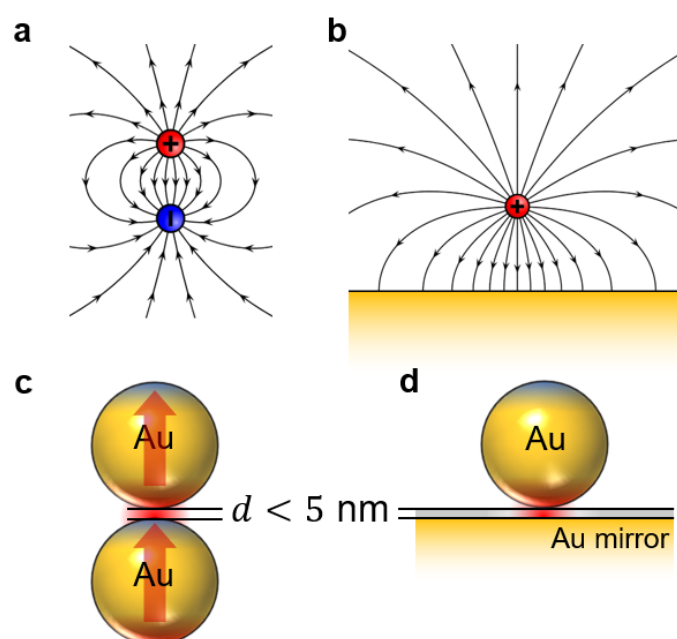


Figure 2.7: **Nanoparticle-on-mirror cavity.** (a) Fringing fields between the two opposite charges equivalent to (b) a charge placed over a polarizable surface. (c) Dipole-dipole coupling between the nanoparticle with gaps  $< 5$  nm equivalent to (d) a nanoparticle placed on a metallic substrate with an equivalent dielectric gap.

The optical excitation of the NPoM cavity is complex compared to the nano-dimer system. In this work, the NPoM is excited with plane waves at a high angle (Fig. 2.8a). When the electric field is polarized perpendicular to the metal film, the coupled mode ( $l_1$ ) is excited with strong low energy resonances (Fig.2.8b), controlled by the nanoparticle size ( $2R$ ), gap distance ( $d$ ) and refractive index of the gap ( $n$ ).

### 2.7.1 Sensing molecules in the gap

In my experiments, molecules are typically self-assembled on the metal surface before the deposition of nanoparticles. This results in molecules being located in the field volume of the  $l_1$  mode. As the fields are strongly confined in the gap, small changes in molecular properties will be reflected in the modulation of the coupled mode. For example, if a  $2R=80$  nm particle with a gap size of 4 nm is considered, a change in the refractive index in the gap from 1 to 2 shifts the coupled mode from 600 nm to 710 nm and increases its intensity (Fig. 2.8c).



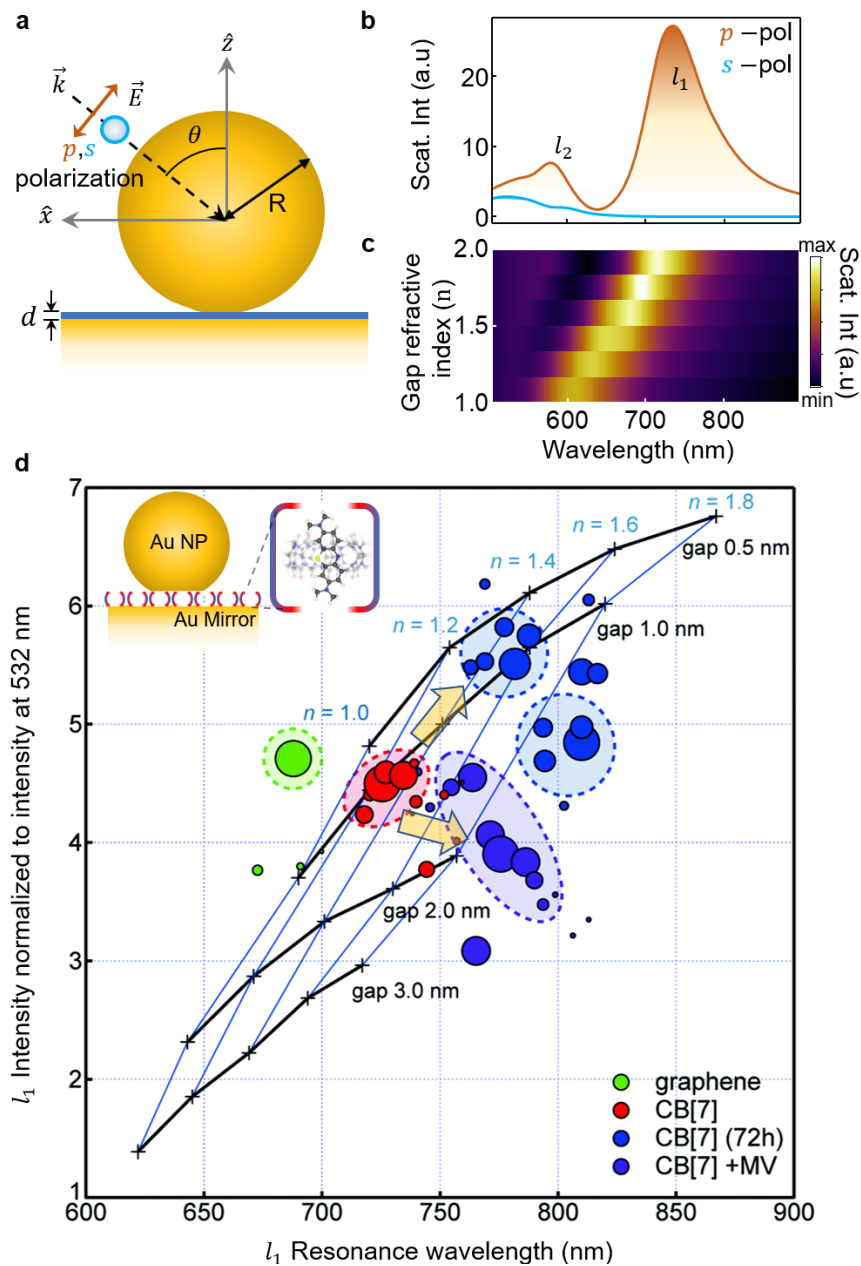


Figure 2.8: **Molecular sensing.** (a) Schematic of a NPoM system, representing the polarization directions of incident light used for FDTD simulation. The light illuminates at angle with 55 degrees to the normal perpendicular to the metal film. (b) Obtained scattering spectrum for two orthogonal polarizations (s- and p- as shown in (a)) for 80 nm particle with 1 nm gap and  $n=1.4$  refractive index. (c) Wavelength dependent scattering intensity (indicated by colour scale) obtained for various refractive indices at 4 nm gap. (d) Mapping the resonance position and intensity of  $l_1$  mode for various gap sizes and refractive indices. The experimentally obtained points are different spacer molecules Reproduced from [51].

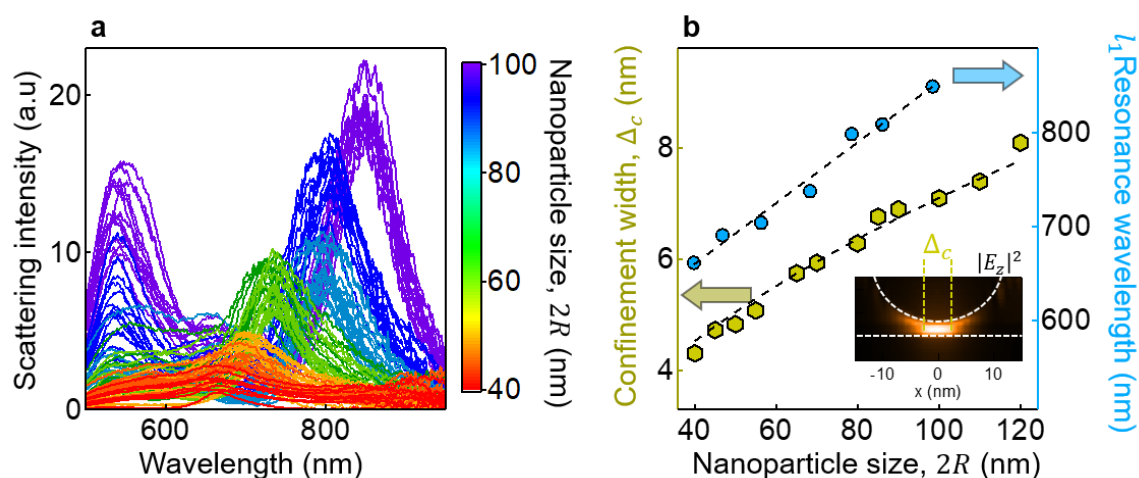


Figure 2.9: **Nanoparticle size.** (a) Scattering spectrum from  $>1000$  NPoM for various batches of different nanoparticles with sizes varying from 40–100nm (Reproduced from [54]). (b) FDTD results calculating the resonance wavelength and field confinement width ( $\Delta_c$ ) of the coupled mode for different nanoparticle sizes in NPoM geometry (the inset above shows the simulated near-field). The  $\Delta_c$  is fitted with  $\sqrt{R}$  (dashed black line).

The  $l_1$  resonance wavelength and its intensity become very sensitive to the kind of molecules assembled in the gap, especially at  $d < 3$  nm. The simulations and experimental results of graphene (gap of 0.4 nm) and self-assembled molecules of cucurbit-7-uril (CB[7]) (gap of 0.9 nm) are in good agreement [51]. Furthermore, loading CB[7] with guest molecules such as methyl-viologen (MV) shows clear shifts in the map, proving it is possible to monitor atomic scale changes [50–53].

## 2.7.2 Effect of nanoparticle size and shape

The size of a nanoparticle can be used to tune the resonance of  $l_1$  to a wavelength of interest (Fig. 2.9). Benzene di-thiol (BPT) is one molecule that self-assembles on Au surfaces with a high degree of uniform packing density and orientation, resulting in gap sizes of 1.1 nm in the NPoM geometry. By systematically increasing the nanoparticle size from 40 nm to 100 nm the resonance  $l_1$  mode can be linearly tuned from 650 nm to 850 nm. This can be seen experimentally and corroborated with theory. The intensity scaling of the  $l_1$  mode is found to be  $\propto R^6$  via dark-field measurements (Fig. 2.9a), which is in good agreement with theoretical predictions.

Optical fields are tightly confined in the gap similar way to the nanoparticle dimer systems [37], the width of this confinement is  $\Delta_c \sim \sqrt{R}$  (Fig.2.9b). In practice,

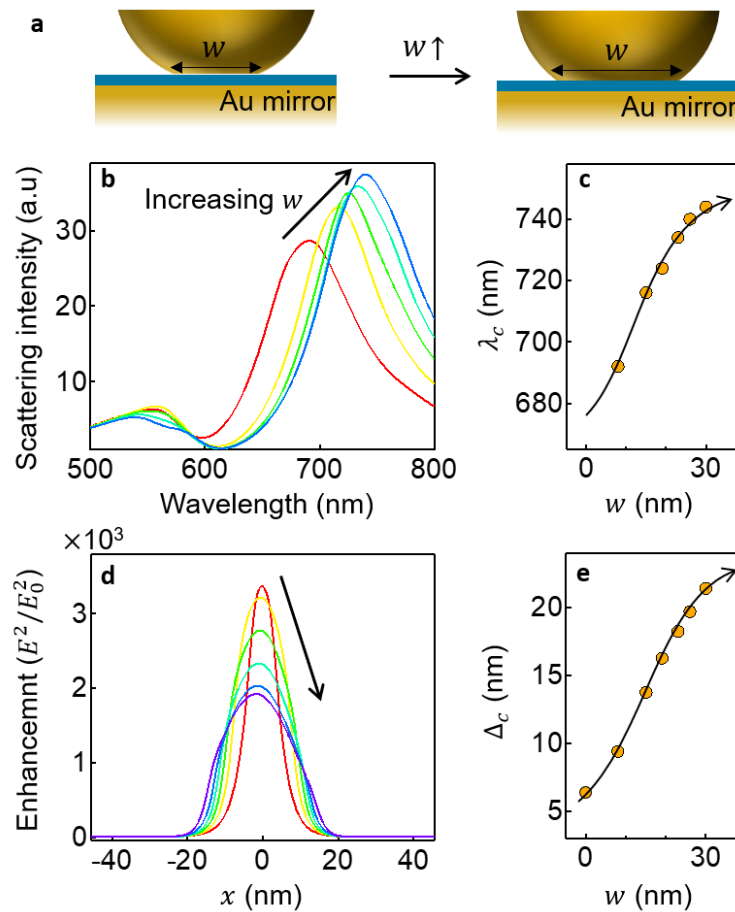


Figure 2.10: **Nanoparticle facets.** (a) Schematic showing increasing nanoparticle facet widths ( $w$ ). (b) Simulated scattering spectra for NPoM with different facet widths  $w=8$ -30nm ( $2R=80$  nm,  $n=2.1$  and  $d=4.5$  nm). (c) Variation in the resonance wavelength, (d) line profiles for electric-field enhancement along the gap, and (e) FWHM confinement widths for increasing facet width.

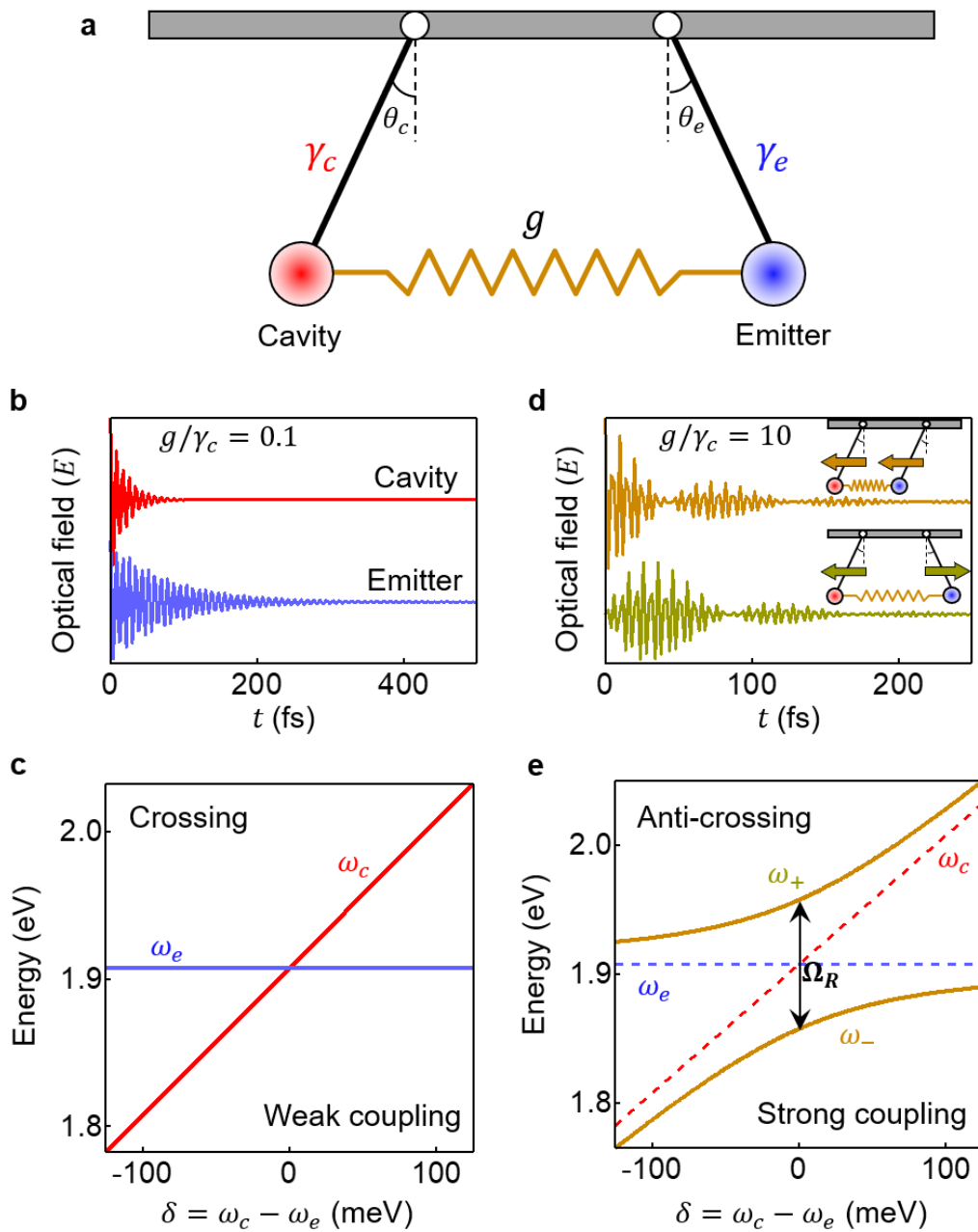


Figure 2.11: **Damped coupled harmonic oscillator model for light-matter coupling.** (a) Schematic of the cavity and the emitter as two damped oscillators connected by a spring. (b) Oscillations of the emitter and cavity in weak coupling regime. (c) Tuning the resonance of the cavity across the emitter resonance at  $g/\gamma_c = 0.1$ . (d) Oscillations of new coupled modes ( $\omega_+$ ,  $\omega_-$ ) in strong coupling regime ( $g/\gamma_c = 10$ ) and the phase of pendulum oscillations are shown in inset. (e) Anti-crossing of new polariton modes ( $\omega_+$ ,  $\omega_-$ ) on tuning the cavity resonance across the exciton energy.

nanoparticles are not spherical and colloiddally synthesized nanoparticles have a certain degree of crystalline facets. These faceted nanoparticles modify the optical resonance and confinement. To account for these facets, the nanoparticle is simulated as a cropped sphere at the base contact with various circular facet sizes,  $w$  (Fig. 2.10a). As the facet size increases (Fig. 2.10b,c) the degree of optical field screening within the cavity increases [49, 55], thus causing the coupled mode ( $l_1$ ) to decrease in energy. A secondary, potentially unwanted, effect of this is a decrease in the field enhancement (Fig. 2.10d,e). Once the facets are large enough they begin to support a new sets of plasmonic modes which intermix with  $l_1$  modes, this is extensively discussed in Chapter 3.

Having introduced plasmonic cavities, let us return to the discussion of coupling of molecules to confined optical modes and how optical properties are modified due to this coupling.

## 2.8 Light-matter coupling

A model system to visualize the dynamics of light-matter interactions is the damped coupled harmonic oscillator (here a coupled pendulum) where light (plasmons) and matter (molecule-resonance) are considered as classical oscillators with resonance frequencies of  $\omega_c$  and  $\omega_e$ , where  $c$  and  $e$  corresponds to cavity and emitter, respectively (Fig. 2.10a). Treating the cavity and emitter as classical harmonic oscillators (Sections 2.1 and 2.3) is a good approximation in weak excitation limits. The damping associated with the plasmon and the emitter are incorporated into the friction of each pendulum represented by  $\gamma_{c,e}$ . The coupling strength  $g$  between the plasmon and the emitter is modelled by a spring connecting the two pendulums [56].

This coupled system evolves according to a set of coupled differential equations characterized by the time varying angles  $\theta_c(t)$  and  $\theta_e(t)$ .

$$\frac{d^2\theta_e}{dt^2} + 2\gamma_e \frac{d\theta_e}{dt} + \omega_e^2\theta_e + g^2(\theta_e - \theta_c) = 0 \quad (2.14)$$

$$\frac{d^2\theta_c}{dt^2} + 2\gamma_c \frac{d\theta_c}{dt} + \omega_c^2\theta_c + g^2(\theta_c - \theta_e) = 0 \quad (2.15)$$

The energy transfer between these two oscillators is determined by the coupling constant  $g$ . The resulting non-trivial solution to the above coupled equation is,

$$\Omega_{\pm} = \frac{1}{2}(\Omega_c + \Omega_e) \pm \frac{1}{2}\sqrt{(\Omega_e - \Omega_c)^2 + 4g^2} \quad (2.16)$$

where  $\Omega_i = \omega_i - i\Gamma_i/2$  denotes the complex frequency of a resonance with frequency  $\omega_i$  and linewidth  $\Gamma_i$ . This can be simplified to find the frequency of the two hybrid states  $\omega_{\pm}$  as,

$$\omega_{\pm} = \frac{1}{2}(\omega_e + \omega_c) \pm \frac{1}{2}Re \left\{ \sqrt{4g^2 + \delta^2 - (\gamma_e - \gamma_c)^2/4 - 2i\delta(\gamma_e - \gamma_c)/2} \right\} \quad (2.17)$$

where  $\delta = (\omega_c - \omega_e)$  with  $\omega_{\pm}$  being the energies of the new hybrid modes determined by the coupling strength  $g$ . This purely classical picture covers the complete dynamics of light-matter coupling in linear-weak excitation limits, where a harmonic ladder of energies can be approximated to a two-level system. In fact, a full quantum mechanical solution obtained using the Jaynes-Cummings (JC) Hamiltonian provides eigenenergies similar to the classical solution [57, 58].

The value of  $g$  is determined by the parametric strength of exciton dipole ( $\mu$ ) and the cavity mode volume ( $V_m$ ) [12].

$$g \propto \mu\sqrt{V_m} \quad (2.18)$$

Depending on the coupling strength and damping associated with the system, two different regimes of light-matter interactions can be defined. (i) Weak coupling: In this limit  $\frac{g}{\gamma_{c,e}} \ll 1$ ; the two oscillators behave independently and  $\theta_{c,e}(t)$  converges to zero exponentially (Fig. 2.11b). Here the eigenfrequencies of the system are not inherently modified. Therefore, tuning the oscillation frequency of cavity ( $\omega_c$ ) over the exciton frequency ( $\omega_e$ ) causes an energy cross-over since the oscillators cannot efficiently exchange energy (Fig. 2.11c). (ii) Strong coupling: Here  $\frac{g}{\gamma_{c,e}} \gg 1$ ; the cavity and emitter are able to exchange energy over several oscillation periods, therefore resulting in the formation of new eigenmodes ( $\omega_{\pm}$ ) (Fig. 2.11d).  $\omega_{\pm}$  correspond to oscillations of the cavity and emitter in-phase ( $\omega_-$ ) and anti-phase ( $\omega_+$ ). These new eigenmodes depend

entirely on the characteristic coupling constants of the system as their energies are given by  $\omega_{\pm} = 1/2(\omega_c + \omega_e) \pm 1/2\sqrt{g^2 + \delta^2}$ . Therefore, anti-crossing behaviour is observed when the cavity resonance is tuned over the exciton resonance ( $\delta = \omega_c - \omega_e$ ) (Fig. 2.11e).

The dispersion of  $\omega_{\pm}$  tends to the uncoupled cavity and exciton energies at large detuning. For the scenario where  $\delta = 0$ , the energy splitting between  $\omega_{\pm}$  is referred to as the vacuum Rabi splitting ( $\Omega_R$ ). The observation of  $\Omega_R \neq 0$  is a direct evidence that the system is operating in the strong coupling regime and measuring  $\Omega_R$  allows us to quantify the interaction strength. However, measurement of  $\Omega_R$  is complicated and experiments such as reflection, transmission and absorption spectra of the coupled system might give slightly different values ( $\Omega_R^r$ ,  $\Omega_R^t$  and  $\Omega_R^a$  respectively). In particular, earlier works on dielectric microcavities by Savona and co-authors demonstrated that  $\Omega_R^a \leq \Omega_R^t \leq \Omega_R^r$ . This anomalous situation is referred to as the intermediate coupling regime which occurs for low quality factor cavity  $Q < 100$  [56]. Similar observations are also reported in the coupling of molecular aggregates on plasmonic films. These effects are directly linked to the finite damping of the system which is dominated by absorption of excitons or SPPs. However, for localized plasmon systems where coupling is generally probed via scattering measurements, achieving  $g \gg \gamma_c + \gamma_e$  would represent the strong-coupling regime. The implications of weak and strong coupling are discussed in the following sections.

### 2.8.1 Weak coupling regime and Purcell effect

In the weak coupling regime ( $g \ll \gamma_c, \gamma_e$ ) the resonant energies are not directly effected by the coupling in the system, however the presence of light-fields around the emitter profoundly affects the spontaneous decay rates. This effect was initially proposed for nuclear transitions in atoms by Purcell in 1946 and hence the ratio of modified ( $\Gamma_m$ ) and free-space ( $\Gamma_0$ ) decay rates is known as the Purcell factor [60].

$$F_P = \frac{\Gamma_m}{\Gamma_0} = \frac{3Q(\lambda/n)^3}{4\pi^2 V_m} \quad (2.19)$$

Here,  $\lambda/n$  is the wavelength associated with the transition frequency of an emitter in a medium of refractive index  $n$ . The cavity quality factor and mode volume are defined by  $Q$  and  $V_m$ . In our case the emission and cavity resonance frequencies are assumed to be perfectly matched. In plasmonic cavities, where the  $V_m$  is very small, this leads

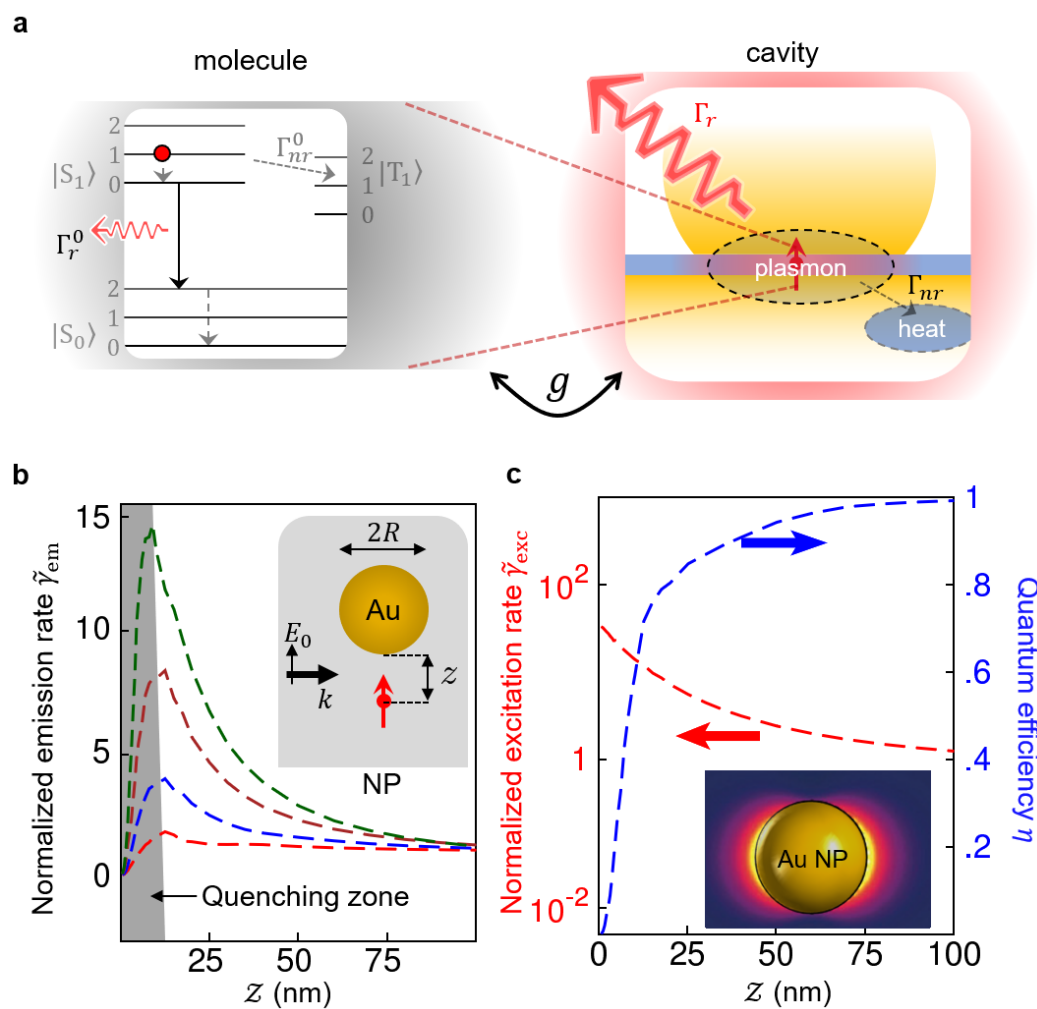


Figure 2.12: **Decay pathways.** (a) Sketching the different decay pathways of the excited molecule coupling to plasmonic cavity. (b) Calculated radiative emission of point dipole coupled to plasmonic nanosphere as a function of emitter-metal distance. (c) Calculated excitation rate and quantum efficiency of the emitter; near-field enhancement around nanoparticle shown in the inset. b and c are reproduced from [59]



to large spontaneous decay rates. However it is incorrect to assume that the enhanced decay always leads to an increase in emission in the far-field. This is especially true in an individual plasmonic nanocavity, such as a spherical Au NP, where the enhanced decay can be lost to absorption within the metal. This absorption is termed the non-radiative decay channel ( $\Gamma_{nr}$ ) [note that this is different from the non-radiative decay channels inside the molecule itself ( $\Gamma_{nr}^0$ )] (Fig. 2.12a) [21, 61]. Therefore, the total radiative emission intensity extracted from a molecule near the metal (fluorescence enhancement) is determined by the competition between radiative ( $\Gamma_r$ ) and non-radiative coupling rates ( $\Gamma_{nr}$ ).

The radiative quantum efficiency of the system is defined as,

$$\eta = \frac{\Gamma_r + \Gamma_r^0}{\Gamma_r^0 + \Gamma_r + \Gamma_{nr}^0 + \Gamma_{nr}} \quad (2.20)$$

It is important to note that the coupling of molecules to these different channels depends on the distance between the molecule and the nanoparticle. For an isolated NP cavity, molecules closer to the NP experience the maximum excitation rate ( $\gamma_{exc} \propto E^2$ ) but suffer from lower quantum yield. An optimal distance between the Au NP and molecule at which the emission intensity is maximised ( $\sim 10$  nm) (Fig. 2.12b). At shorter distances, the emission is strongly suppressed by the coupling with higher order, mostly non-radiative modes of the cavity ( $l_{2,3,\dots}$ ). This regime in which the emission is suppressed is generally termed the 'quenching' zone. Another non-radiative pathway which is not represented here (Fig. 2.12a) is a charge transfer process between the molecule and plasmon. The molecule in an excited state can undergo redox chemistry by transferring an electron to the metal (resonant electron transfer). The reverse process is also possible, in which excited plasmons relax by emission of high-energy electrons (hot-e) which are captured by molecules absorbed on the surface [65]. However, the energy dynamics of these processes is still a matter of debate.

The quenching zone is suppressed to near zero values for those plasmonic cavities in which excitation rates dominate the quenching rates [66, 67]. As discussed previously, plasmonic nanodimers and NPoM cavities supporting high field enhancement ( $E/E_0 > 100$ ) in nanogaps are ideal for obtaining large light emission from molecules. In a NPoM cavity, the emission from the molecule in the gap is strongly enhanced even when the distance between the metal and the molecule is  $< 1$  nm (Fig. 2.14a). At larger distance the coupling between the NP and the film is weak, therefore larger NP are required for any effects to be observed. However, at small gaps ( $d < 5$  nm) smaller nanoparticles ( $2R = 40$  nm) give

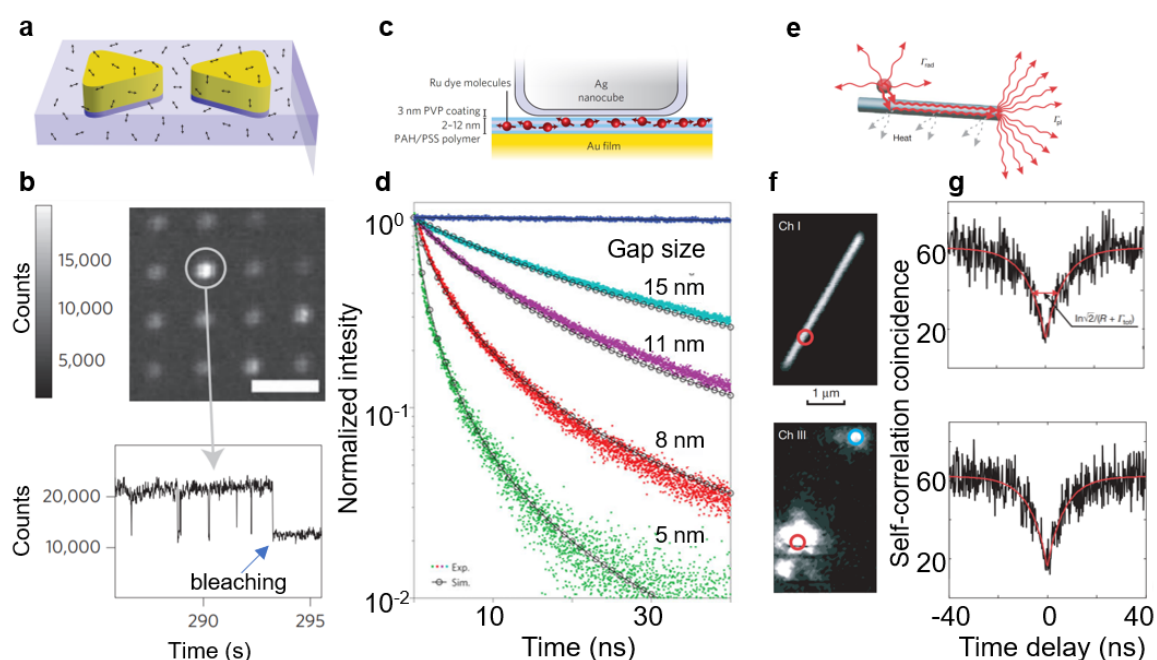


Figure 2.13: **Enhanced light emission from plasmonic cavities.** (a) Schematic of a bowtie gold nanoantenna coated with fluorescent molecules (black arrows). (b) Confocal scan of 16 bowties coated with fluorescent molecules on an average of 3 molecules per gap. The fluorescence time trace of one such gaps shown below represents blinking dynamics and eventual photobleaching of one molecule that has been enhanced by a factor of 1,340.(a-b) Reproduced from [62]. (c) Cross-section of the experimental structure consisting of Ru dye intercalated into a polymer film and situated between a gold film and a silver nanocube. Arrows indicate typical directions of the transition dipole moments.(d) Measured and simulated time-resolved ruthenium metal complex dye (Ru dye) emission for four gap thicknesses with normalized intensities.(c-d) Reproduced from [63]. (e) Radiative coupling of quantum dots (QD) to silver nanowires. A coupled QD can emit photon into the guided surface plasmon modes of the nanowire. (f) (top) Optical image of a plasmonic nanowire and position of QD is encircled in red. (below) Fluorescence image of (f) with excitation laser focused on the quantum dot. The blue circle indicates the light emission from the farthest end of the nanowire, used for photon cross-correlation measurements. (g) Second-order correlation function  $g^{(2)}(\tau)$  of single quantum dot fluorescence (top) without and (bottom) with coupled to nanowire. (e-g) Reproduced from [64].

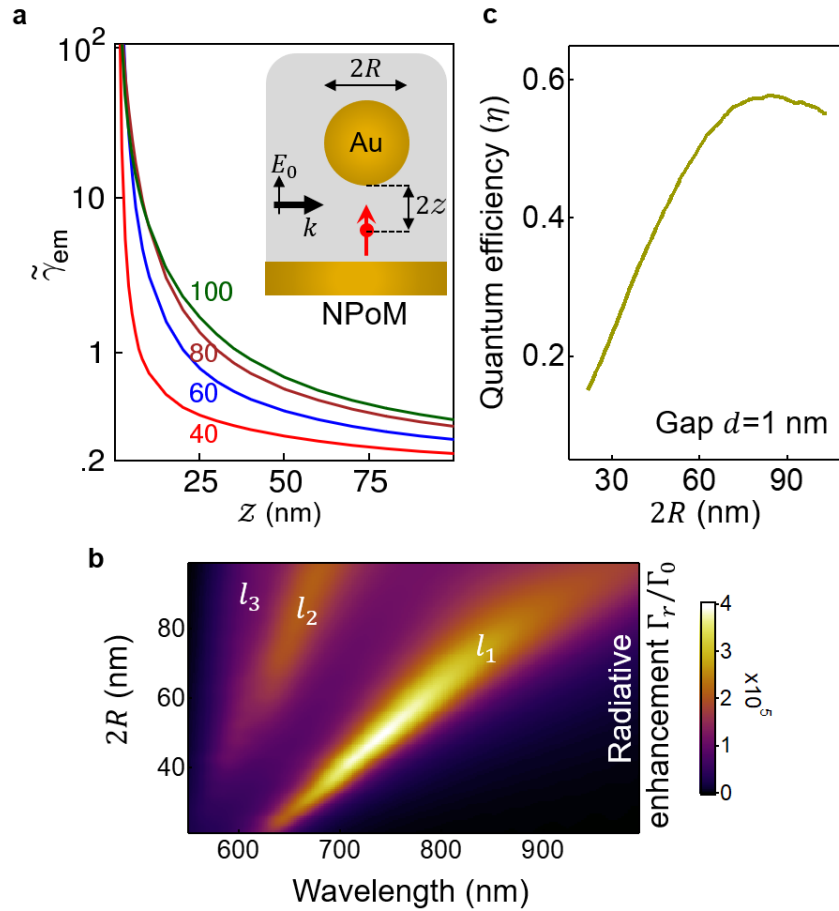


Figure 2.14: **Emission from NPoM cavity.** (a) Calculated emission from the system for various gap sizes and positions of the point emitter at the centre of the cavity. (b) Radiative enhancement of an emitter placed in 1 nm gap NPoM cavity for various nanoparticle sizes, and (c) the quantum efficiency extracted from  $l_1$  mode. Fig. a, b are reproduced from [59].

equal enhancement. The competition between the radiative and non-radiative rates is crucial for our NPoM systems with 1 nm gaps, as  $\Gamma_r$  is larger than  $\Gamma_{nr}$ . The quantum efficiencies  $\eta > 0.5$  can be reached in this geometry when the size of the nanoparticle is between 60-80 nm (Fig. 2.14b). Comparatively in single NP cavities emission is strongly quenched. Furthermore, when an emitter in the NPoM couples to the  $l_1$  mode, radiative enhancements  $> 10^5$  can be achieved (Fig. 2.14c). Higher order modes  $l_2$  and  $l_3$  acquire a strong radiative component at small gaps due through their hybridization with dipolar modes, hence suppressing the quenching zone.

From the enhancement rates it is possible to extract the mode volume of the system, since the Purcell factor is a measure of the total decay rate, where  $\Gamma_m = (\Gamma_r + \Gamma_{nr})$ . In NPoM systems,  $\Gamma_m/\Gamma_0 > 10^6$  at 650 nm, resulting in effective mode volumes  $< 100 \text{ nm}^3$ .

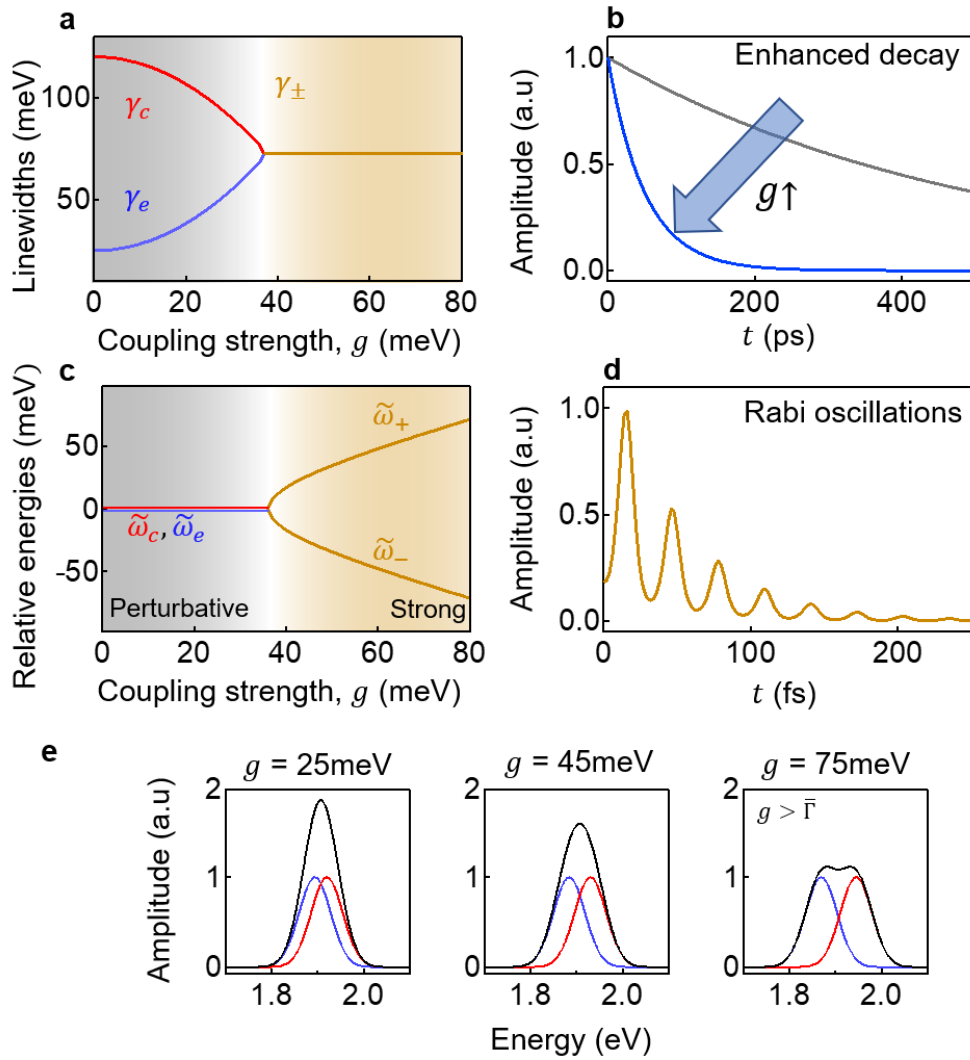


Figure 2.15: **Purcell enhancement and Rabi oscillations.** (a) Variation of linewidths and (c) relative energies of cavity, exciton and polariton energies with change in coupling strength. Time dynamics of an emitter coupled to cavity in (b) the weak and (d) strong coupling regime. In weak coupling, decay rate is enhanced, whereas in strong coupling Rabi oscillations are observed. (e) Calculated polariton modes and the total summed response as a function of coupling strength, between the limits of Eqs. 2.21 and 2.22.

It is important to note that emission enhancement measured in experiments [68–71] (ratio of intensities with and without a cavity) is not equal to the Purcell factor in plasmonic cavities, because the intensity of ingoing light is concentrated at the location of the emitters, increasing the amount of light they absorb. Therefore the increased emission is only from this absorption enhancement. To circumvent this issue, the enhancement in fluorescence intensity needs to be measured at high laser intensities at which the absorption saturates and the emission intensity is dominated only by the radiative decay rates [72]. However many molecules will undergo rapid photobleaching before saturation. On the other hand, the total number of photons emitted by the molecule before it bleaches is independent of the rate at which the molecule is excited, so the enhancement in total photons emitted is proportional to the radiative enhancement factor [73].

Early experiments by Kinkhabwala *et al.* [62] measured the enhancements upto 1300 in the brightness of a single molecule's fluorescence for gold bowtie nanoantennas with gaps  $< 20$  nm (Fig. 2.13a,b). Electromagnetic simulations from the same study revealed that the increase in brightness was due mainly to an enhanced absorption. However in recent studies Akselrod *et al.* [63] demonstrated enhancement in radiative decay rates by factor 1000 in the narrow gaps (5 nm) formed between silver nanocubes and gold film (Fig. 2.13c,d). These measurements involved ensembles of emitters with unoptimized orientation of dipoles. Later experiments [74, 75] by the same group showed similar enhancements when coupling to a single quantum dot in the same geometry, resulting in an ultrafast single-photon source at room temperature. For quantum technologies it is important to have nanoscale antennas that can efficiently absorb light from single-emitters and subsequently emit the photons in a well-controlled manner. To this end Akimov *et al.* [64] demonstrated the coupling of single-photon emission from a quantum dot to a SPP mode of silver nanowire (Fig. 2.13e-g). They also observed that the light emission from the other end of the nanowire was antibunched, confirming the quantized nature of SPPs.

Before discussing the strong coupling regime, in which the energies of plasmon and molecule are intermixed to form new resonances of the system, it is important to consider that the spectral linewidths of the molecules and cavity are perturbed in the weak coupling regime, as the emission by the molecule is not uniformly enhanced/suppressed. The linewidths of the emitter increase with increasing coupling strength ( $g$ ) (Fig. 2.15a), as the emission is faster in both radiative and non-radiative channels [12, 76]. This increase in linewidth,  $\gamma_e = \gamma_0 + \gamma_m$  is proportional to the Purcell enhanced rate.  $\gamma_m$  continues to increase proportional to  $g^2$  until the system reaches the strong coupling regime, where new

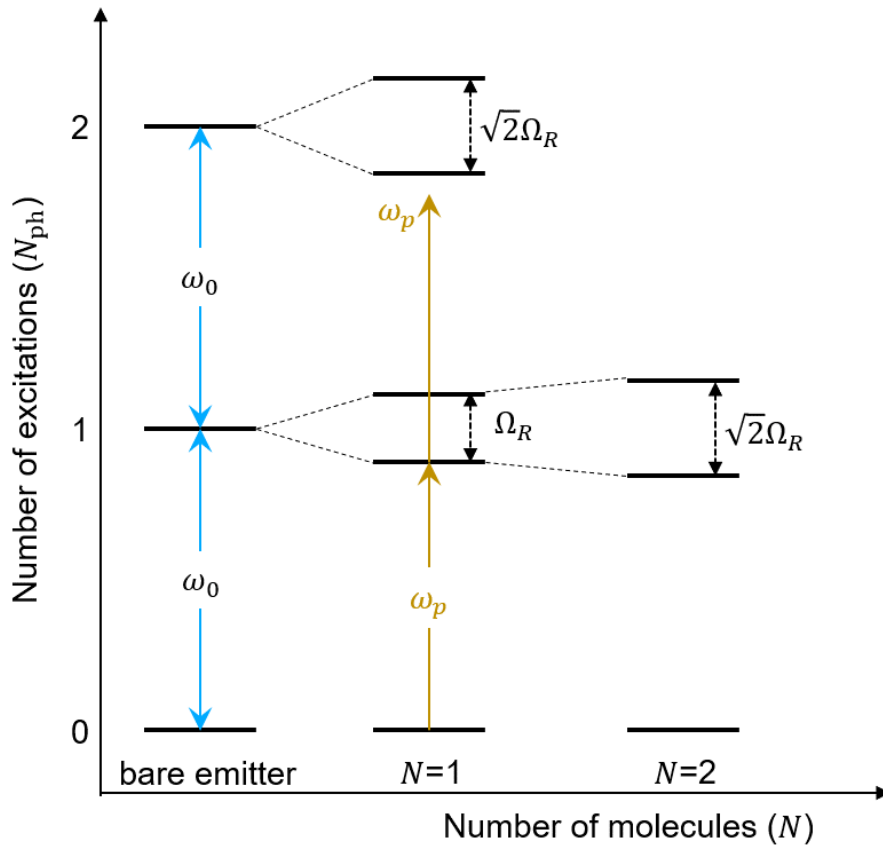


Figure 2.16: **Nonlinearity of polariton states.** Schematic of the hybridized energy levels: each excitation ( $N_{\text{ph}}$ ) in the harmonic ladder has two states associated with it. The energy splitting of each state is given by  $\Omega_R \sqrt{N_{\text{ph}}}$ . This anharmonic splitting is shown in the diagram and explains how  $\omega_p$  will only excite the first manifold and nothing greater, creating a photon blockade. The splitting energy scales  $\sqrt{N}$  with  $N$  being number of emitters coupled in the system.

hybrid eigen states emerge ( $\omega_{\pm}$ ). This is a phase transition with the system switching at critical emitter damping, from perturbative regime to strong coupling regime.

## 2.8.2 Strong coupling

Strong coupling occurs in a system when  $\omega_{\pm}$  results in real values at zero detuning with,

$$g^2 > (\gamma_c - \gamma_e)^2 / 16 \quad (2.21)$$

The time dynamics shows periodic oscillations (Rabi oscillations) which are masked with

finite damping of the system  $(\gamma_e + \gamma_c)/2$  (Fig. 2.15d). However, this clearly fails when  $\gamma_c = \gamma_e$  since in this case the equation 2.16 always gives real solutions even though the linewidths may be larger than the splitting [56]. To observe the split, the modes clearly require at least,

$$\Omega_R > \bar{\Gamma} = (\gamma_c + \gamma_e)/2 \quad (2.22)$$

giving the condition  $2g > \bar{\Gamma}$ . These different scenarios are mapped in Fig. 2.15d. There are two types of damping processes that destroy the coherence of the Rabi oscillations. (i) Spontaneous decay to lower electronic states: this process occurs stochastically, breaking the coherence of the wave function. The rate of this damping process is set by the lifetime of the polariton states (both radiative and non-radiative part). (ii) Phonon decoherence: the dephasing is complicated to understand for molecular systems with strong vibrational states, further complicated by the interaction with the environment that perturbs the phase of the wavefunction and destroy the Rabi flipping dynamics.

The energy ladder obtained from the solution to JC Hamiltonian for strong-light matter coupling depicts the anharmonicity of the structure (Fig. 2.16). This is also known as a JC ladder, giving rise to an intriguing optical effect of a photon blockade [77–79]. Photon blockade arises when the first excitation blocks absorption of a second photon of the same energy, enabling nonlinear response with a single photon. However, the spectrum of the system changes when more than one emitter is involved in the interaction. A system of  $N$  emitters coupled to the same electromagnetic mode acts like a giant quantum oscillator with dipole strength  $\mu\sqrt{N}$ . Hence the strength of coupling correspondingly scales with the number of emitters, whereas the higher excitations are harmonic and do not induce the effect of photon blockade within the limits of  $N_{\text{ph}} \ll N$ .

Earlier works on strong coupling in plasmonic systems focused on the coupling of molecular aggregates with SPP modes on metal film [84–92]. In most experiments strong coupling was observed between a silver film and exciton modes of  $J$ -aggregates or aggregates of dye molecules. The strength of the coupling was revealed by measuring anticrossing in reflectivity measurements. Furthermore, the light emission from the coupled system traced the position of the lower polariton branch with no evidence of emission from the upper polariton branch. Few studies attributed this phenomenon to the presence of a large number of uncoupled excitons in the system, energy relaxation dynamics of different polariton states, presence of  $N-1$  dark states or even the wavelength of excitation. This

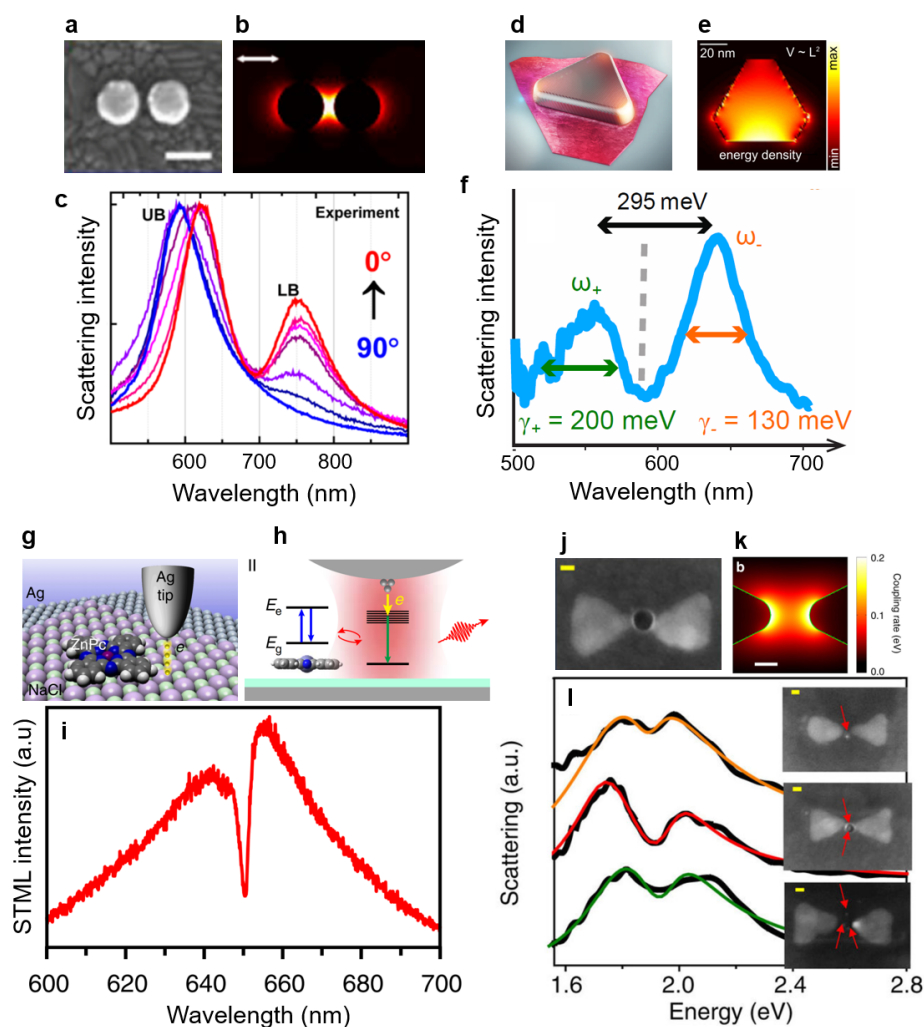


**Figure 2.17: Strong coupling in plasmonic cavities.** (a-c) Au plasmonic nanodisc dimer coupled with molecular  $J$ -aggregates. (a) SEM image of a plasmonic nanodisc dimer with a diameter of 85 nm and a gap of 15 nm. (b) Near-field enhancement map ( $E^2/E_0^2$ ) for (a), with maximum enhancement of 200 in the gap. (c) Polarization dependent scattering spectra obtained from the nanodisc dimer system on coupling with excitons transition wavelength of  $J$ -aggregates at 693 nm.  $0^\circ$  represents the detection polarization angle parallel to the dimer axis. (a-c) Reproduced from [80]. (d) Schematic view of  $J$ -aggregate sheet coupled with silver nanoprism. (e) Energy density  $\varepsilon|E|^2$  distribution around a silver nanoprism, showing that  $V_m$  is approximated by geometrical volume of the nanoprism. (f) Scattering spectrum of a single nanoprism strongly coupled to  $J$ -aggregates, resulting in a pronounced scattering dip. (d-f) Reproduced from [81]. (g) Schematic of experimental STM used to achieve single-molecule Fano resonance. (h) Ag tip in close proximity to the molecule and (i) corresponding STM luminescence spectra representing a typical Fano lineshape. (g-i) Reproduced from [82]. (j) SEM image of plasmonic bowties. (k) Scattering spectra of bowties with (from top to bottom) one, two and three QDs in the gap. All spectra show a transparency dip due to Rabi splitting. (l) Spatial distribution of the coupling strength in the gap between the bowties. (j-l) Reproduced from [83].



absence of upper polariton branch emission is still an unsolved issue and is a subject of ongoing debate. [93, 94].

Exciting features start to appear when the number of emitters is drastically decreased to the quantum limit of one emitter level. To progress in that direction, localized plasmonic modes are utilized. In recent experiments with plasmonic dimers, nanorods, cubes, core-shell nanoparticles, nanostars and nanoprisms the number of excitons is drastically reduced to  $<1000$  excitons [80, 95–99] (see Fig. 2.17a-f for experiments on nanodimers and nanoprisms). There was also significant evidence of uncoupled excitons in their data. This is expected because, although  $J$ -aggregated molecules are coated on nanostructures the optical fields are strongly confined in the gaps or on the surface, which is sometimes shielded by the oxide layers in silver substrates or else the excitons are not aligned well with the optical fields.

Achieving strong coupling at single emitter level requires meticulous alignment of the emitters in a highly confined plasmonic mode volume. A study published after the work presented in Chapter 7, utilized STM tips with sub-nanometre spatial control to couple confined plasmon modes near the tip with molecules deposited on the surface (Fig. 2.17g-i). When the tip is in close proximity they observed Fano lineshapes in tunneling electron-induced luminescence spectra [82]. However, the coupling strengths were still limited to values lower than the cavity damping rates due to the mismatch between the molecular dipole and cavity fields. In another work, Santhosh *et al.* [83] utilized capillary forces to assemble one to few quantum dots (QD) in the gaps of silver bowtie cavity (Fig. 2.17j-l). They observed a transparency dip in the scattering spectra, registering coupling strength of 120 meV, close to the strong coupling regime.

As have been discussed, the fabrication of nanocavities with small gaps  $d < 5$  nm is extremely demanding. Moreover, specifically positioning the molecule in this tiny gap is an extremely challenging task. In the next chapter I discuss experimental methods used to make NPoM cavities and to position molecular emitters into these tiny gaps with controlled orientation and position. I also discuss the optical techniques developed to probe these nanocavities.





### **3 Supramolecular Assembly and Nano-Optical Spectroscopy**

Constructing reliable plasmonic nanocavities with precise nanogaps and the molecule of interest positioned at the field-maxima at optimal orientations is crucial for optimized light-molecule coupling. Obtaining such nanocavities has always been hard due to the stochastic variation associated with nanoparticle size, shape, anisotropy of molecules and floppiness of weak van der Waals forces. Highly interdisciplinary tools are needed to build nanoscale plasmonic cavities and to probe them. In this chapter, I discuss the fabrication of plasmonic nanocavities with robust control over nanometre gaps and methods to position molecules into these gaps at precise location and orientation using supra-molecular self-assembly. Having achieved these nanocavities, I further introduce the nano-optical spectroscopy methods used to probe light-molecule coupling phenomena presented in this thesis.

## 3.1 Self-assembled monolayers on metallic surfaces

Certain organic molecules have the capability to spontaneously assemble on Au surfaces with order and high density. These assembled molecules are termed self-assembled monolayers (SAMs) [100]. The molecular structure of such molecules is generally classified into three different regions (Fig. 3.1a). (i) Functional groups bind to Au surfaces via covalent bonds or via strong van der Waals interactions [101, 102]. Typically, the bond strength of these affinities is larger than  $k_B T$  ( $k_B$  = Boltzmann constant). The chemistry of Au is unique in this aspect of binding molecules, as Au does not have any stable oxide states ( $Au_2O_3$  is the only metastable state) allowing surfaces accessible for binding other molecules. However, the extremely high electron affinity of Au (2.31 eV) allows molecules with soft electron donating groups to bind to the Au surface [103]. Thiols and carboxy- and  $\pi$ -electron clouds of phenyl groups have been highly studied and are used in this study (Fig. 3.1b). (ii) The head group of the SAM molecule is located at the opposite end of the molecule determining the chemical properties of the SAM surface. The head and functional groups are separated by (iii) the backbone which is composed of either or both aliphatic ( $-CH_2-$ ) or aromatic ( $-phenyl$ ) groups. The backbone determines both the electronic and heat transport properties as well as the mechanical properties of the SAM. To obtain a high degree of order, it is important that there is a certain interaction between the molecular backbones. In this work, different lengths of alkane and aromatic thiol molecules are self-assembled on flat Au surfaces (Fig. 3.1c).

The assembly of SAMs is governed by the co-operative interaction with the binding energy of the functional group with the Au substrate and the intermolecular interaction, for example,  $\pi - \pi$  stacking. The binding energy of a thiol group to Au is  $\sim 1.9$  eV [104], which is sufficiently large to compensate for the change in entropic energy. Assembly of SAMs on Au initiates from the rapid attachment of molecules to the Au surface followed by very slow ordering of molecules by maximizing the interaction between the backbone and the gold surface [105, 106]. For typical concentrations and solvents (1 mM in ethanol), this second step is completed within  $\sim 24$  h.

To summarize, SAMs have the following unique properties from the point of view of light-molecule coupling in plasmonic nanocavities: (i) Robust monolayers are formed with highly dense and defined orientation of molecules on plasmonic Au surfaces. (ii) Specifically for NPoM geometries, these SAMs act as insulating spacers when a nanoparticle is deposited on top. SAMs are typically 1-3nm elementary thin film materials and determine

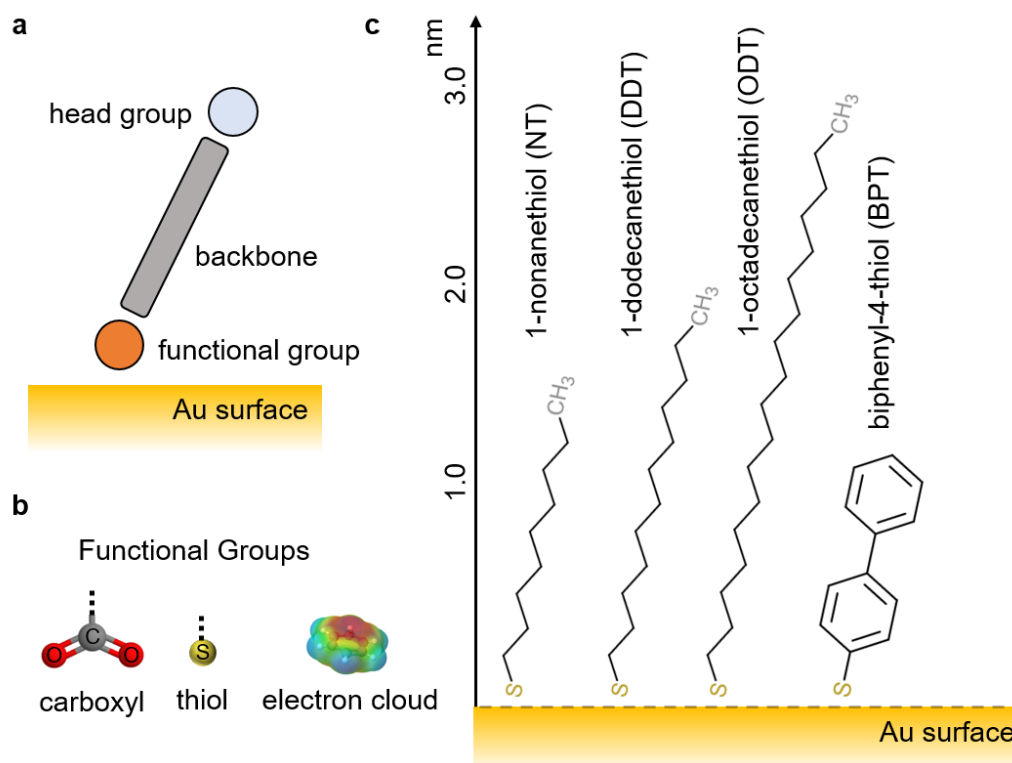


Figure 3.1: **Assembly of molecules on Au surface.** (a) Illustration of different regions of the molecule that spontaneously self-assembles on the Au surface. (b) Examples of functional groups that bind to the Au surface and support the assembly of molecules. (c) Different SAMs used to control the gap distance between the Au surface and the nanoparticle deposited on top.

the nm gap size between two plasmonic surfaces. (iii) Different functionalities of the end group can be explored for controlling the surface wettability and chemistry of plasmonic surfaces to absorb molecules that in general do not sit on Au surfaces. However, SAMs are limited to few sets of molecules with the right functionalities and geometry. Further, direct chemical bonding of molecules of interest with metal can result in undesirable modification of the chemical properties of the molecule. High packing density can be disadvantageous sometimes, due to the electronic coupling between the molecules modifying the resonances. To address these issues, I use guest-host complexes of cucurbit- $[n]$ -uril (CB $[n]$ ) molecules.

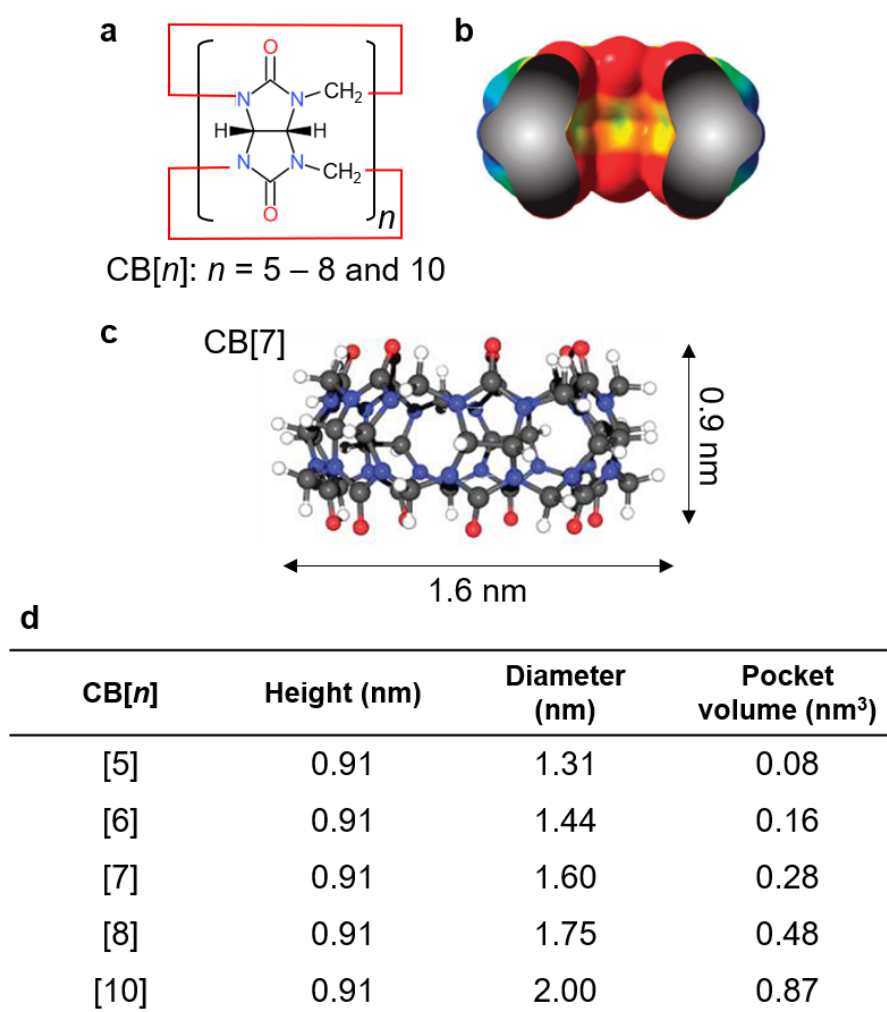


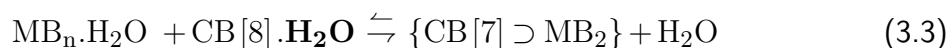
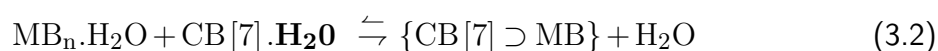
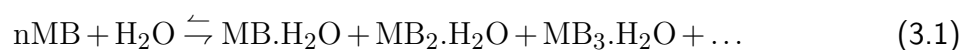
Figure 3.2: **Supramolecular host, Cucurbit-[-*n*]-uril.** (a) Chemical structure of the monomer unit of CB[*n*]. (b) Electrostatic potential of CB[7], reproduced from [107]. (c) Chemical structure and physical dimensions of CB[7]. (d) Physical dimensions of different CB[*n*].

## 3.2 Cucurbit- $[n]$ -uril: Supramolecular host

Cucurbit $[n]$ uril host molecules are pumpkin-shaped water soluble macrocyclic molecules composed of repeating units ( $[n]=5-8,10$ ) of methylated glycoluril arranged in a ring<sup>1</sup> (Fig. 3.2a). This barrel-shaped geometry inherently makes the CB $[n]$  extremely rigid under compression of the portal regions [108, 109]. The carbonyl rings at the portals of the CB $[n]$  have negative electrostatic potential (Fig. 3.2b) values  $>1.5$  eV. This allows CB $[n]$  to bind to various positively charged ions such as Fe<sup>2+</sup> and Na<sup>+</sup>. However, the inner pocket encompassed by the fused rings has no functional groups and no free electron pairs. Thus, the inner pocket of CB $[n]$  is somewhat hydrophobic and has preference towards the encapsulation of even slightly hydrophobic compounds. The inner pocket volume varies for different  $[n]$  values, allowing the capture of specific host molecules. The physical dimensions of different CB $[n]$  are noted in Fig. 3.2d; the parameter to note here is the height of CB $[n]$  which does not change with the number of monomers in the ring.

### 3.2.1 Guest-host assembly of CB $[n]$

Binding of the guest molecules inside CB $[n]$  is determined by three key parameters. Two parameters already mentioned above are the hydrophobic pocket and the physical dimensions of the pocket volume. The third driving parameter for the formation of a guest-host complex is the enthalpic and entropic change during the replacement of high-energy water molecules present inside the pocket by the guest molecules [107]. For example, methylene blue (MB) molecules spontaneously get encapsulated inside CB[7] and CB[8] with large binding constants  $10^6 - 10^7 \text{M}^{-1}$  and  $10^{13} - 10^{14} \text{M}^{-2}$  respectively. Hydrated MB molecules in water displace high energy water molecules present in CB[7] and CB[8] resulting in the formation of a guest-host complex.



<sup>1</sup>CB $[n]$  molecules utilized in this study are synthesized by author's collaborators at Prof. Oren A Scherman's group, Melville Laboratory for Polymer Synthesis, University of Cambridge, Cambridge, UK

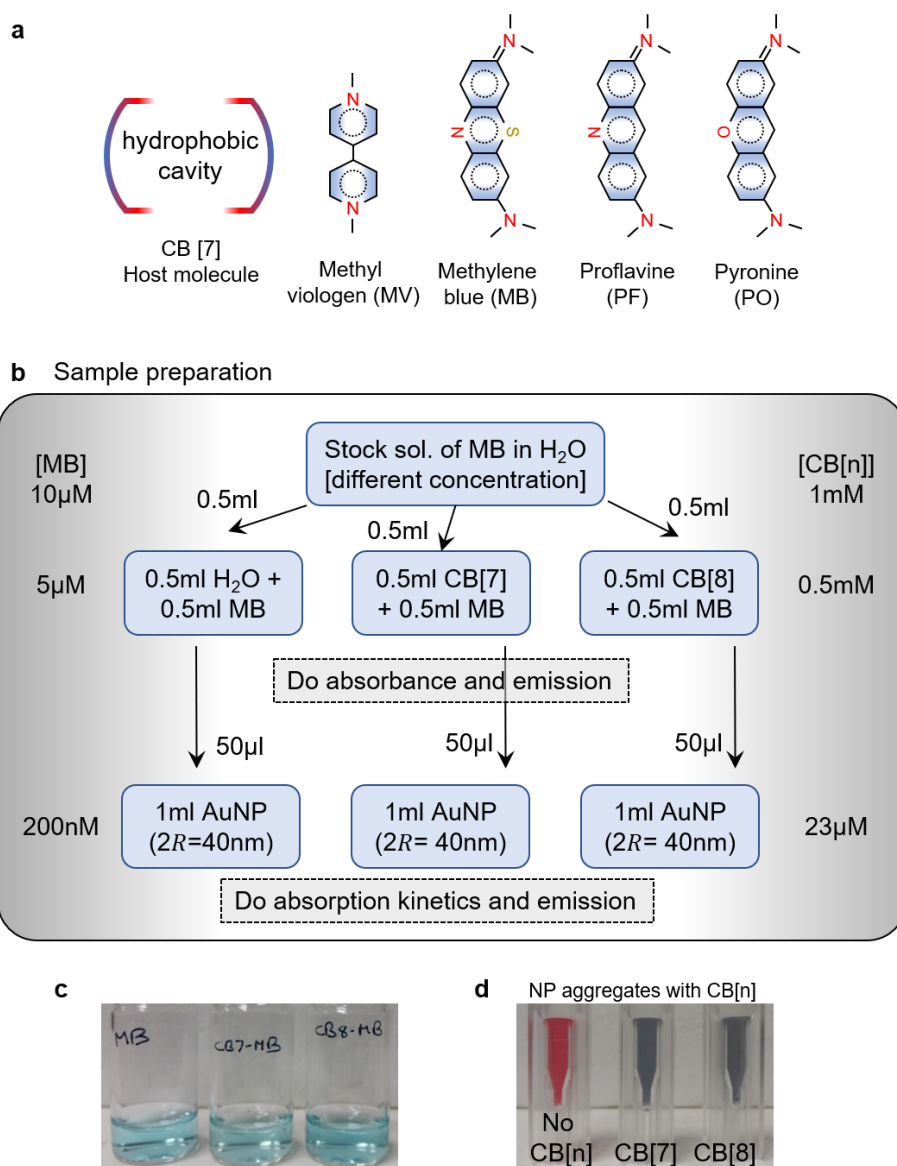


Figure 3.3: **Guest-host complex of CB[7]**. (a) Chemical structure of different guest molecules encapsulated inside CB[n], in which hydrophobic and hydrophilic parts are colour coded with blue and red. (b) Assembly of MB guest molecule inside CB[7] and CB[8], the final molar concentration of MB and CB[n] presented at left and right side. (c) Photographic images of MB in water, MB encapsulated in CB[7] and CB[8]. (d) Photographic images of Au NP aggregates formed on assembling with CB[n]-MB complex and compared with non-aggregated Au in water.



This change in enthalpic and entropic values gives rise to a gain in Gibbs free energy resulting in the formation of the complex. For the CB[7] complex, the gain from water expulsion is the largest compared to other CB[*n*] members, because CB[7] has the highest number of high energy molecules in the pocket whose energy is also remarkably large compared to bulk water. Most of the assembly is done in water medium and in the following section I discuss the experimental procedure used in creating the self-assembly of CB[*n*]-guest complexes on Au surfaces.

### 3.2.2 Sample preparation

Stock solutions of CB[*n*] are prepared at 1 mM concentration in ultra-pure water. The limited solubility of CB[*n*] hinders the preparation of highly concentrated (>5 mM) solutions, especially for CB[8] samples. The solubility is enhanced by incorporating a polar-guest molecule into CB[*n*]. To encapsulate the guest into CB[*n*], appropriate concentration of guest molecules dissolved in water is mixed with CB[*n*] solution (Fig. 3.3a). The concentration of the guest molecule is chosen in such a way that the resultant mix has CB[*n*]:guest ratio in the range of 10:1 to 100:1, which ensures that CB[*n*] is excess in the solution and most of the guest molecules are inside CB[*n*] (Fig. 3.3b). To ensure the proper formation of a guest-host complex, the mixed solution is sonicated for 5-10min. Different sets of guest molecules are encapsulated in CB[*n*]. The photographic images of samples of MB encapsulated in CB[7] and CB[8] are shown in Fig. 3.3c.

### 3.2.3 Optical properties of the guest-host complex

The formation of the guest-host complex is confirmed via optical absorption spectroscopy (Fig. 3.4a). MB in water has a strong absorption band at ~665 nm corresponding to  $n - \pi^*$  transitions accompanied by a weak shoulder peak at ~620 nm from the 0-1 vibronic transition. The strong absorption below 650 nm observed in the experiment (Fig. 3.4b) corresponds to the aggregation of MB at these concentrations [110]. As a cationic dye, MB undergoes face-to-face (H-) aggregation which results in a strong absorption at 605 nm for dimeric forms and at 575 nm for trimeric forms. The equilibrium constants for these aggregates are reported to be  $10^4$ - $10^6$  Lmol<sup>-1/2</sup> in water [110].

These aggregates are well separated by encapsulation in CB[7], as each CB[7] can accommodate only one MB [111] (Fig 3.4c,e). This is also reflected in the absorption

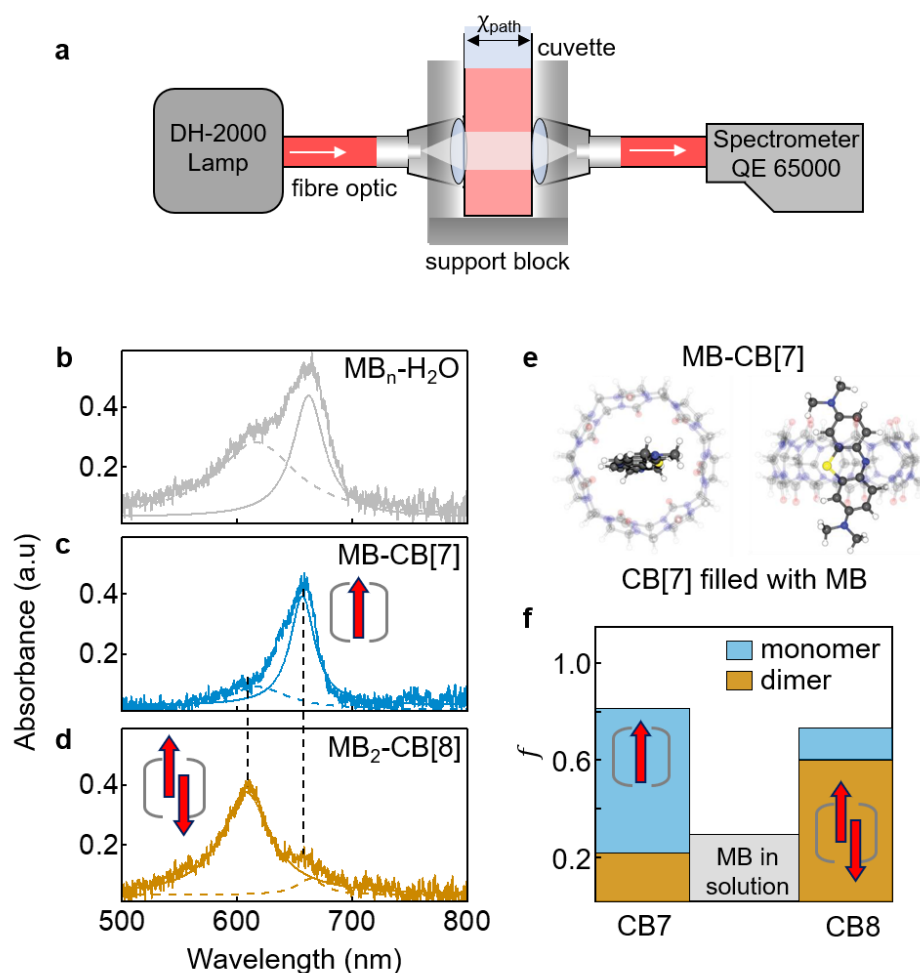


Figure 3.4: **Monitoring formation of guest-host complex.** (a) Optical extinction setup used. (b-d) Absorption of MB in (b) water without any CB[n] and MB in complexed form with (c) CB[7] and (d) CB[8]. (e) Top and side view of MB encapsulated in CB[7]. (f) Fraction of MB in monomeric and dimeric form on encapsulation with CB[n] and in water.

spectrum with suppressed dimer and trimer peaks [112]. However, CB[8] forms association with two MB molecules aggregated in a sandwich type of structure [113], resulting in a strong absorption band at 610 nm (Fig. 3.4d) along with a weak absorption associated with the monomeric form. From the intensities of these absorption bands, the fraction of MB in monomeric and dimeric forms in CB[ $n$ ] are extracted. More than 80% of MB is present in the monomeric form in CB[7] sample, whereas CB[8] sample contains more than 60% of the dimeric form. This kind of isolation of emitter is crucial for single-molecule studies, where optical properties are not mixed with disordered aggregates.

### 3.2.4 Assembly of CB[ $n$ ] on Au surfaces

CB[ $n$ ]s encapsulated with guest molecules are assembled on Au surfaces linking spherical nanoparticles and Au films via electrostatic interactions of the CB[ $n$ ] portal [115, 116]. The CB[ $n$ ] binds to Au with the carbonyl portals at either end of the barrel structure flat to the metal surface. On adding CB[ $n$ ] to Au NP solution, CB[ $n$ ] binds to Au surface and 'glues' the nanoparticles. So, CB[ $n$ ] acts like a binding linker to bridge Au nanoparticles. In solution with excess CB[ $n$ ], Au nanoparticles aggregate to form a large fractal-like structure with gap size controlled by the CB[ $n$ ], which is 0.9 nm. This aggregation process is monitored by extinction spectroscopy (Fig. 3.5a,b), in which the plasmon absorption band at 535 nm gradually decreases with time, accompanied by the evolution of new plasmon modes due to the coupling between the nanoparticles (termed as chain modes). There is no difference between plasmon bands of aggregates formed from CB[7] and CB[8]. The SEM image of formed aggregates with 40 nm Au nanoparticles is shown in Fig. 3.5c with inset showing the gap size controlled with the size of CB[ $n$ ] molecule.

Similarly, CB[ $n$ ]s are assembled on a metal surface [51] (Fig. 3.5d). Here, atomically smooth gold substrates are prepared by e-beam evaporation of 100 nm gold layers onto a clean silicon wafer. This is then heated to 60°C, with epoxy glued to it and then cured, before peeling off to obtain an ultra-smooth gold surface. This gold coated substrate is submerged in a 1 mM solution of CB[7] in de-ionized water overnight to deposit a layer of CB[7] molecules or CB[7]-MB complexes. Further, 40-60 nm citrate-capped gold nanoparticles (purchased from BBI) are drop-cast onto the coated film where physisorption takes place and are rinsed with de-ionized water after 10 s to remove excess particles. The substrate is then blown dry using nitrogen, resulting in nanoparticle-on-mirror cavities with CB[7]-MB molecule assembled in the gap.

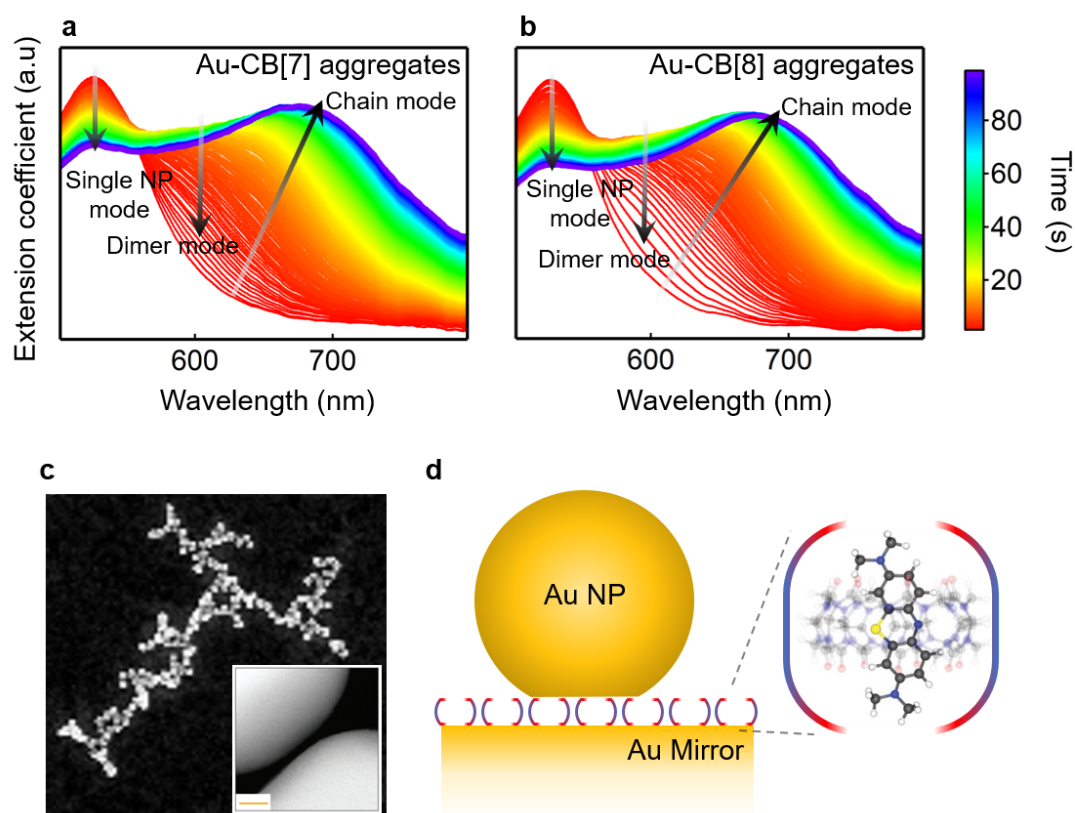


Figure 3.5: **Assembly of CB[n] on Au surface.** (a,b) Time resolved extinction spectrum monitoring the formation of Au-NP aggregates on addition of (a) CB[7]-MB and (b) CB[8]-MB<sub>2</sub>. (c) SEM image of formed aggregates from 40 nm Au-NP with CB[7]. Inset showing the gap 0.9 nm formed between the two nanoparticles, reproduced from [114]. (d) Diagrammatic representation of nanoparticle on mirror system with CB[7] molecules assembled on the Au surface, inset showing the chemical structure of CB[7]-MB complex.

### 3.3 DNA origami

Guest-host complexes with CB[ $n$ ] provide sub-nm plasmonic cavities and well-assembled molecules in the gap with a great degree of molecular orientation control. However, the molecules are distributed stochastically on the surface. Various techniques [117] exist to control the location of a single emitter beyond random deposition such as, (i) chemical modification/functionalization of the substrate [118], (ii) placement by scanning probes in scanning tunneling- or atomic force microscopes (AFM), (iii) electrostatic trapping [119], (iv) capillary forces in solvent evaporation [120, 121] and (v) host-guest chemistry [116, 122]. However, each of these methods suffer from inherent issues of randomness, coupled with low-yield and difficult scalability.

Here, I also utilize deterministic bottom-up nanoassembly combining both organic and inorganic components, using deoxyribonucleic-acid origami (DNAo) nanotechnology [123–128]. A long single strand of DNA termed the scaffold is folded by the complementarity of base-pairs along hundreds of much shorter DNA ‘staple strands’. These are designed to uniquely bind two or more sections of the scaffold together, while pinning different subcomponents to the staple strands yielding DNA ‘breadboards’ that can carry different functional elements [129–137]. I combine two robust methods to form NPoM cavities with DNAo breadboard spacers<sup>2</sup>.

The DNAo is designed as a 2-layer plate (Fig. 3.6a), each layer consisting of 24 helices having 128 to 149 base pairs [138]. The bottom layer has 4 thiol modifications on specific staple strands which are used to bind the origami onto the flat Au mirror. The top layer contains 6 poly-A (10 adenine bases on the 3’) overhangs which can bind to the nanoparticle. The overhangs are designed to form a hexagon with the mid-point labelled (0,0) so that ssDNA-coated-nanoparticles hybridize to locate the centre of the nanoparticle bottom facet. The origami are folded in a 14 mM MgCl<sub>2</sub>, 1x TE Buffer using a 7560-base long single stranded viral DNA scaffold isolated from M13mp18 derivative (*Tilibit nanosystems*) at a concentration of 10 nM and a staple concentration of 100 nM (i.e. 10:1 staple: DNA). The folding is carried out using an annealing cycle that slowly cools the solution from 90 °C to 4 °C over a period of 23 hours. Once the cycle is complete, the solution is filtered through a 100kDa *Amicon* filter in a 2 mM MgCl<sub>2</sub>, 0.5x TBE washing the buffer thrice.

---

<sup>2</sup>DNAo spacers used in this work are assembled in collaboration with Prof. Ulrich F Keyser’s group at Cavendish Laboratory, University of Cambridge, Cambridge, UK

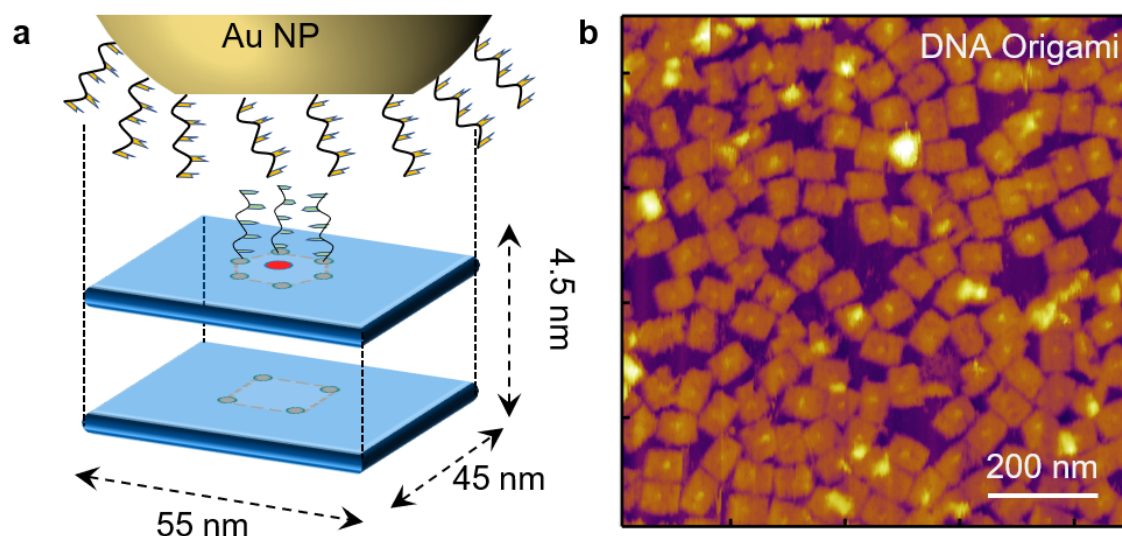


Figure 3.6: **DNA origami assembly.** (a) Design of DNA origami (DNAo), with dimensions shown. Blue rectangles indicate each layer of the DNAo plate. Bottom layer has four thiolate staples (grey circles) and the top layer has six overhangs to hybridize with ssDNA bound to the nanoparticle (not to scale). (b) Large scale atomic force microscopy (AFM) image of DNAo plates.

AFM images of these DNAo on Au surface confirm a uniform size distribution and high yield assembly (Fig. 3.6b). The  $\sim 2.5$  nm diameter of each helix [139] sets the position of the overhangs from this centre point (in nm) at  $(x, y)$  of  $(0, 5)$ ,  $(0, -5)$ ,  $(5, 2.5)$ ,  $(5, -2.5)$ ,  $(-5, 2.5)$  and  $(-5, -2.5)$ . Finally, 80 nm diameter Au nanoparticles functionalized with 5' thiol-modified 20x poly-T strands hybridize with the DNAo. The resultant assembly yields nanoparticles on a flat metal surface with the ultra-narrow gap (NPoM cavity) filled with DNA origami and a single-Cy5 molecule at the centre (Fig. 3.6d).

To optically address these nanocavities, I developed different microscopic setups having the capability to probe individual nanocavities.

### 3.4 Optical nanoscopy

To image and excite single nanoparticles in a NPoM system, an Olympus BX51 microscope combined with laser and white-light spectroscopy is used. This was reconfigured as a part of this thesis to Raman and dark-field spectroscopy on individual NPoM cavities. Further existing particle tracking codes were adopted to do automated nanoparticle scanning for

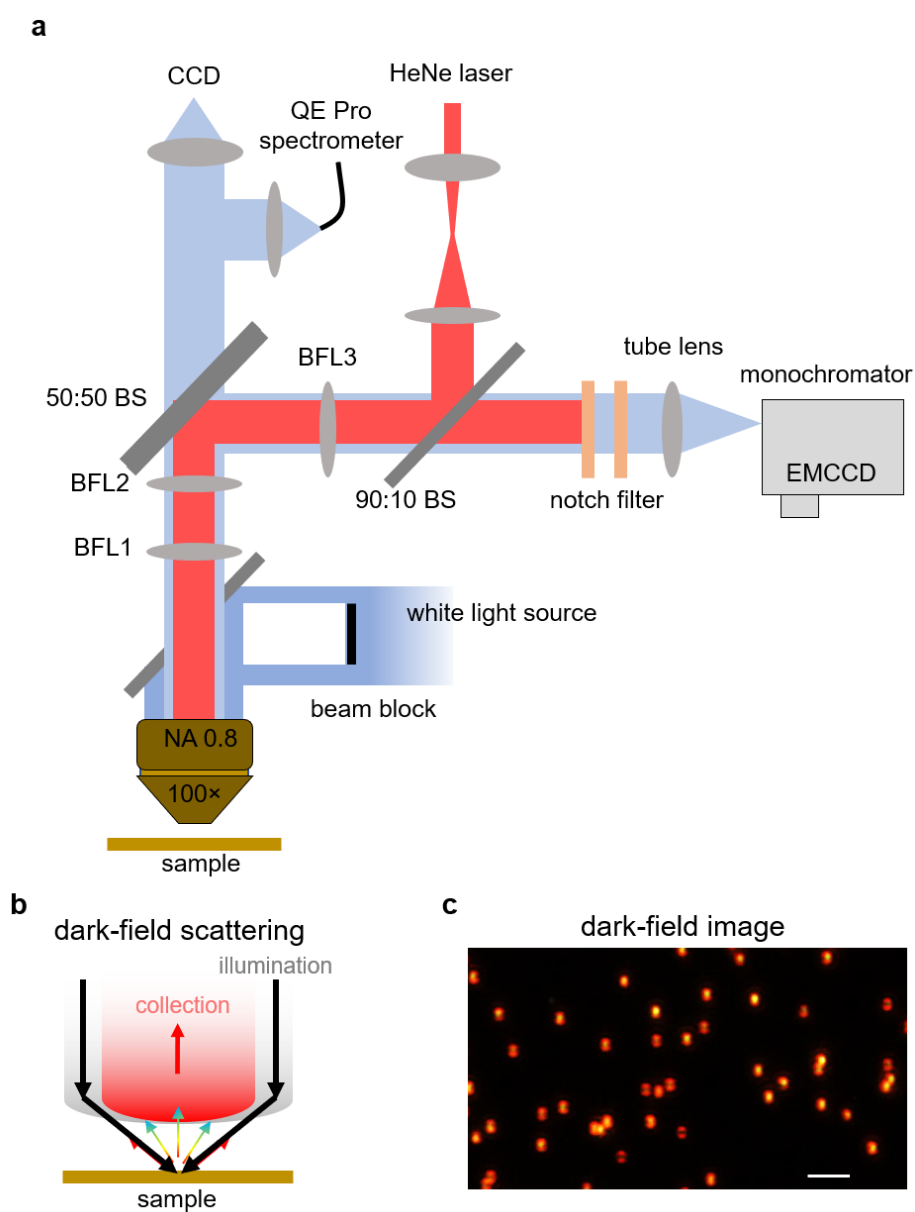


Figure 3.7: **Optical setup.** (a) Optical sketch of the dark-field and Raman spectrometer. (b) Schematic of the dark-field objective. (c) Dark-field image of NPoM sample, each spot represents the scattering from individual NPoM cavities.

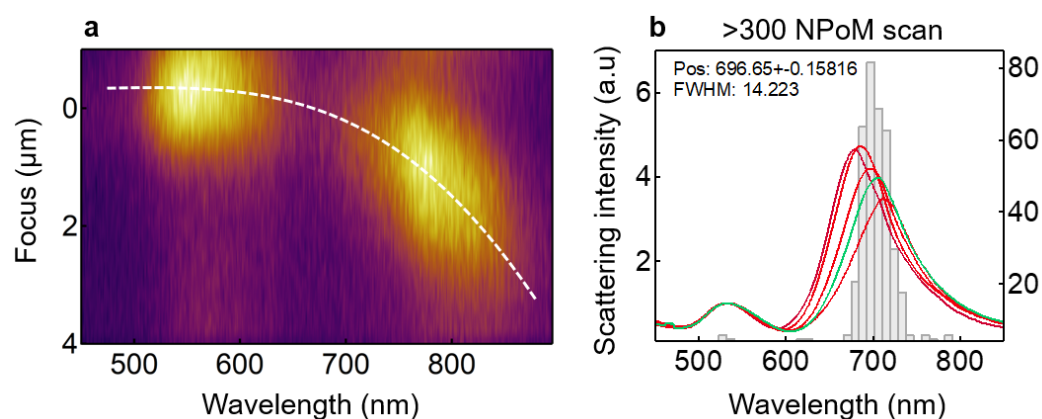


Figure 3.8: **NPoM dark-field scattering spectroscopy.** (a) Scattering spectra obtained from NPoM cavity at different focus, indicating chromatic corrections at longer wavelengths. The dashed line represents the ideal focal height for each wavelength. (b) Typical dark-field spectra obtained from >300 NPoM cavity from my automated particle tracking technique.

>500 NPoM cavities. The optical rig is equipped with Olympus LMPLFLN-BD objective with NA  $0.8\times 100$  which is used for both the spectroscopy and imaging (Fig. 3.7a). To characterize the resonances of NPoM cavity a wavelength-dependent light scattering technique is exploited in a dark-field configuration.

### 3.4.1 Dark field spectroscopy

Nanoparticles in the NPoM system scatter light at the resonant frequency of the cavity. To image and perform spectroscopy on individual nanoparticles, the outer-ring of the dark-field objective was illuminated with collimated white-light (halogen source). Corresponding to the high NA of the excitation ring, only the scattered light from each NP is collected by the objective lens. The excitation and collection angles measured from the optical axis are  $0^\circ$ - $53^\circ$  and  $53^\circ$ - $56^\circ$ . This scattered light is collected through a  $50\ \mu\text{m}$  multi-mode fibre and routed to an OceanOptics QEPro spectrometer (cooled to  $-22^\circ\text{C}$ ).

The wavelength-dependent scattering intensity needs to be referenced with the response from the white light lamp to obtain the response of the NPoM cavity. This referencing is done by collecting the scattered light from a white-light diffuser. The dominant intensity scattered by the diffuser is collected at the angles along the optical axis, however the NPoM cavity need not scatter light in this normal direction. This is especially true when the NPoM cavity scatters at longer wavelength and at high angles, at which chromatic aberration of the objective lens is high, resulting in different wavelengths



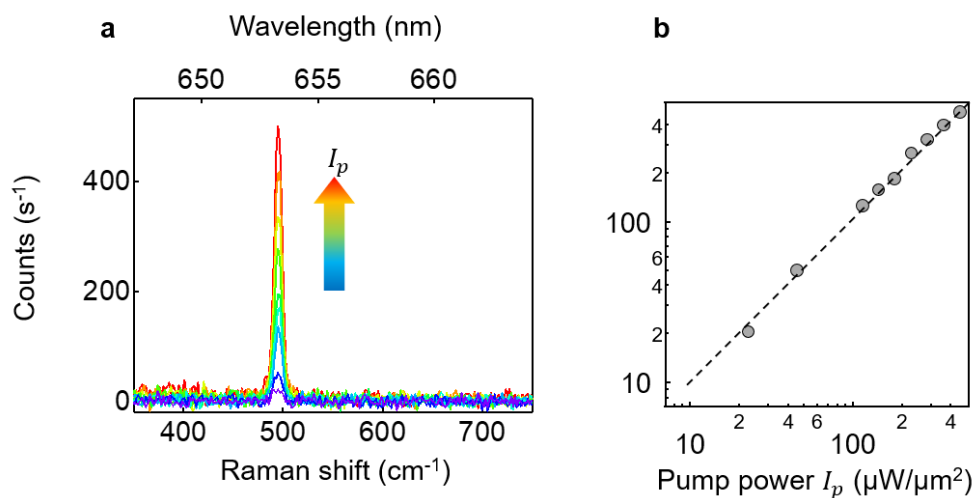


Figure 3.9: **Power reference measurements on silicon.** (a) The variation in Raman spectra of phonon mode of silicon with varied pump power. (b) The linear variation of peak intensity with increasing pump power for the Si 512 cm<sup>-1</sup> peak.

effectively collected at different heights. To circumvent this issue, I acquire series of spectra at different focus heights (Fig. 3.8a) and final scattering spectrum is obtained from adding intensities from an ideal focal height for different wavelengths. In special cases where an accurate ratio of different peaks from the NPoM cavity spectrum are needed, similar calibration is required for the lamp response. As the white-diffuser is not a point scatterer like the NPoM cavity, collecting spectra at different focus heights does not help. To account for this, light scattering from a 50  $\mu\text{m}$  glass microsphere is used. By changing the focal height, light is reflected at different angles from the microsphere surface, providing accurate referencing for the NPoM cavity.

### 3.4.2 Electronic and Raman scattering

To pump the molecule placed in a NPoM cavity, the above setup is equipped with a helium-neon (HeNe) laser of wavelength 632.8 nm (Fig. 3.7a), and the laser is expanded to fill the back aperture of the objective lens. Back-scattered light from the sample is collected from the same objective and routed to an Andor Shamrock i303 spectrograph after filtering the laser line with the two notch filters with OD > 6. The light is dispersed with a 600 lines/mm grating and the spectrum is recorded with an Andor Newton DU970P-BVF EMCCD (cooled to  $-90^\circ\text{C}$ ). The power density of the laser on the sample is controlled with a Thorlabs FW212CNEB automated filter wheel with twelve neutral density filters, such

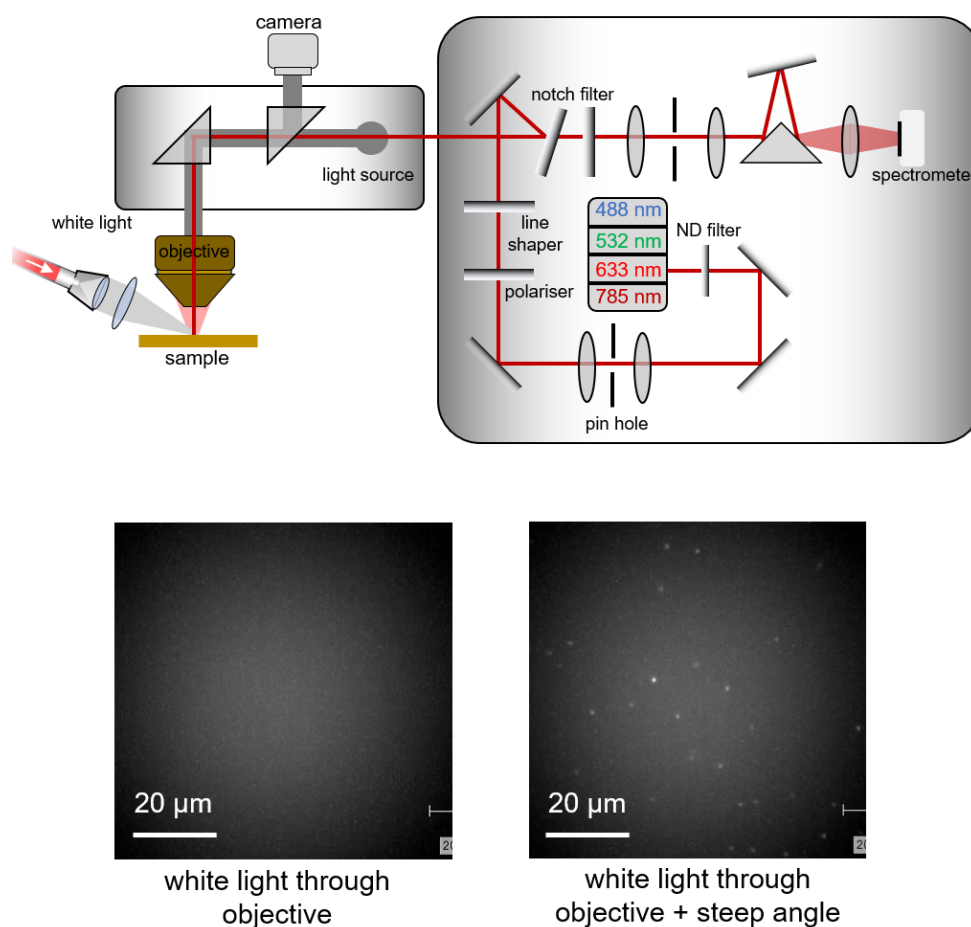


Figure 3.10: **Multi-wavelength excitation setup.** (top) Setup of the Renishaw inVia Raman microscope coupled with side white-light illumination. (bottom) Optical images obtained from 50x long working objective without and with white-light illumination from side.

that the resulting power on sample varies between  $20\text{--}400\ \mu\text{W}/\mu\text{m}^2$ . Thus the reference measurements were done on silicon (Fig. 3.9). The intensity of photon mode at  $512\ \text{cm}^{-1}$  varies linearly with increasing pump power.

Experiments with multi-wavelength excitation were performed on an Renishaw inVia Raman microscope (Fig. 3.10), with available wavelengths of 244 nm, 488 nm, 532 nm, 633 nm, and 785 nm. For the work presented in this thesis, I utilize 532 nm, 633 nm and 785 nm lines. A simple dark-field illumination setup was developed for identifying nanoparticles in an easy manner. The excitation light provided by a fibre coupled white light source was injected to the sample from the side at steep angles. Small nanoparticles with diameter  $<60\ \text{nm}$  are identified as bright scatterers, only in the presence of this light.

## 3.5 Electromagnetic modelling

An important toolbox for the understanding of optical properties of metallic nanoparticles is the numerical modelling of electromagnetic fields. Here, objects are discretized into small elements and Maxwell's equations are solved numerically for each element. I use commercial Finite-Difference Time-Domain (FDTD, Lumerical) package for the modelling.

### 3.5.1 Scattering from NPoM cavities

To model the scattering from a NPoM cavity, the gold or silver nanostructure was modelled as an appropriate geometry on top of an infinite dielectric sheet of thickness  $d$ . Underneath this sheet, a 200 nm thick gold layer was placed in order to replicate the experimental NPoM geometry (Fig. 3.11 left). The dielectric function of gold was taken from Johnson and Christy [25] and the material function for silver was taken from Palik. The real refractive index of the dielectric sheet was varied depending on the experimental parameters. The NPoM was illuminated with a s- and p-polarized plane wave from an angle of incidence of  $\theta_i = 55^\circ$ . The scattered light was then collected within a cone of half-angle  $\theta_c = 53^\circ$  based on the numerical aperture of the objective. The resulting spectra were incoherently added in order to obtain an unpolarized scattering response as was measured experimentally.

In Lumerical, the angle of incidence of the impinging light pulse is controlled through the magnitude of the  $k$ -vector in the  $y$ -direction (Fig. 3.11 right). Since the  $k$ -vector is also a function of wavelength, excitation using a broadband pulse results in changes in the angle of incidence within the frequencies of the pulse. This prohibits a constant angle of incidence during a frequency sweep for our excitation angles of  $55^\circ$ . To account for this, a narrow pulse for each desired frequency point can be used and the entire problem is solved for each frequency point, a computationally rather expensive strategy.

### 3.5.2 Enhanced decay from point dipoles

To calculate the enhanced decay rates of the molecule in a NPoM cavity and to estimate the mode volume, the Purcell factor (from Chapter 2.8.1) method is utilized. This Purcell factor describes the enhanced radiative and non-radiative decay rates of a classical dipole in the NPoM cavity. This is simulated by placing dipoles in specific orientations either at the centre of the facet or at the edge, near the top nanoparticle where the fields are

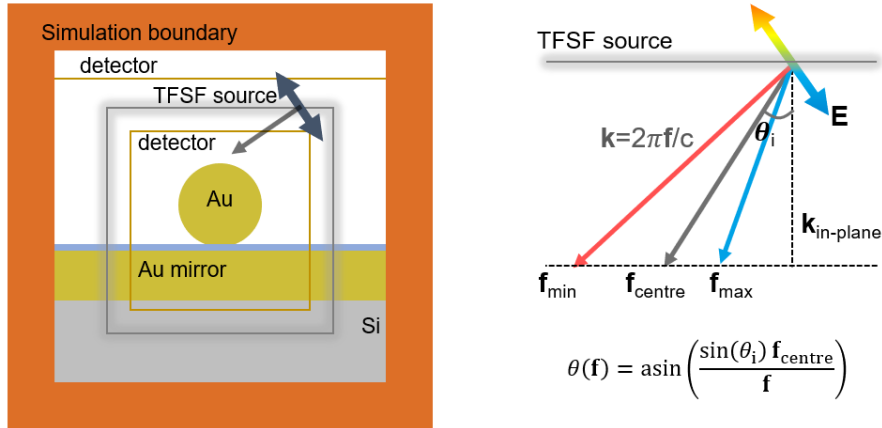


Figure 3.11: **Lumerical FDTD simulation setup.** (left) Schematic of NPoM system along with the source, detector and simulation boundaries (not to the scale). (right) Generation of a light pulse in Lumerical, showing the variation in the angle of incidence for a broadband incident pulse.

strongly enhanced. The mode volume for each mode was subsequently extracted from this calculation and from the  $Q$ -factor obtained from the resonant lineshape, as described in the section above (Sec. 3.5.1).

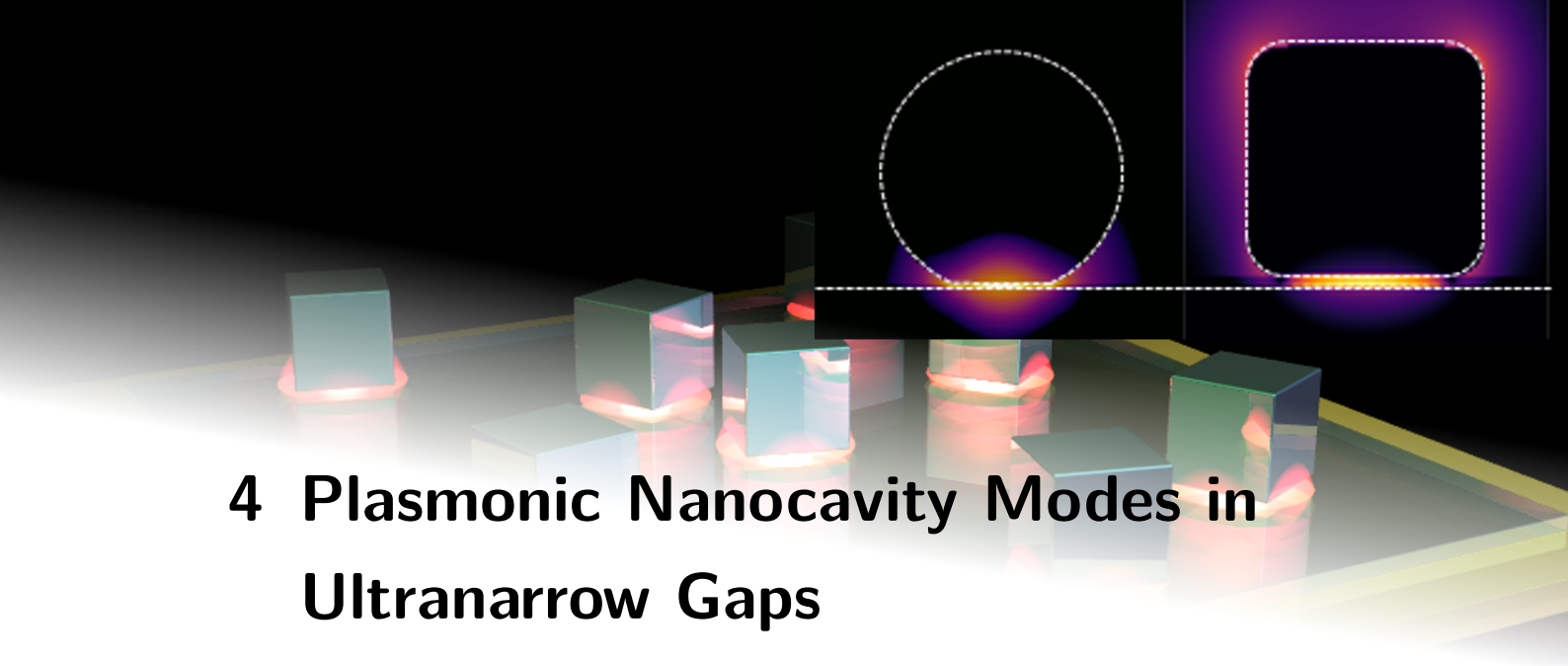
### 3.5.3 Strong coupling from Lorentz absorbing materials

To simulate the strong coupling with molecules, the gap of the NPoM cavity is modelled as a self-consistent dispersive medium with excitonic dielectric permittivity described by the Lorentz model as,

$$\epsilon_{\text{tot}}(\omega) = \epsilon_{\infty} + \sum_j \frac{f_j \omega_j^2}{\omega_j^2 - \omega^2 - i\gamma_j \omega} \quad (3.4)$$

where  $\epsilon_{\infty}=1.96$  is the non-resonant background. For each exciton  $(A,B)$   $f_j$  is the reduced oscillator strength and  $\hbar\omega_{A,B}$  are the  $A,B$  exciton energies with linewidth parameters  $\gamma_{A,B}$  tuned to match the experimentally observed values from absorption measurements.

To summarize, in this chapter I have introduced different experimental and theoretical methods used in this thesis. Especially, guest-host assembly of molecules and their binding to metal surfaces resulting in NPoM cavity is demonstrated. Further the optical properties of assembled structures are measured by scattering and absorption spectroscopy methods. Experimental results are further corroborated with numerical simulations and the details of these simulations are introduced.



## 4 Plasmonic Nanocavity Modes in Ultranarrow Gaps

Plasmonic nanocavities with sub-5 nm gaps between nanoparticles support multiple resonances and possess ultra-high-field confinement and enhancements. The precise structural details of nanogaps dramatically modify the plasmonic response, producing a complex pattern of confined electromagnetic modes that can be directly observed in scattering experiments. Here I systematically compare the two fundamentally different resonant gap modes: transverse waveguide ( $s$ ) and antenna modes ( $l$ ), which, despite both tightly confining light within the gap, have completely different near-field and far-field radiation patterns and strengths. By varying the gap size, both experimentally and theoretically, I show how changing the nanoparticle shape affects the hybridization of  $s$  and  $l$  modes.

## 4.1 Need for plasmonic nanocavities

Light confinement between nanoplasmonic components is now possible in nanoscale gaps and provides exquisitely sensitive spectral information about the realm of sub-nanometre structures. The unprecedented strong field enhancement in nanoscale gaps allows access to real-time measurements of the movement of atoms and molecules [140]. As discussed in Chapter 2, a promising route towards controlling plasmonic nanogaps is by the nanoparticle-on-mirror (NPoM) geometry. Large numbers of plasmonic nanogaps can thus be obtained in a controllable and reproducible manner. However, the exact geometry of the overlying NP strongly modifies the optical response of this system, making it a subtle optical monitor of atomic-scale modifications. As most of the NPs are faceted with different crystalline planes, the bottom surface geometry of the NP facing the underlying mirror supports different sets of bright modes (scatters light to far-fields) and dark modes (does not scatter light). Certain sub-sets of dark-modes sharing similar field symmetries as bright modes will strongly mix with bright modes in the near-field and scatter light with a different phase into the far-field, resulting in a complex envelope of multiple modes at similar wavelength. In the light of coupling optical emitters to plasmonic cavity modes, it is important to understand local field strengths, far-field cross sections, losses due to damping, and spatial charge distributions across the geometry for both bright and dark modes.

In this chapter I discuss the following questions:

- ⇒ How to estimate resonance energies of bright and dark modes?
- ⇒ How does different facet size and shape modulate these energies?
- ⇒ When and how do these modes mix with bright modes?
- ⇒ What determines their coupling strength?
- ⇒ How to decompose these modes from a complex spectrum?
- ⇒ How to quantify different parameters to define a figure of merit estimating the coupling coefficient for a single optical emitter?

## 4.2 Confined waveguide and cavity modes

In a nanoparticle-on-mirror (NPoM) geometry, a metallic nanoparticle is brought to interact with its mirror image in an underlying metal film. Thin dielectric spacers between the two

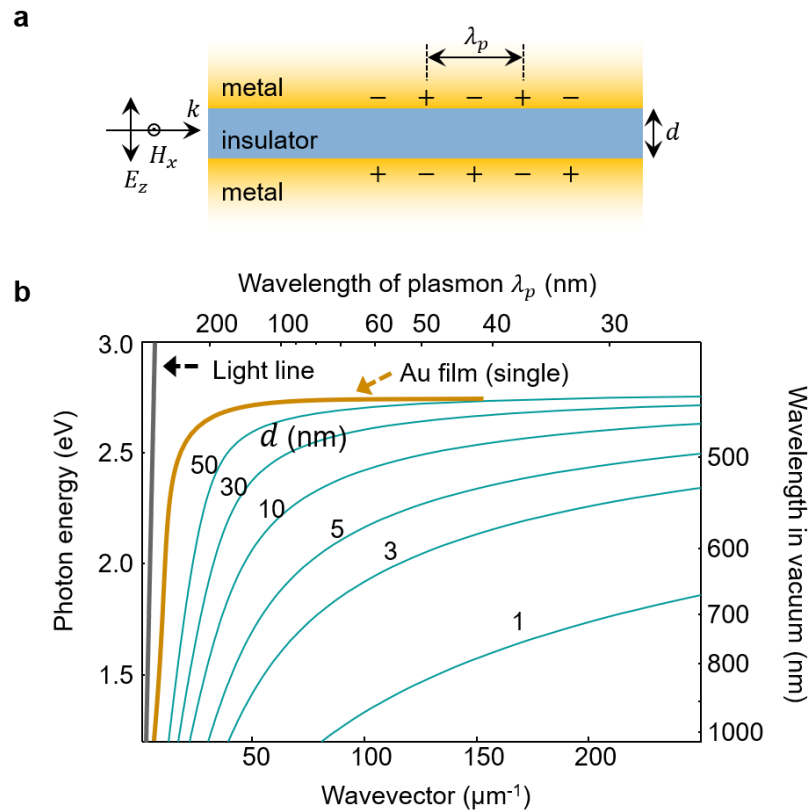


Figure 4.1: **Metal-insulator-metal (MIM) waveguide modes dispersion.** (a) Schematic of MIM structure with variable insulating material (refractive index of 1.5) sandwiched between two infinite metal (Au) surface. (b) Dispersion of MIM modes for variable gap size ( $d= 50, 30, 10, 5, 3$  and  $1$  nm) is compared with photon and propagating SPP mode on a planer Au surface.

metallic interfaces are usually introduced to prevent conductive contact. In comparison to a single spherical NP, tightly coupled plasmonic components support different cavity modes confined to the gap between them.

1. Transverse waveguide cavity modes ( $s_{ij}$ ) where fields propagate parallel to the flat interfaces and reflect at the facet edges (as for Fabry-Perot modes), lead to coherent interference with characteristic standing-wave patterns.
2. Longitudinal antennae modes ( $l_{1,2,\dots}$ ) are the coupled charge oscillations of the NP with the image charges in the mirror that radiate efficiently. These modes are mixed and radiate at specific angles depending on the exact geometry.

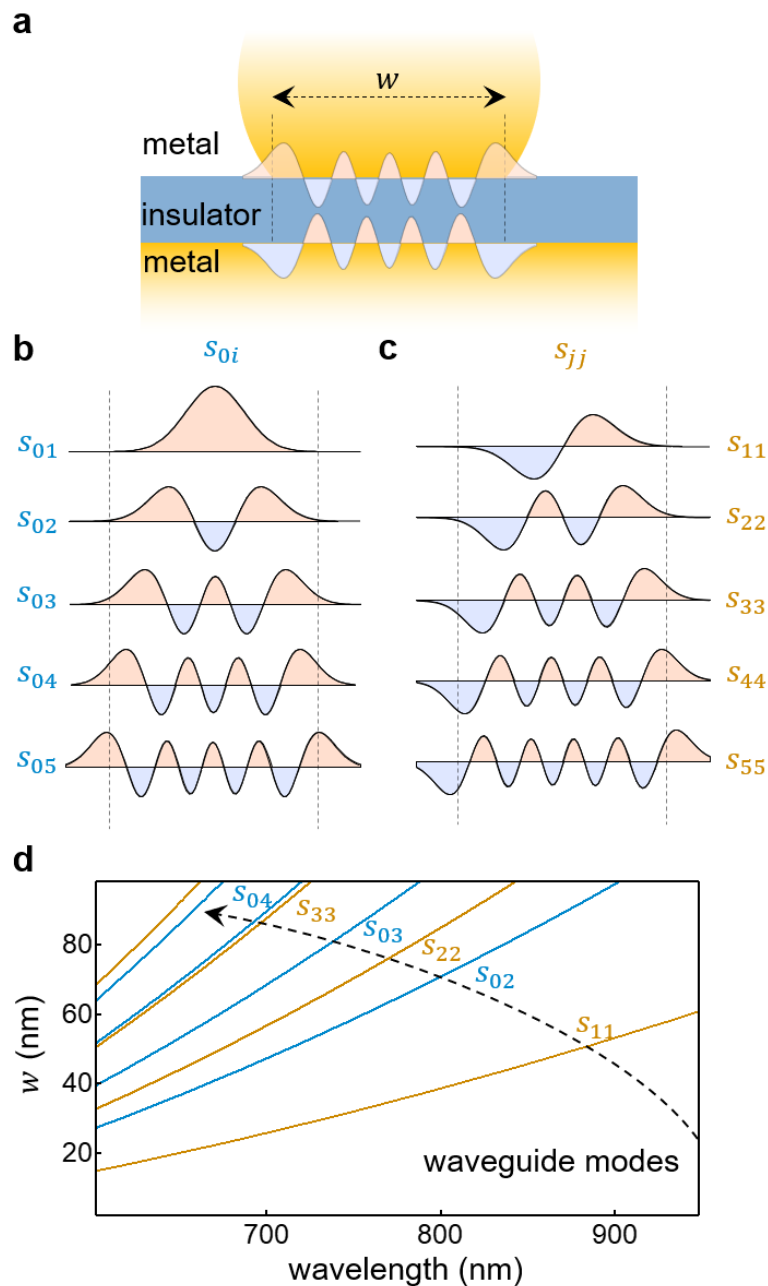


Figure 4.2: **Confined metal-insulator-metal (MIM) waveguide modes.** (a) Schematic of a faceted NPoM with charge oscillations for  $s_{05}$  mode. 1D MIM waveguide with boundary conditions defined by the facet size supporting modes with antinode (b) and node (c) at the centre of NPoM. (d) Dispersion of MIM waveguide modes for varying facet size. The modes are calculated for NPoM with  $D = 100\text{nm}$ ,  $d = 1\text{nm}$  and  $n_d = 1.45$ .



### 4.2.1 Transverse waveguide cavity mode

The NPoM with facets forms metal-insulator-metal (MIM) cavity with boundary defined by a (for now) circular facet. The dispersion of cavity modes ( $s_{ij}$ ) as a function of facet length  $w$  is calculated based on the MIM waveguide dispersion  $E(k_{||})$  with a gap distance  $d$  as,

$$\tanh\left(\frac{\beta_d d}{2}\right) = \frac{\epsilon_d \beta_m}{\epsilon_m \beta_d} \quad (4.1)$$

where  $\beta_{m,d} = \sqrt{k_{||}^2 \epsilon_{m,d} - k_0^2}$  and  $\epsilon_d$  ( $\epsilon_m$ ) is the dielectric permittivity for the gap (metal). For very thin gaps ( $d < 10$  nm) [141–143] approximation of  $\tanh(x) = x$  can be used to obtain an analytical expression for MIM waveguide dispersion as,

$$\left(k_{||} \frac{\hbar c}{E}\right)^2 = \epsilon_d + \left(\frac{\gamma}{2}\right) \left[1 + \sqrt{1 + \frac{4(\epsilon_d - \epsilon_m)}{\gamma}}\right] \quad (4.2)$$

where  $\gamma = [(-2\hbar c \epsilon_d)/(E d \epsilon_m)]^2$  giving the effective waveguide refractive index,  $n_{eff} = \hbar c k_{||}/E$ , dependent on the dielectric constants  $\epsilon_m$  in the metal and  $\epsilon_d$  the gap dielectric. The dispersion of MIM modes is interpreted as the hybridization of propagating SPP modes when two metal-dielectric surfaces are brought closer to each other [144–147]. The dispersion of low energy modes is plotted in the Fig. 4.1. When the distance between two Au surfaces ( $d$ ) is large ( $> 50$  nm) the dispersion is not significantly different from a single Au surface. However, when  $d < 5$  nm the dispersion becomes flat with extremely small plasmon wavelengths ( $< 10$  nm i.e. deep ultraviolet wavelengths). Moreover the amplitudes of electric fields reach higher values due to an increase in plasmon density of states (inversely proportional to the slope of dispersion curve). Further the decay of fields into metal ( $\delta_m$ ) defined as  $\delta_m = [\Re \sqrt{k^2 - (\omega^2/c^2)\epsilon_m(\omega)}]^{-1}$  where  $k$  is the wavevector, decreases by an order of magnitude.  $\delta_m$  drops to  $< 5$  nm for MIM modes with  $d = 1$  nm, compared with propagating SPPs on a single Au surface where  $\delta_m \sim 25$  nm. Thus, the wavelength along the direction of propagation is shortened significantly and does not couple well to the far-field.

In NPoM geometry, the facet width of the nanoparticle defines lateral discretization of these MIM waveguide modes resulting in solutions of different symmetry within the

cavities ( $s_{0i}$  and  $s_{jj}$  modes, Fig. 4.2). The resonance positions  $\lambda_{ij}$  of the cavity modes can be approximately analytically using [49],

$$\lambda_{ij} = \lambda_p \sqrt{\frac{\epsilon_d w}{d \alpha_{ij}} + \epsilon_\infty} \quad (4.3)$$

with  $\lambda_p = 137$  nm as the plasmon wavelength of Au in the Drude approximation with  $\epsilon_\infty = 10.5$  as the corresponding background dielectric permittivity while  $\epsilon_d = 1.63$ , for a given dielectric constant  $\epsilon = n^2$  and thickness  $d = 1.0$  nm. Here,  $\alpha_{ij} = \alpha'_{ij} + \phi$  is the argument of the  $i^{\text{th}}$  root of the cylindrical Bessel function of  $m^{\text{th}}$  order  $J_m$  and accounts for a simplified circular facet shape, where  $\phi = \pi$  is a phase-shift that accounts for the reflection of the cavity modes at the edges of the cavity.

While a full simulation is needed to find the exact spectral position of the resonant modes which reflect between the discontinuities at either end of this plasmonic MIM waveguide, simple indications can be extracted from this model. We can assume perfect reflection at each end, due to the strong mismatch in impedance within and outside the MIM plasmon waveguide. In practise, the phase shift on reflection and the reflectivity of the plasmon closely depends on the exact morphology at the facet edges (and this is likely seen in experiments with nanoparticles with geometries). However, full simulations show that the field stays slightly outside the facet area for such narrow gaps, and hence this is a reasonable assumption.

### 4.2.2 Hybridization with antenna mode

Optical antenna modes convert the freely propagating optical radiation into localized energy, and vice versa. The NPoM cavity couples light in and out via these antenna modes ( $l_1$  and  $l_2$  modes shown in Fig. 4.3a). These cavity modes possess charge on the top NP surface that facilitates the fields to couple in and out of the cavity (Fig. 4.3b,c) and exist for all facet sizes. As the facet size increases, the antenna modes shift to lower energy due to the increased interaction area (Fig. 4.3d, grey line). This red-shift ceases at  $w/2R \sim 0.3$  and blue-shifts occur for larger facets because of the reduced facet of the nanoparticle, which then represents a shorter antenna.

To investigate the interaction of these antenna modes with waveguide modes, antenna modes are modelled simply with a linear blue-shift (Fig. 4.3d, black line). Two different classes of waveguide modes ( $s_{jj}$  and  $s_{0i}$ ) exist, depending on their radial symmetry.

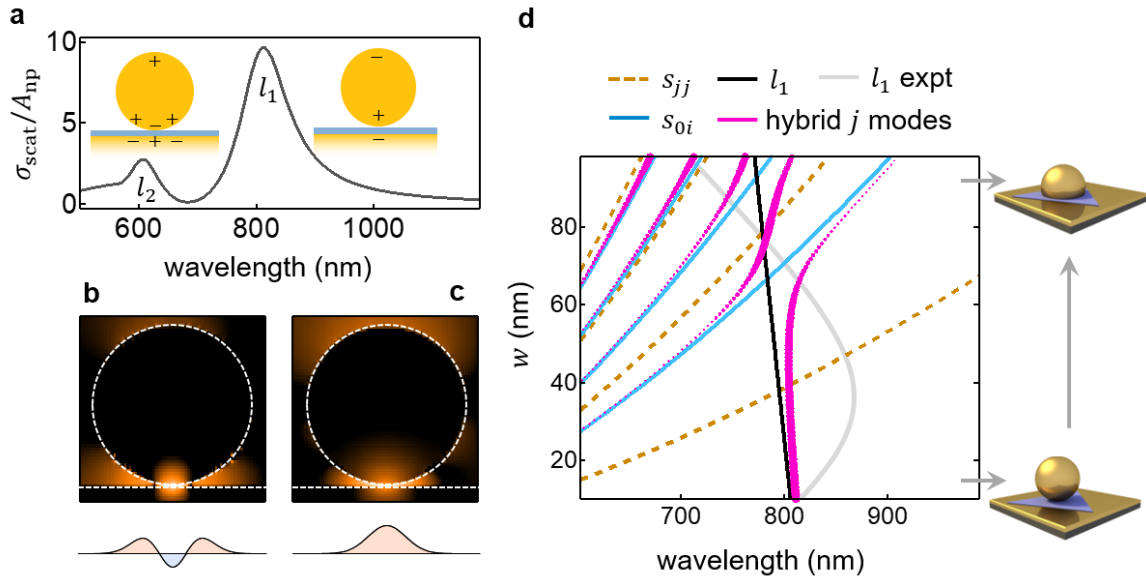


Figure 4.3: **Hybridization of antenna ( $l$ ) and waveguide modes ( $s$ ).** (a) Scattering spectrum for NPoM with a perfectly spherical nanoparticle with  $R = 50$  nm in a 1 nm gap. The two resonances  $l_1$  and  $l_2$  are the longitudinal antenna modes of the cavity with charge distribution shown adjacent. The charge on the top surface of the nanoparticle make these modes bright and accessible in far-field scattering spectroscopy. Near-field ( $E/E_0$ ) distributions for (b)  $l_2$  and (c)  $l_1$  modes, with line profiles at the middle of the gap shown below. (d) Evolution of different MIM modes (blue and orange lines) as the perfect sphere is transformed into a faceted sphere with increasing facet length ( $w$ ).  $l_1$  mode (black line) strongly hybridizes with  $s_{0i}$  modes (blue lines) resulting in the formation of new hybrid bright modes  $j$  modes (pink lines, intensity of the mode is indicated by the size of dots). The  $l_1$  mode does not mix with  $s_{jj}$  modes (orange dotted lines) so they remain dark and not generally observed in far-field scattering. (d) is replotted and modified from [148].

As seen in Fig. 4.3d, the waveguide modes with odd-order Bessel functions ( $s_{11}, s_{12}, \dots$ ; dashed orange curve) cross the antenna modes without any interaction, while the even-order waveguide modes ( $s_{02}, s_{03}, \dots$ ; blue curve) anti-cross the antenna modes. This is explained using the hybridization picture according to which, coupling of two plasmonic modes leads to hybridized modes (pink curve) of higher and lower energy respectively, and between them is a ‘forbidden gap’ at the crossing point. This anti-crossing is best identified for the  $s_{02}$  mode at a facet width of  $w/2R \sim 0.6$ . The  $s_{jj}$  waveguide modes are not radially symmetric and therefore do not couple to the radially symmetric antenna modes, crossing without interaction. However,  $s_{0i}$  waveguide modes share the same symmetry with antenna modes in the near-field resulting in their anti-crossing with each other. The coupling strength is determined by the contact angle between the nanoparticle facet and the substrate, which provides radiative outcoupling to the hybridized modes accessible in far-field.

This results in a complex set of multiple modes influencing optical properties at a given wavelength of interest. While several geometries have been reported in the literature, the question of which geometry is optimal for coupling light into emitters within these nanocavities remains unclear. To tackle this, parameters such as the local field strength, far-field cross sections, losses due to damping, and spatial charge distributions across the geometry need to be carefully analyzed. To understand how the individual modes influence these parameters, a suitable decomposition technique is required. Here, I address this issue by considering two extreme dimer nano-architectures based on cubes with sharp edges and spheres with smooth surfaces. A theoretical framework is also developed that provides ideal decomposition of the modes, which is used to quantify their different Purcell factors.

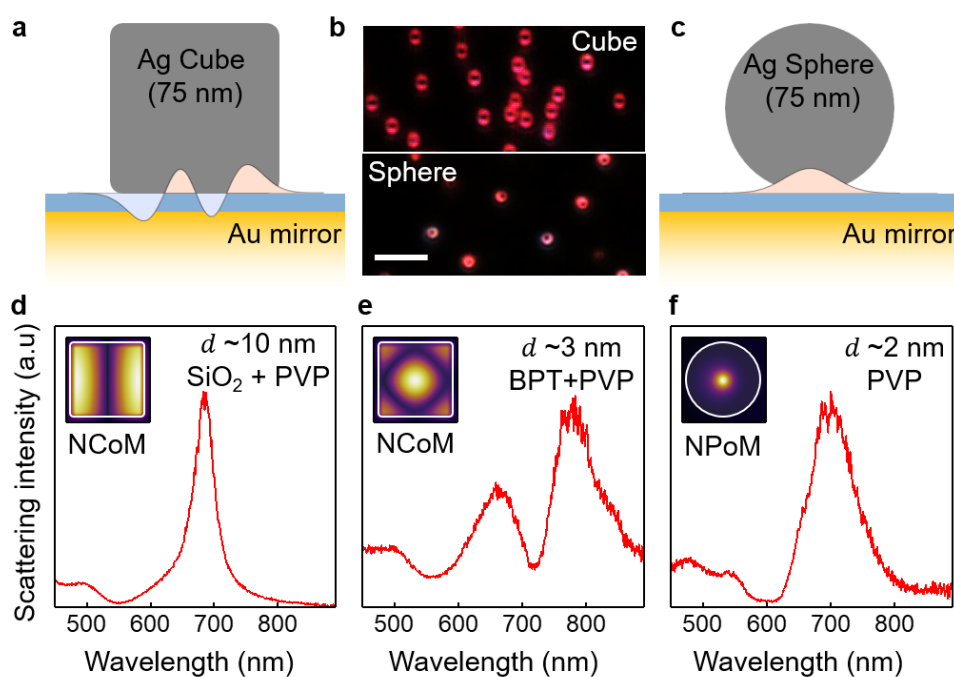


Figure 4.4: **Nanocube vs nanosphere image-dimers.** (a) Schematic of Ag nanocube with 75 nm edge length placed on template-stripped Au with sub-5 nm molecular gaps, supporting waveguide mode. (b) Optical dark-field images of (top) nanocubes and (bottom) nanospheres placed on Au mirror with BPT and PVP spacers respectively. (c) Schematic of NPoM, supporting strong antenna mode. (d-f) Scattering spectra from (d,e) 75 nm nanocubes with (d)  $d=10$  nm SiO<sub>2</sub> spacer, (e) 3 nm BPT spacer, and (f) nanosphere with 2 nm PVP spacer. Inset colour maps show normalized near-field intensity at the resonance wavelength, taken at the middle of gap; white lines indicate nanostructure edges.

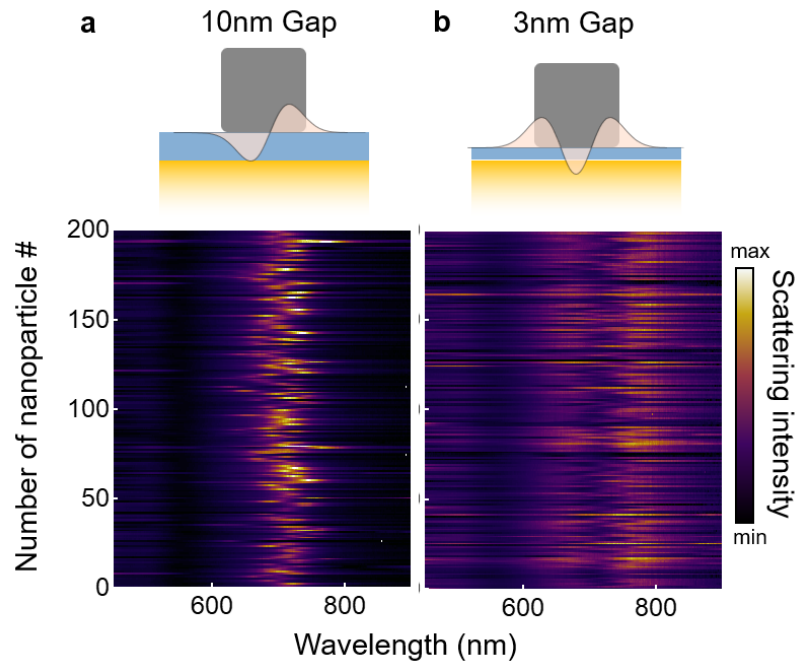


Figure 4.5: **NCoM modes at different gap.** Experimental scattering obtained for >200 NCoM for two different gaps (a) 10 nm SiO<sub>2</sub> spacer and (b) 3 nm gap of BPT+PVP spacer.

### 4.3 Nanocube vs Nanosphere-on-Mirror

Systematic comparison of near- and far-field optics of film-coupled nanocubes (termed nanocube-on-mirror, NCoM) and nanospheres (nanoparticle-on-mirror, NPoM) for sub-5 nm gaps (Fig. 4.4a-c) is performed here. Recent studies have shown that both these systems exhibit extreme nano-optics such as ultrafast photon emission from NCoMs [75] and strong-coupling from NPoMs in the single-emitter regime [149]. There are two fundamental parameters for a cavity which describe how well it enhances light-matter interactions. The quality factor ( $Q=\omega_c/\gamma_c$ ) describes how long a photon can be confined within the cavity and is calculated from the spectral width  $\gamma_c$  and the resonant frequency of the cavity  $\omega_c$ . The second parameter is the effective field localization  $V_{\text{eff}}$ , which characterizes the confinement of the cavity mode. Different power law scaling of  $Q$  and  $V_{\text{eff}}$  influences different optical phenomena and as shown, are influenced by the nanoparticle shape.

The fundamental (or lowest order) cavity resonance of the NCoM structure (seen in the near-IR with larger gaps in Fig. 4.4d and Fig. 4.5a) has  $Q \sim 30$  with strong field enhancements near the nanocube edges (inset Fig. 4.4d). By contrast, NPoMs have the

highest field confinement at the centre with broader resonances ( $Q \sim 15$ , Fig. 4.4f). For nanogaps below 5 nm the optical dark-field images of NCoMs and NPoMs both exhibit doughnut spatial profiles (Fig. 4.4b) which are characteristic of vertical radiating dipoles, confirming the coupling to image charges in the metal film. However, spectra of this collected scattered light exhibit completely different resonance features (Fig. 4.4e,f and Fig. 4.5b). The question of which resonance is the most effective for molecular nano-optics in such small gaps is the focus of this chapter.

As several resonant mixed modes can contribute to  $Q$  and  $V_{\text{eff}}$  at any given wavelength, it is not easy to understand their dependences without decomposing the observed peaks into fundamental modes. Therefore, I first show how to deconvolve the observed composite plasmonic modes of this nanoparticle-on-mirror geometry (focusing on the cube initially, as Chapter 2 describes the modes of a sphere) and analyze how these modes interfere in the near-field and far-field response using a symmetry-based eigenmode decomposition. I track these fundamental modes while tuning the gap size and obtain the deconvolved charge distributions for the two dominant lowest modes of cube NCoMs. I then show how these two modes evolve while transforming the cube NCoM into the sphere NPoM. It is found that different types of modes are involved, with waveguide modes closely confined to the gap and antenna modes with significant amplitude on the top of the nanoparticles. Finally, once I have pure charge distributions for these fundamental modes, I come back to the figures of merit for different modes to quantify which system is most effective for coupling to single molecules.

## 4.4 Characterization of nanocavity modes in cube NCoMs

To characterize the resonances of cube NCoMs with gaps below 5 nm, samples are fabricated with self-assembled monolayers of biphenyl-4-thiol (BPT) on template-stripped gold and then silver nanocubes (edge length 75 nm) assembled on top, resulting in NCoMs with gaps of 2-3nm (note that nanocubes are coated with 1-1.5nm thick poly(vinylpyrrolidinone) (PVP) on the surface). Dark-field scattering spectra from various such NCoMs (Fig. 4.5b) consistently exhibit two optical resonances, with average peak positions around 650 nm and 780 nm. Small variations in peak positions from nanoparticle to nanoparticle is associated with differences in nanoparticle size, PVP coverage and their edge rounding (see below).

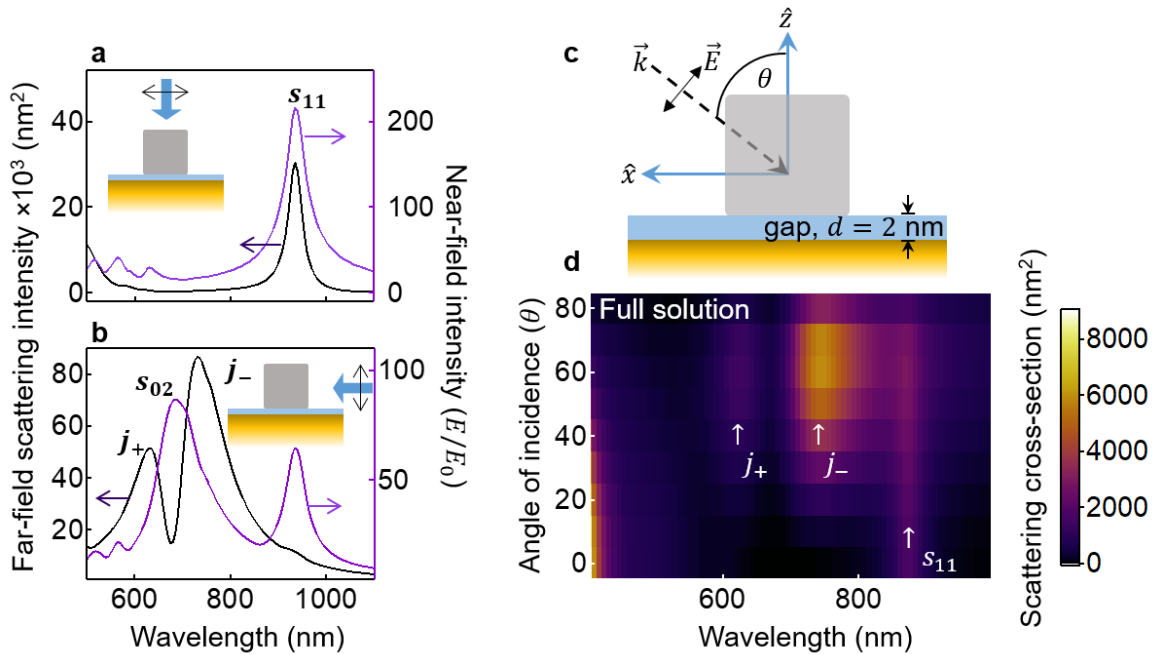


Figure 4.6: **Simulated nanocavity resonances of nanocube with 3 nm gap.** (a) FDTD scattering (black) and near-field spectra (purple) for 75 nm Ag cube on Au mirror with 3 nm gap of  $n=1.4$ , under normal (top) and perpendicular (bottom) illumination (insets). (b) BEM scattering full solution (orange) at  $55^\circ$  incidence, with projections from 1<sup>st</sup> (dashed green) and 5<sup>th</sup> (dashed gray) irreducible representations. (c) Charge distributions and decompositions at  $\lambda_s$  peaks in (b). (d) Amplitudes of  $j_{\pm}$  modes and charge distributions to  $\Gamma_1$  component. (e) Angle dependent far-field coupling pattern for  $s_{02}$ ,  $s_{11}$  modes.

Better insight is obtained using 3D finite-difference time-domain (FDTD) simulations (Fig. 4.6a). For normal illumination with electric field polarized parallel to the metal surface, only one resonance mode at longer wavelengths (600-1200nm) is observed in the far-field scattering spectrum (scattering intensity integrated over all directions). The same resonance mode is observed in the near-field and labeled  $s_{11}$  because its field profile shows charge oscillations between each edge of the nanocube indicating a transverse waveguide feature [150] (Fig. 4.4d inset). Illumination almost parallel to the metal film with electric field polarized perpendicular to the metal surface shows a completely different spectrum. The near-field still shows  $s_{11}$  but a new resonance labeled  $s_{02}$  is also observed at 690 nm. Unlike  $s_{11}$  which has a nodal line across the centre of the nanocube, the  $s_{02}$  mode is maximum at the centre and each corner of the nanocube (Fig. 4.4e, inset). In the far-field however, the strong scattering resonance at  $s_{11}$  (950 nm) is absent and two new resonances labeled  $j_+$  and  $j_-$  appear at 610 and 750 nm (which is discussed in detail in later sections, but come from mixing  $s_{02}$  and  $l_1$ ), with lineshapes that are not Lorentzian. Similar modes

are also observed in cropped spheres with NPoM geometry [49, 55] where strong mixing is found between  $l_1$  and  $s_{02}$  modes.

### 4.4.1 Symmetry based decomposition of nanocavity modes in NCoMs

The origin of the resonances in near- and far-field can be better understood through group representation theory analysis [151–155]. The symmetry operations of the NCoM structure form the  $C_{4v}$  group, which has five irreducible representations (*irrep*,  $\Gamma$ ). For each  $\Gamma_i$ , a projection operator can be constructed<sup>1</sup>. The application of all projection operators to a function results in basis functions that belong to different  $\Gamma_i$ . More importantly, the obtained basis functions are orthogonal to each other in an inner product sense. Therefore, the optical response from a FDTD solver [151–156] including the surface charge, surface currents, near-, and far-fields of the NCoM can be decomposed according to  $\Gamma_i$ . For a given incident field, the full solution of the surface charge can thus be decomposed into surface charge basis functions (Fig. 4.7a,b) belonging to the first ( $\Gamma_1$ ) and fifth ( $\Gamma_5$ ) irreps. Inspecting the charge contributions from  $\Gamma_{i=1\dots 5}$  shows that  $\Gamma_{2-4}$  do not contribute significantly to the total field in the gap. The surface-charge basis functions act as sources inducing the near- as well as the far-field. When the scattering cross section is evaluated, due to their orthogonality, no interference between  $\Gamma_1$  and  $\Gamma_5$  is observed. This immediately allows an additive decomposition of the scattering cross section, as easily confirmed by comparing the orange curve with the dashed green and grey curves ( $\sigma_s$  due to  $\Gamma_1$  and  $\Gamma_5$  respectively) which shows they are not coupled or interfering. The scattering cross section associated with  $\Gamma_5$  has a prominent resonance around 880nm and weaker resonances at and below 400 nm (Fig. 4.7a) which correspond to higher order  $s_{ij}$  modes. The narrow  $s_{11}$  mode (880 nm) is weak in the region of the  $j_{\pm}$  modes (which are associated with  $\Gamma_1$ , dashed green).

Corresponding features are seen in the near-field charge distributions (Figs. 4.7b):  $\Gamma_1$  contributes to two resonances labelled  $j_{\pm}$  (627, 750 nm), with similar charge distributions maximized at the centre of the bottom cube face. These modes come from the mixing of  $s_{02}$  and  $l_1$ , and give constructive interference in the near-field that leads to a near-field maximum at 665 nm (Fig. 4.6a lower). The amplitude of these  $j_{\pm}$  modes

---

<sup>1</sup>Group theory analysis presented in this chapter are done by Xuezhi Zheng, Department of Electrical Engineering (ESAT-TELEMIC), KU Leuven, Leuven, Belgium



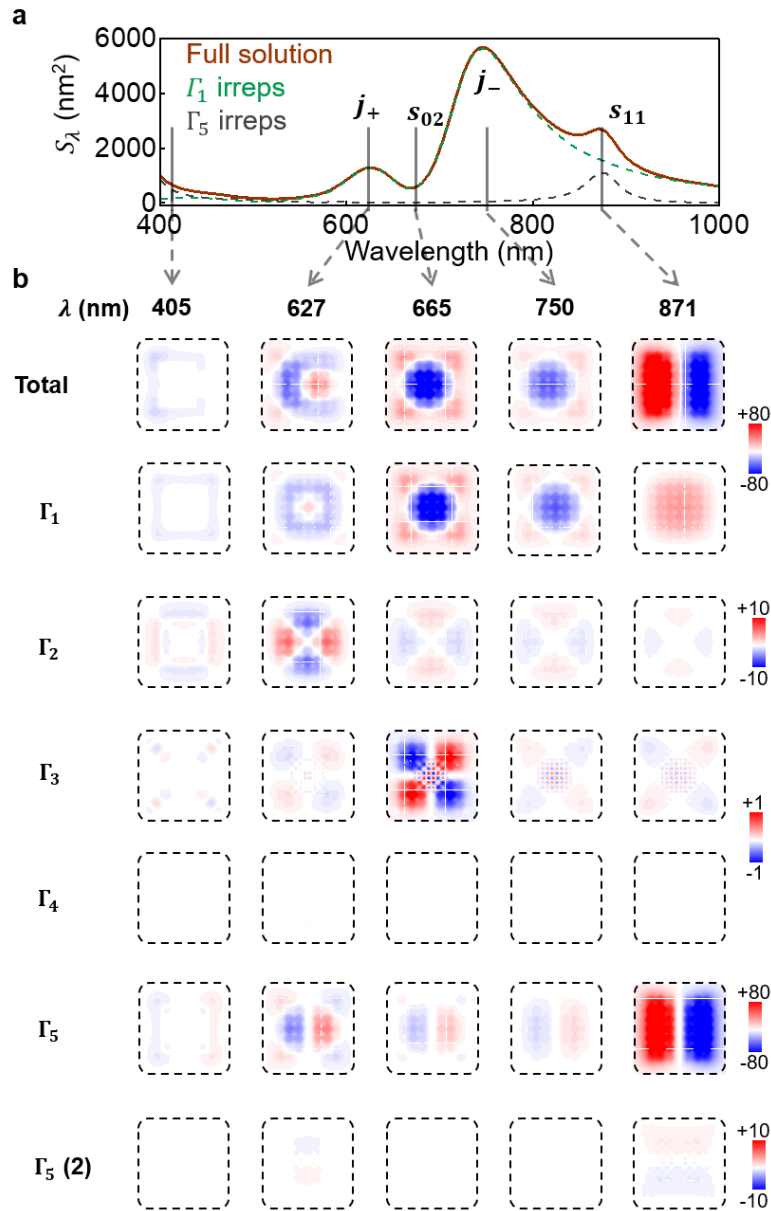


Figure 4.7: **Eigenmode deconvolution of NCoM resonance.** (a) Simulated scattering spectrum for a NCoM with 2 nm gap. Full solution (orange) at  $55^\circ$  incidence, with projections from 1<sup>st</sup> (dashed green) and 5<sup>th</sup> (dashed gray) irreducible representations. (b) Charge distributions and decompositions at different wavelengths from (b) (top row). This is decomposed into the near-field contributions from different eigenmodes ( $\Gamma_1$  to  $\Gamma_5$ ). The  $s_{02}$  mode has a near-field maximum at 665 nm and associated near-field feature is captured in  $\Gamma_1$ , whereas the features of the  $s_{11}$  mode at 871 nm are captured in  $\Gamma_5$ . Note that  $\Gamma_5$  and  $\Gamma_5(2)$  are degenerate modes.

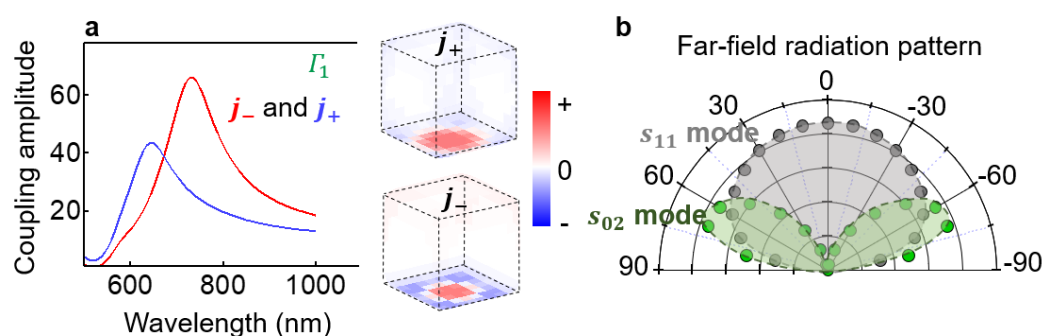


Figure 4.8: **Coupling strengths.** (a) Amplitudes of  $j_{\pm}$  modes and charge distributions to  $\Gamma_1$  component. (b) Angle dependent far-field coupling pattern for  $s_{02}$ ,  $s_{11}$  modes.

shows overlapping spectral components (Fig. 4.8a), however there is a  $\pi$  shift between their emission phases which means they destructively interfere in the far-field. Thus at the wavelength of the central dip between the  $j_{\pm}$  resonances, their near-fields within the gap constructively add while in the far-field they cancel out. This can also be seen from their opposite charge on the top surface of the cube (Fig. 4.8a, right), [157] thus giving their asymmetric line shapes. It is important to note that when  $j_{\pm}$  couple to molecules, it is through their local near-field in the gap whereas far-field radiation of these modes is driven by the oscillating charge on the top surface of the nanocube.

Even though  $s_{11}$  and  $s_{02}$  modes are projections of different  $\Gamma_i$ , their near-fields both have major contributions from  $E_z$  components. Intrigued by this aspect I checked the angle-dependent scattering cross-sections (Figs. 4.8b) and found that  $s_{11}$  modes have maximum coupling efficiency for  $k$  normal to the surface (horizontal dipoles) while for  $s_{02}$  modes coupling is maximized for  $k$  incident at  $60^\circ$  to the film (vertical dipoles). It thus turns out that symmetry breaking from the nanoparticle-on-mirror geometry (compared to a nanoparticle dimer) allows a horizontal input field to partially couple to a vertical quadrupole with strong  $E_z$  [158, 159].

## 4.5 Variation of gap size

To track the formation and evolution of these hybrid  $j_{\pm}$  modes, the spacer thickness ( $d$ ) is tuned by using different aliphatic self-assembled monolayers. Molecular monolayers of 1-octadecanethiol, 1-dodecanethiol and 1-nonanethiol have decreasing chain lengths (18, 12, and 9 carbon atoms respectively) resulting in gaps of 3.5, 2.8 and 2.2 nm (as previously

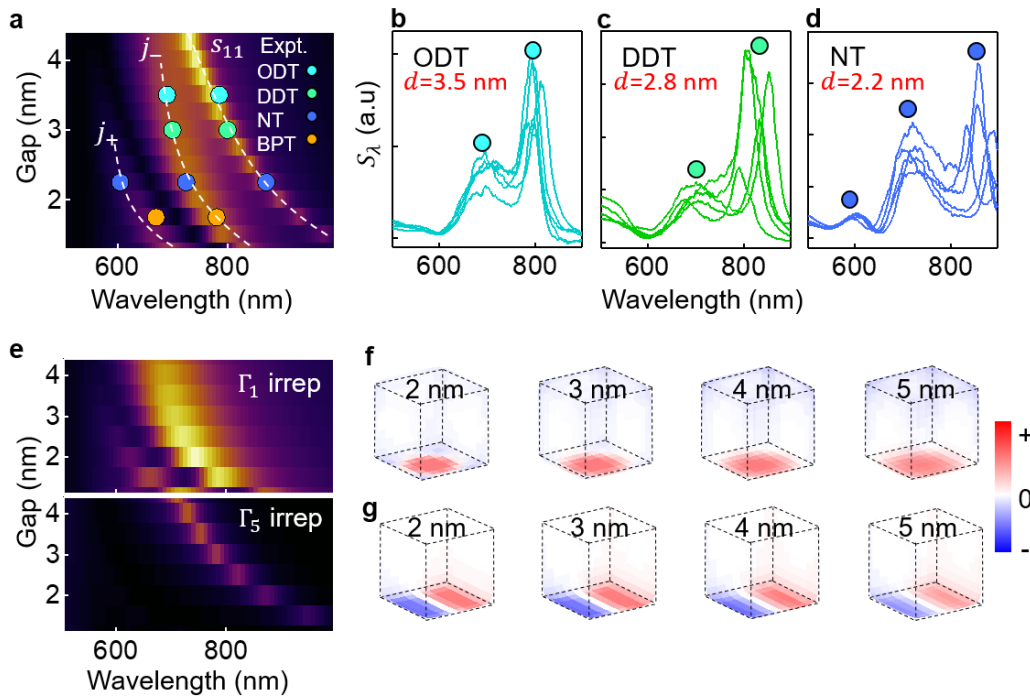


Figure 4.9: **Evolution of nanocavity modes with gap size.** (a) Experimental resonance positions (coloured points) of  $s_{11}$  and  $j_{\pm}$  modes for different molecular spacers in addition to PVP coating (see text, dotted lines are guides to eye). Background colour map shows calculated spectra with gap size. (b-d) Scattering spectra obtained for different molecular spacers of  $d$  (b) 3.5 nm, (c) 2.8 nm, and (d) 2.2 nm thickness. Peak positions are marked by colour-coded dots as in (a). (e) Evolution of scattering cross sections from projections of  $\Gamma_1$  and  $\Gamma_5$  vs gap size. (f,g) Evolution of charge confinement vs gap size ( $d$  as marked) for (f)  $\Gamma_1$  and (g)  $\Gamma_5$ .

determined [160]) including the layer of PVP around the nanocubes. Both experimentally and numerically, the  $s_{11}$  scattered mode is seen to rapidly shift from 800 nm to 900 nm for a small reduction in gap from 3.5 nm to 2.2 nm (Fig. 4.9a-d). In these experiments, BPT molecular spacers have a larger refractive index than aliphatic monolayers so the  $s_{11}$  mode is shifted further into the infrared and cannot be observed in the optical dark-field setup.

This  $s_{11}$  mode scattering strength weakens as the gap decreases (Fig. 4.9a), which makes it hard to couple into this mode at smaller gaps, while limiting the field confinement essential for extreme nano-optics. On the other hand, the  $j_{\pm}$  resonances become prominent at smaller gaps, which correlates with their increasing proximity to the  $l_1$  mode. The coupling of the  $j_{\pm}$  modes intensifies and exhibits a systematic red-shift as the gap size decreases, which is in good agreement with the observed trend in scattering cross sections shown in Fig. 4.9a-d. The surface charge distribution also varies with the gap size (Fig.

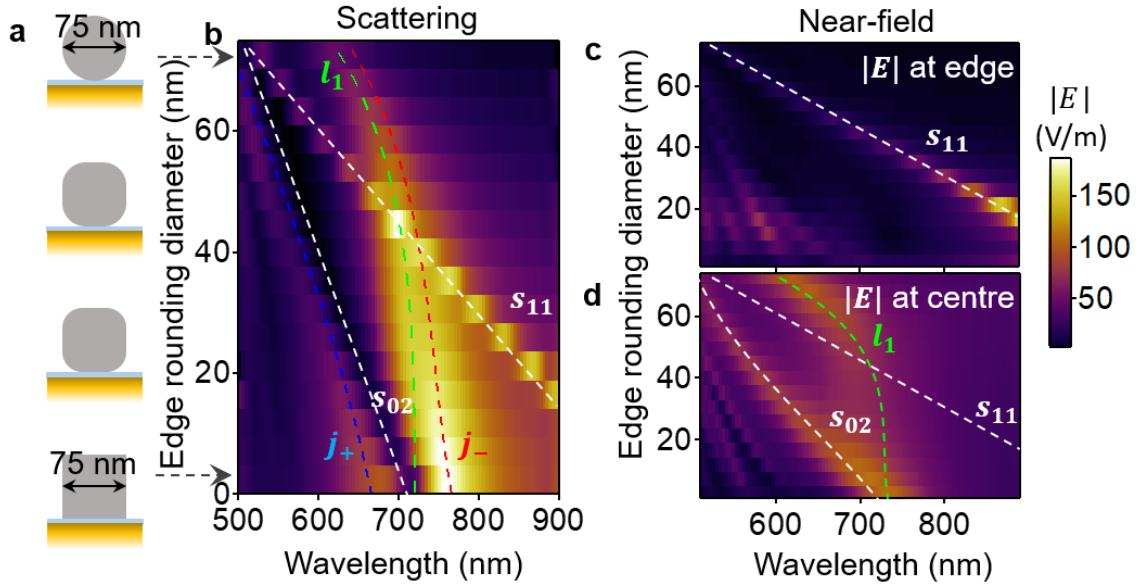


Figure 4.10: **Evolution from nanocube to nanosphere with 3 nm gap.** (a) Schematic of smoothly transforming a nanocube of edge length 75 nm into a nanosphere of 75 nm diameter by tuning the edge rounding parameter. (b) Simulated 3D FDTD scattering spectra obtained for nanostructures defined in (a). Resonance wavelengths of modes vary due to the change in volume ( $l_1$ , green line) and edge length ( $s_{ij}$ , white lines) of nanostructure. Calculated resonance position of  $j_+$  and  $j_-$  due to the mixing between  $l_1$  and  $s_{02}$  modes shown as red/blue dashed lines. (c,d) Near-field intensities vs  $\lambda$ , (c) at edge, and (d) at centre of lower gap facet, resonant modes colour coded as (b).

4.9f). As the gap size reduces, the bottom surface charges concentrate more to the centre, attributed to the increased attraction exerted by the image charges in the underlying mirror.

## 4.6 Tuning the shape of the nanocavity

Clear identification of the  $s$ ,  $l$  and  $j$  modes is obtained from simulations in which NCoMs are gradually transformed into NPoMs by progressively rounding the edges of the nanocube (Fig. 4.10a). Increasing the nanocube edge roundness linearly blue-shifts the  $s_{11}$  NCoM mode as the facet diameter decreases (Fig. 4.10b), becoming no longer the ground state for the NPoM after 60% rounding. Discrimination of the modes by symmetry is achieved by monitoring the near-field spectra at the edge ( $s_{11}$ ) and centre ( $s_{02}, l_1$ ) of the nanostructure (Fig. 4.10c,d). The  $l_1$  mode of an equivalent sphere NPoM which is given the same total volume as this progressively rounded cube (Fig. 4.10d, dashed green) almost exactly tracks the resonance observed in the near-field at the facet centre. The predicted position of  $j_{\pm}$

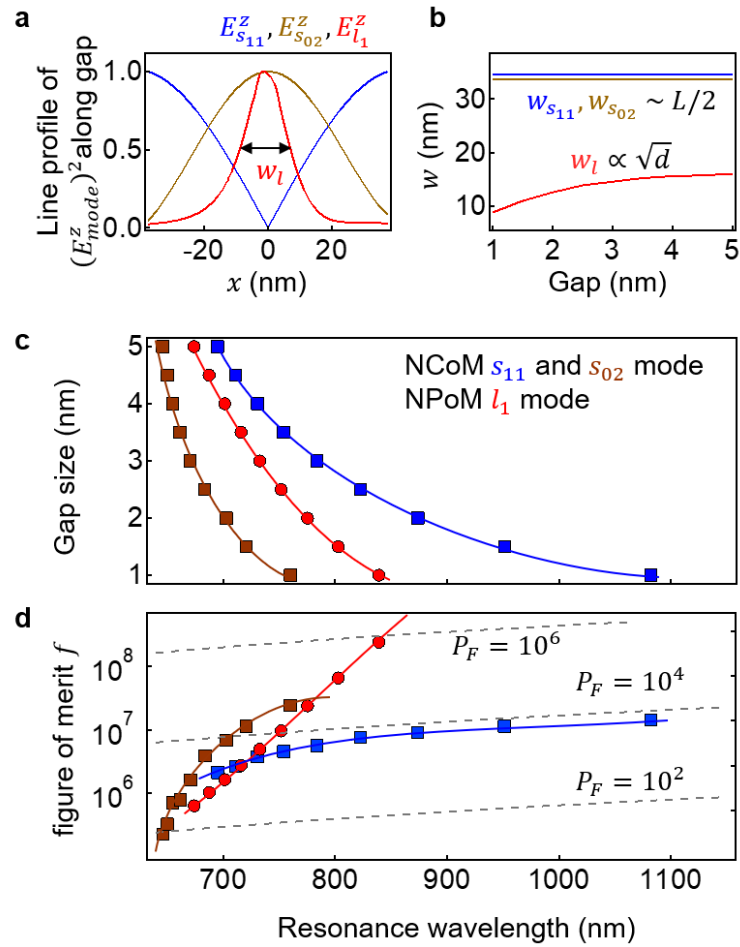


Figure 4.11: **Comparing molecular-coupling figure of merit for cube NCoM and sphere NPoM of same volumes.** (a) Line profile of  $|E|$  field in the middle of the gap. (b) Field confinement length ( $w$ ) in the lateral ( $x$ ) direction. (c) Resonance frequency of NCoM modes (square dots) and NPoM mode (circular dots) with gap size. (d) Figure of merit for modes (colour-coded as in a), dotted grey lines indicate Purcell factors  $P_F$ .

modes (red/blue dotted lines, Fig. 4.10b) is calculated from the frequencies of  $l_1$  and  $s_{02}$  from near-field (Fig. 4.10d) with a coupling strength of 250 meV obtained for this scenario.

## 4.7 Figure of merit

The molecular-coupling efficiencies of NPoM and NCoM systems can now be compared, being careful to use the same particle volume for each (Fig. 4.11). I first note that for small gaps, the  $s_{11}$  mode in cubes is always at much longer wavelengths than the  $s_{02}$  modes making it awkward to utilize in coupling with electronic resonances in the visible

and near-IR (high-oscillator-strength electronic transitions of molecules or semiconductors are hard to tune into the IR as they come from larger less-localized electronic states). The  $s_{02}$  modes support near-field enhancements that exceed the  $s_{11}$  mode for gaps  $d < 2.2$  nm, and slightly exceed those found for spherical NPoMs. Although for larger gaps ( $d > 2.2$  nm) the cube NCoM produces higher field enhancements from the  $s_{11}$  mode, this is always at longer wavelengths (beyond 720 nm) and for the same spectral resonance position, the  $s_{02}$  is always preferred. Of most importance, however is the mode volume as well as the field enhancement. The effective mode volume for  $s_{11}$  and  $s_{02}$  from the cube NCoM is considerably larger than the  $l_1$  mode of sphere NPoMs (Fig. 4.11a,b). I define a suitable figure of merit comparing these modes that is proportional to the Rabi coupling strength,  $\Omega_R \propto f$ , and thus involves both near-field enhancement and mode volume as,

$$f = (E^2/E_0^2)/(A_{\text{eff}}/A_\lambda) \quad (4.4)$$

where the effective lateral mode area  $A_{\text{eff}}$  for the  $l_1$  mode is  $A_{\text{eff}} = \pi R d$  and for the  $s_{11}$ ,  $s_{02}$  modes is  $\sim L^2/4$  where  $R$  is the radius of nanosphere and  $L$  is the edge length of the nanocube. The normalization is to  $A_\lambda = (\lambda/n)^2$  where  $\lambda/n$  is the wavelength of the resonance in the gap medium. For gaps  $d > 4$  nm,  $s_{11}$  has larger  $f$  values than the other two modes with Purcell factor ( $\propto Q/V$ ) up to  $7 \times 10^3$ , however as the gap becomes smaller, the coupling  $f$  saturates for cube modes  $s_{11}$  and  $s_{02}$  (Fig. 4.11d). In contrast, the  $l_1$  mode dominates for gaps  $< 2.2$  nm with large  $f$  values and Purcell factors exceeding  $10^6$ . For this reason, the desirable extreme nano-optics regime of coupling to single emitters will always favour the sphere NPoM with vertical dipole orientation, rather than the  $s_{11}$  mode in cubes. I note that some degree of faceting is always inevitable, hence in practice mixed  $s_{02}$ - $l_1$  modes will be obtained. However, these conclusions hold in practical experiments where neither extreme geometry is feasible, since nanospheres are faceted and nanocubes have rounded edges.

## 4.8 Conclusion

I have experimentally and theoretically compared the effect of nanoparticle shape for the prototypical coupling between plasmonic components. For gaps of a few nanometres, I find that optical coupling to emitters is favoured for modes with plasmonic fields perpendicular

to the gap, although input coupling is easier for the geometry where the plasmonic fields are parallel to the gap. This analysis is further used to design optimal experiments and explore the extreme nano-optics.







## 5 Single-molecule Surface Enhanced Raman Scattering

Enhancing weak Raman signals from molecules in metal nanogaps is undoubtedly one of the biggest achievements of plasmonics. In this chapter, I discuss how this local enhancement can be used for detecting single-molecule Raman signatures. I consider two different approaches to pin down an unambiguous proof for single-molecule sensitivity in the nanoparticle-on-mirror (NPoM) geometry. The first is a chemical  $g_{ch}^{(2)}$  technique, where two different molecules with well-distinguished Raman spectra are mixed in the nanogap and it is shown that for mixtures at low concentrations, signals arise from one or the other, but not from both the molecules. Further I discuss multi-principal component analysis for robust statistical analysis for  $> 1000$  NPoM and extract single-molecule events. The second approach is time-resolved surface enhanced Raman, where spectral diffusion of Raman signals arises from the bending and flexing of single-molecules.

## 5.1 Detecting single-molecules

Detection of single-molecules has been a central question of research across all molecular science disciplines [161, 162]. Typical photon absorption at room temperature from ground state to first singlet-excited state (the largest optical cross-section) [163] is  $5 \times 10^{-2} \text{nm}^2$  where a high-numerical-aperture microscope objective focuses light to an area of  $10^5 \text{nm}^2$ . As a result, absorption of at best one in  $10^6$  incident photons by the molecule of interest will occur and weak differential signal with high background noise makes the detection extremely difficult. Hence, traditional absorption schemes are limited to cryogenic temperatures, along with the right guest-host system where absorption cross-sections are boosted by  $10^6$ . Consequently, fluorescence detection (photons emitted from the singlet-excited state) gained importance due to its zero-background noise and easy experimental detection schemes.

Nevertheless, reasons for not using fluorescence methods for probing single-molecules are plenty. (i) Many molecules are inherently not fluorescent or have very low quantum yield ( $10^{-3}$ ), (ii) fluorescent labelling might not work for probing small molecules, and (iii) labelling might change the properties of the probe system altogether. Most importantly, both absorption and fluorescence methods provide information only about the electronic states of the molecules, which might not be of great use in various studies including the detailed structural and dynamic information of the molecule such as enzymatic studies dealing with vibrational bond-breaking and forming.

To this end, Raman scattering is a useful method to probe ground state vibrations of the molecule, and its detection schemes are not much different from the fluorescence methods. However, cross-section for Raman is  $10^{-15}$  times weaker than the absorption cross-section [164, 165] making detection difficult. Here, I discuss how Raman scattering can be boosted in plasmonic cavities and introduce statistical tools to probe single-molecules.

## 5.2 Rayleigh and Raman scattering

Curiosity to explain the colour of the sky led to the formulation of classical theory of light scattering by Lord Rayleigh in 1871. In Rayleigh scattering, incident light is scattered by molecules (or particles much smaller than the wavelength of incident light) with the same

photon energy. But C. V. Raman was not satisfied with Rayleigh's explanation on the colour of sea, especially after observing the intense blue of Mediterranean Sea.

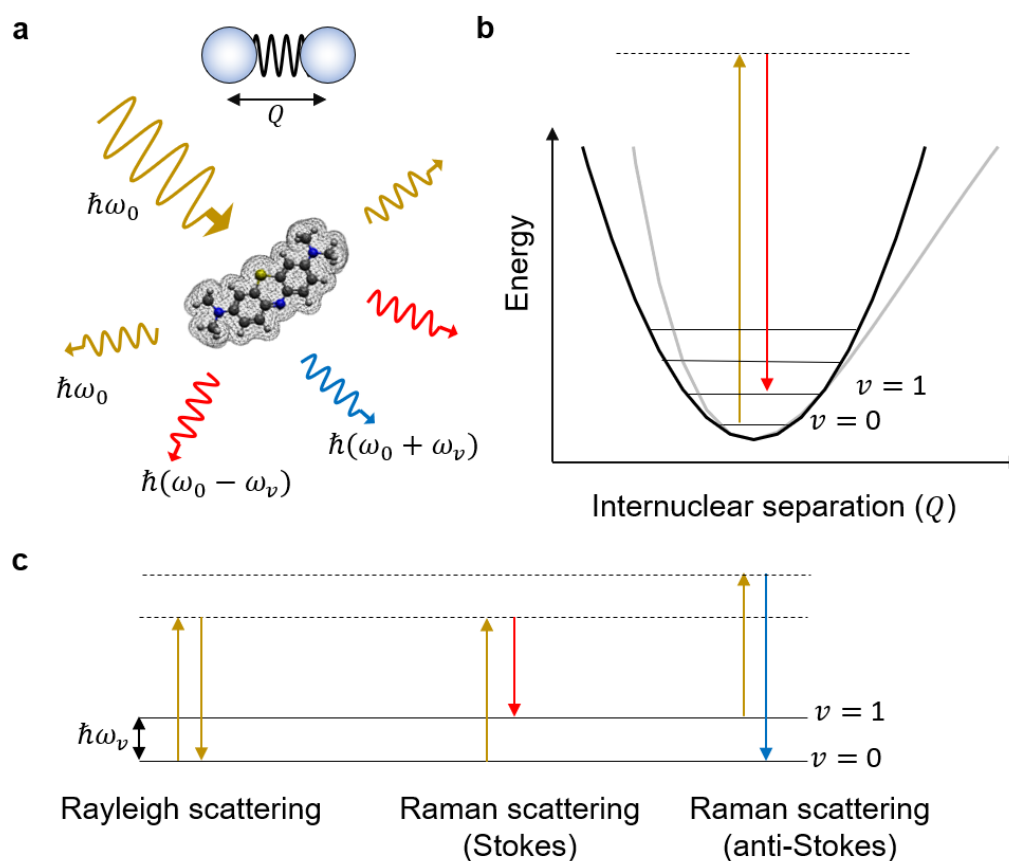


Figure 5.1: **Raman scattering by molecule.** (a) Diagrammatic representation of light scattering from a vibrating molecule, modelled as masses connected by a spring. (b) A harmonic potential (solid black line) approximates the energy landscape of the ground electronic level (grey line). (c) Schematic of nonresonant Stokes and anti-Stokes scattering between two vibrational states of the molecule mediated by a virtual state.

This led to the study of scattering of light by liquids, which resulted in the experimental discovery of scattering that changes the frequency of incident light. This new type of secondary radiation observed in 1928 (by C. V. Raman and K. S. Krishnan) termed Raman scattering opened the door for new realms of research [166, 167].

The origin of scattered radiation is the oscillating electric dipole induced in a molecule by the electromagnetic fields of the incident light waves<sup>1</sup>. The relation between induced electric dipole moment  $\vec{P}$  and  $\vec{E}$  is given by,<sup>2</sup>

$$\vec{P} = \tilde{\alpha} \cdot \vec{E} \quad (5.1)$$

Here,  $\tilde{\alpha}$  is the polarizability of the molecule and is a second order tensor. In general  $\vec{P}$  has frequency components associated to Rayleigh scattering ( $P^{Ray}$ ) with frequency  $\omega_i$  and Raman scattering ( $P^{\omega_i \pm \omega_v}$ ) at  $\omega_i \pm \omega_v$  ( $\omega_v$  is the molecular vibration frequency) ( $P = P^{Ray} + P^{\omega_i + \omega_v} + P^{\omega_i - \omega_v}$ ). The time averaged intensity of Raman or Rayleigh scattering is given as

$$I = k' \omega_s^4 P^2 \sin^2 \theta; \quad k' = 1/(32\pi^2 \epsilon_0 c_0^3) \quad (5.2)$$

With appropriate polarizability values at scattering frequency  $\omega_s$ , along the direction making an angle  $\theta$  with the dipole axis, the scattered radiation is proportional to the irradiance of the incident radiation. Here  $\tilde{\alpha}$  will in general, be a function of the nuclear coordinates and hence of the molecular vibrational frequencies  $\omega_v$ . The variation of  $\tilde{\alpha}$  with vibrations of the molecule can be expressed by expanding each component  $\tilde{\alpha}_{xy}$  of the polarizability tensor in a Taylor series with respect to the normal coordinates of vibration, as follows.

$$\tilde{\alpha}_{xy} = (\tilde{\alpha}_{xy})_0 + \sum_k \left( \frac{\partial \tilde{\alpha}_{xy}}{\partial Q_k} \right)_0 Q_k + \frac{1}{2} \sum_{k,l} \left( \frac{\partial^2 \tilde{\alpha}_{xy}}{\partial Q_k \partial Q_l} \right)_0 Q_k Q_l \dots \quad (5.3)$$

where  $Q_k, Q_l \dots$  are the normal vibration coordinates at molecular vibration frequencies  $\omega_k, \omega_l$  and the sum is over all the normal coordinates. The subscript '0' indicates that these values are considered at an equilibrium configuration. In an electrical harmonic approximation<sup>3</sup> generalized for all tensor components, we write,

---

<sup>1</sup>Note that the contribution from magnetic dipole and higher-order electric oscillations are typically several orders of magnitude smaller compared to oscillating electric dipole oscillations. But these weak interactions are enhanced in plasmonic nanocavities in which incident wavelength is compressed to the dimensions of the molecule.

<sup>2</sup>Note that I have deliberately ignored higher-order induced dipole moments which are non-linear. i.e.  $\vec{P} = \vec{P}^{(1)} + \vec{P}^{(2)} + \vec{P}^{(3)} + \dots = \tilde{\alpha} \cdot \vec{E} + \left(\frac{1}{2}\right) \tilde{\beta} : \vec{E} \vec{E} + \left(\frac{1}{6}\right) \tilde{\gamma} : \vec{E} \vec{E} \vec{E} + \dots$  where  $\beta$  and  $\gamma$  are hyperpolarizability and second order hyperpolarizability with third and fourth-rank tensor.

<sup>3</sup>In a harmonic oscillator approximation, the restoring force is proportional to the first power of the displacement. Similarly, variation in the polarizability due to vibration is proportional to the first power of  $Q_k$ .

$$\tilde{\alpha}_k = \tilde{\alpha}_0 + \tilde{\alpha}'_k Q_k; \quad \tilde{\alpha}'_k = \left( \frac{\partial \alpha}{\partial Q_k} \right)_0 \quad (5.4)$$

In time dependent simple harmonic motion of  $Q_k = Q_{k0} \cos(\omega_k t + \delta_k)$  with normal coordinate amplitude  $Q_{k0}$  and phase factor  $\delta_k$ , the time dependent polarizability tensor resulting from  $k^{\text{th}}$  molecular vibration is  $\tilde{\alpha}_k = \tilde{\alpha}_0 + \tilde{\alpha}'_k Q_k \cos(\omega_k t + \delta_k)$ . Along with  $E = E_0 \cos \omega_0 t$ , the induced dipole moment is,

$$P = \tilde{\alpha}_0 E_0 \cos \omega_0 t + \tilde{\alpha}'_k E_0 Q_{k0} \cos(\omega_k t + \delta) \cos \omega_0 t \quad (5.5)$$

Reformulating with simple trigonometric identity,

$$P = \tilde{\alpha}_0 E_0 \cos \omega_0 t + \frac{1}{2} \tilde{\alpha}'_k Q_{k0} E_0 \cos(\omega_0 \pm \omega_k t \pm \delta_k) t \quad (5.6)$$

Here, the first term is associated to Rayleigh scattering and latter term to Raman scattering with Raman polarizability  $\alpha_k = \frac{1}{2} \tilde{\alpha}'_k Q_k$ . Note that all the molecules exhibit Rayleigh scattering as all of them are polarizable ( $\tilde{\alpha}_0$  is never zero). However, for the vibrational modes to be Raman active the change in molecular polarizability  $\alpha'_k \neq 0$ . Thus, the condition for Raman activity is that, for at least one component of the polarizability tensor, a plot of that component against the normal coordinate must have a non-zero gradient at the equilibrium position. Interestingly, homo-nuclear diatomic molecules which are not observable in infrared-vibrational spectroscopy will be accessible in Raman scattering. The selection rules remain unaffected even if the mechanical anharmonicity (Morse curve from Fig. 5.1) is considered, but anharmonicity can lead to the observation of overtones. Despite having such a specific fingerprint information about the molecular structure, Raman spectroscopy was limited with low scattering cross-sections ( $\sim 10^{-29} \text{cm}^2$ ). Enhancement by a factor  $< 10^3$  in Raman signal can be obtained by choosing the excitation frequency overlapping with an electronic resonance (resonance Raman (RR)). Unfortunately, this resonant excitation can lead to undesirable photochemical effects. An imperative need to enhance Raman intensities inspired the development of plasmonic architectures which avoid the issue of weak signals via surface enhanced Raman scattering (SERS).

### 5.3 Surface enhanced Raman scattering

Surface-enhanced Raman scattering (SERS) amplifies Raman scattering of the molecules by several orders of magnitude [165]. This phenomenon was first observed by Fleischmann et al. in 1974 for pyridine molecules adsorbed on electrochemically roughened silver electrode [168, 169]. It is almost universally accepted that the enhancement is largely due to the amplification of the local electric fields owing to the excitation of surface-plasmon resonances, to which molecules interact in close proximity to a nanometallic surface. This enhancement is quantified by the enhancement of the local electric field  $E$  and the overall intensity of Raman scattered light as,

$$I_{\text{SERS}} \propto \alpha_R^2 |g(\omega_0)|^2 |g(\omega_0 + \omega_v)|^2 I_0 \quad (5.7)$$

Here,  $\alpha_R$  is the Raman polarizability for the bond vibrating with frequency  $v$ . The near-field enhancement at excitation frequency ( $\omega_0$ ) and the scattered light frequency ( $\omega_0 + \omega_v$ ) are  $g(\omega) = E^2/E_0^2$  estimated at those wavelengths<sup>4</sup>. Here  $E_0^2$  is the intensity of the input electric field. This simple model of SERS as a two-step process is not strictly accurate. Instead, this needs to be solved as a coupled electromagnetic problem of radiating dipoles for the case of a plasmonic nanostructure coupled with incident electric fields. For plasmonic systems with plasmon resonance line-width larger than the energy shift of the Raman scattering,  $g(\omega_0) \approx g(\omega_0 + \omega_v)$ , thus scaling SERS intensity to the fourth power of electromagnetic enhancement,  $\text{SERS} \propto E^4$ . This approximation is indeed true for plasmonic cavities with  $Q < 5$  but does not hold for plasmonic dimers or NPoM cavities where  $Q > 10$  and when multiple cavity modes participate in Raman scattering.

#### 5.3.1 SERS: Electromagnetic and chemical enhancements

For a nanoparticle with  $2R=100$  nm with 40 nm facet placed above the metal film with a gap spacing of 1 nm, the field enhancement at 785 nm is  $E/E_0 > 300$  (Fig. 5.2a). The confined optical fields are strongly wavelength-dependent (Fig. 5.2b) and the pump wavelength ( $\lambda_0$ ) and Raman scattered light are enhanced at different rates. An appropriate choice of pump laser can change the SERS intensity by 10-100 times (Fig. 5.2c). For a 100 nm nanoparticle

<sup>4</sup>The estimation of enhancement in local electric fields needs to be via far-field excitation. As plasmonic cavities support both dark and bright modes, the enhancement in near-field due to dark-modes might not enhance Raman scattering directly. But bright and dark modes intermix in appropriate symmetry conditions (as discussed in Ch. 4) resulting in an enhancement of Raman scattering.

in NPoM geometry, excitation with 785 nm provides the maximum enhancement, whereas for 40–60 nm nanoparticles, 633 nm pump wavelengths yield better results.

As we saw, the position of a molecule in the gap is crucial in determining the enhancement of its vibration. Under these optimum conditions the SERS enhancement can be as large as  $10^{10}$ . This strong optical field confinement in the gap is generally referred to as a SERS 'hotspot'. However, enhancement ( $E/E_0$ ) is not non-uniformly distributed and confined in spatially narrow regions  $<100\text{ nm}^2$ . For uniformly deposited molecules on the metal film, only a small set of molecules in this 'hotspot' are enhanced and observed in SERS spectra and typically the number of molecules observed in the gap for this NPoM geometry is 100-200. If the molecules are uniformly coated on the nanoparticle, more than 80% of the SERS signal will be contributed by  $<1\%$  of the molecules. Such skewed intensity variation is equivalent to a Pareto distribution [170, 171], which makes single-molecule SERS studies and analysis nontrivial.

There are also other effects that alter the wavelength-dependent SERS enhancement. Those are broadly classified as chemical effects that can boost or suppress the SERS signal by factors  $<1000$ . Chemical enhancements which are systematically studied are (i) electronic resonance Raman, (ii) charge transfer from metal to electronic state of the molecule, (iii) presence of static charge around the molecule, (iv) change in energy levels of molecules due to chemical bonding with the metal, and (v) hot-electron transfer from metal to molecule changing the redox state of the molecule. All these effects have profound effects on SERS intensity fluctuations in time, spectral shifts or the formation of new Raman modes. Among these, a boost in SERS by  $\times 1000$  is evident in electronic resonance Raman, in which  $\lambda_0$  drives the electronic eigen-state of the molecule (termed SERRS). An MB encapsulated in the CB[7] and assembled in NPoM geometry shows this effect of electronic resonance. SERS obtained from pumping with 633 nm resulted in signals  $>50$  times stronger than non-resonant pumping at 785 nm. Moreover, relative intensities of SERS peaks are different compared to off-resonant SERS. Given these different enhancements in Raman signals, can this technique be used to probe single-molecules? If so, how is it possible to quantify the number of molecules contributing to SERS?

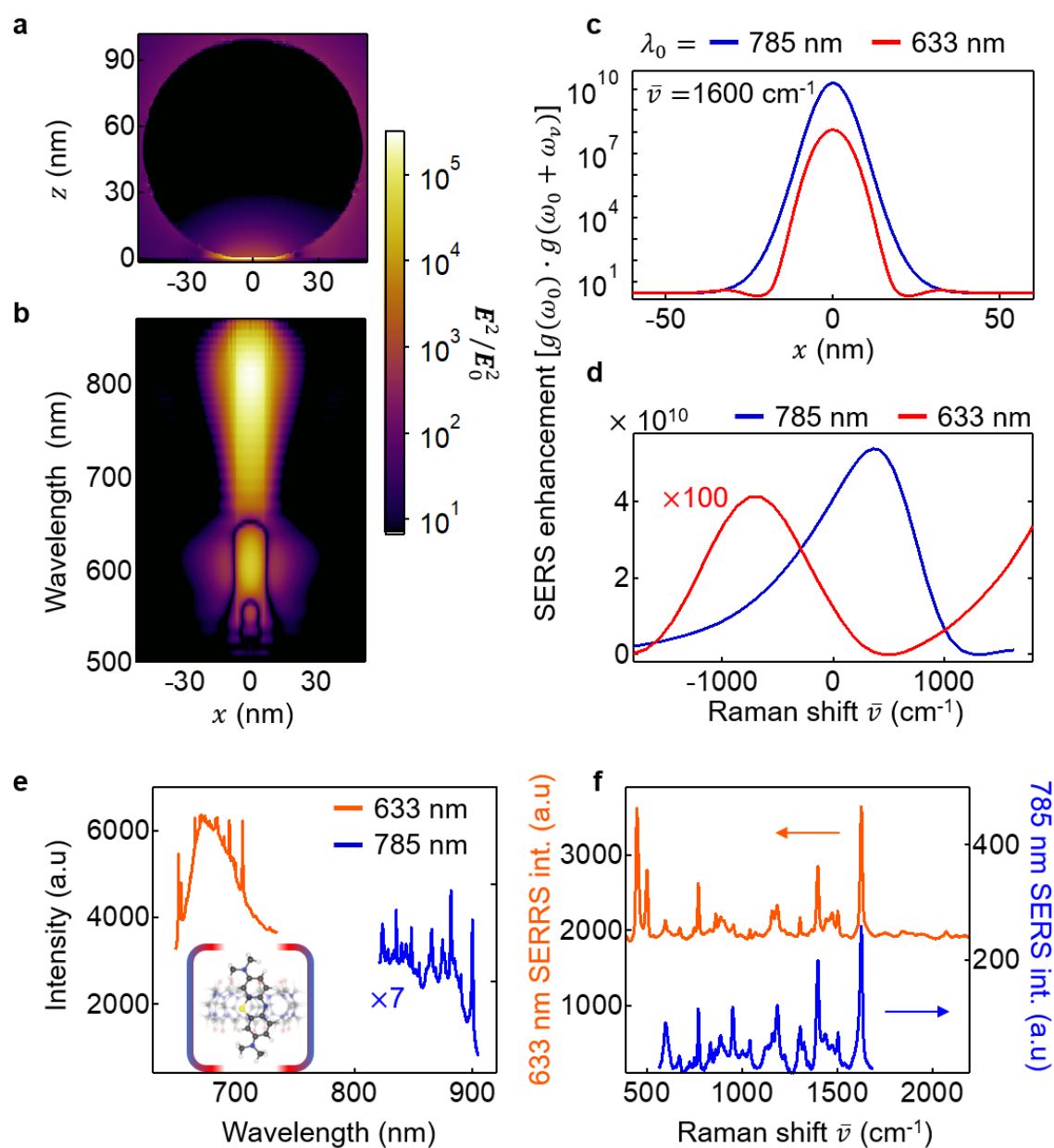


Figure 5.2: **SERS in nanoparticle-on-mirror cavity.** (a) Enhancement of optical field intensity in NPoM for  $2R=100$  nm nanoparticle with 40 nm facet and 1 nm spacer at 785 nm. (b) Wavelength dependent optical field intensity along the middle of gap in  $x$  direction. SERS enhancement for excitation wavelength of (c) 785 nm and 633 nm along the gap and (d) for different Raman modes characterized by Raman shift. (e) SERS signal obtained from CB[7]-MB complex in NPoM geometry with excitation overlapping with electronic resonance (633 nm) and off resonance excitation (785 nm). (f) SERS spectra are replotted by removing the background from (e).



## 5.4 Single-molecule SERS

'How to ensure that the observed SERS spectrum is from just one-molecule?' has been a challenge for decades even after the early claims of single-molecule SERS detection. This uncertainty is because of the experimental strategies used to probe the molecules. The basic assumption of this approach is to work at a low analyte-concentration (pico/femto molar) such that there cannot be more than one molecule per nanoparticle or a cluster of nanoparticles. Another assumption is that the fluctuation in the intensity from nanoparticle to nanoparticle or in time, comes from the variation in the number of molecules or the spatial position of a molecule in the gap. This is problematic mainly due to two reasons: (i) There is no way to ensure that molecules are not bunched and attached to nanoparticles as a cluster. (ii) Experiments with different concentration of molecules per nanoparticle have shown that the intensity distribution is dominated by the variation in position/orientation of a molecule in the 'hotspot' and thus smears the variation in  $n$ . Hence, Poisson statistics ( $P(n) = e^{-\lambda}\lambda^n/n!$ ) is not an appropriate approach towards intensity fluctuations to quantify  $n$ .

To overcome this ambiguity, Etchegoin et al. proposed bi-analyte SERS and principal component analysis (PCA) to quantify single-molecule events [170, 172, 173]. The bi-analyte method is the concept of using two different molecules with well-distinguished Raman spectra, to show that mixtures at low concentration result in signals arising from one or the other, but not from both the molecules. The tool to analyze this data is via PCA. Unlike a Poisson statistical approach, this tool does not completely rely on the signal intensity, rather, it deals with the occurrence of SERS signatures in four different probabilistic events.

### 5.4.1 Principal component analysis

Principal component analysis is a statistical technique that reduces the dimension of the data set, without compromising on the information. Once the linear transformation is performed on the data, it transforms the data into a new co-ordinate system, where the new set of variables (principal components) are linear functions of the original variables. For the bi-analyte case, new variables will be the principal components corresponding to SERS signals from the two molecules. One should be careful choosing molecules to have minimal Raman spectral overlap, while both the molecules of interest will have an equal

probability of being present in the gap. The steps associated with PCA analysis are the following.

**Step 1:** The first step is to convert the spectral data into the form of a rectangular matrix. I consider a simple scenario here for ease of calculations, where only two Raman bands (one for each analyte) are associated with a single data set. The matrix  $M$  is represented as,  $M = (y \times x)$ , where  $y$  is the spectrum number from different NPoMs and  $x$  is the wavenumber in the Raman spectrum; each matrix component represents the intensity at that wavenumber.

$$M = \begin{bmatrix} I_{N1}^{\nu_1} & I_{N1}^{\nu_2} & \cdots & I_{N1} \\ I_{N2}^{\nu_1} & I_{N2}^{\nu_2} & \cdots & I_{N2} \\ \vdots & \vdots & \vdots & \vdots \\ I_{Ny}^{\nu_1} & \cdots & \cdots & I_{Ny} \end{bmatrix}$$

**Step 2:** The second step involves mean subtraction for the centering of the matrix. To find the basis which reduces the mean square error while approximating the data, it is crucial to have a mean of zero. So, I first calculate the mean of each row and subtract it from each row element, after which the new matrix looks like,

$$\hat{M} = (\hat{I}_{N_i}^{v_j}) \quad (5.8)$$

where,

$$\hat{I}_{N_i}^{v_j} = I_{N_i}^{v_j} - I_{N_i}^-; \quad I_{N_i}^- = \frac{1}{N} \sum_j I_{N_i}^{v_j} \quad (5.9)$$

**Step 3:** This step calculates the covariance matrix  $V$ , for  $N$  number of column vectors for the new matrix as,

$$V = \left( cov \left( \hat{I}_{N_i}^{v_k}, \hat{I}_{N_i}^{v_j} \right) \right) \quad (5.10)$$

$\left( cov \left( \hat{I}_{N_i}^{v_k}, \hat{I}_{N_i}^{v_j} \right) \right)$  is the covariance of the intensity columns at  $v_j$  and  $v_k$ . This is calculated from the unbiased estimator for the covariance. The covariance matrix is a square matrix of size  $N \times N$  and for better statistical accuracy, one should have a large number of spectra ( $T$ ).

**Step 4:** From the variance matrix, I now calculate the principal components of the data.

The first task is to obtain  $N$  number of eigenvalues and corresponding eigenvectors from  $V$ . Due to the real and symmetric nature of covariance matrix, all the eigenvalues will be positive and real. The most important components are the eigenvectors corresponding to the largest variances (largest eigenvalues), termed 'principal components' of the entire data matrix. In this bi-analyte scenario with just two analytes, there will be two principal components  $f_1^{vj}$ ,  $f_2^{vj}$  ( $j = 1..N$ ) corresponding to the two peaks and each spectrum can be expressed as a linear combination of  $f_1^{vj}$  and  $f_2^{vj}$ .

**Step 5:** The next task is to obtain the two coefficients which depict the linear combination of the principal eigenvectors, to represent a particular spectrum. The table of coefficients can be calculated as,

$$C = \begin{bmatrix} \alpha_1 & \beta_1 \\ \alpha_2 & \beta_2 \\ \vdots & \vdots \\ \alpha_N & \beta_N \end{bmatrix} = \hat{M} \begin{bmatrix} f_1^{v1} & f_2^{v1} \\ f_1^{v2} & f_2^{v2} \\ \vdots & \vdots \\ f_1^{vN} & f_2^{vN} \end{bmatrix}$$

All the parameters required to reconstruct the spectrum are now obtained and the spectral data can now be written as,

$$I_{Ni}^{vj} = \alpha_i f_1^{vj} + \beta_i f_2^{vj} + I_{Ni} \quad (5.11)$$

**Step 6:** To correlate this analysis to the real bi-analyte single-molecule SERS, the  $C$  matrix in the coefficient space needs to be plotted. This gives the distribution of SERS signals from the two molecules of interest. In the plot for a bi-analyte molecular pair, events along the axes in coefficient space are the pure analyte signals and the events between the two axes are the mixed signals. For spectroscopic interpretation, we need two eigenvectors representing the actual SERS spectra and the relative intensities of the two eigenvectors. Moreover, the coefficient matrix  $C$  should have only positive coefficients. To achieve these conditions, multiple linear transformations are performed subsequently, yielding a new set of coefficients and transformed eigenvectors  $g_1^{vj}$  and  $g_2^{vj}$ . At this stage, (1) two principal components are directly related to the Raman signatures from two analytes and (2) the transformed coefficients directly provide the average number of each analyte producing the SERS signal.

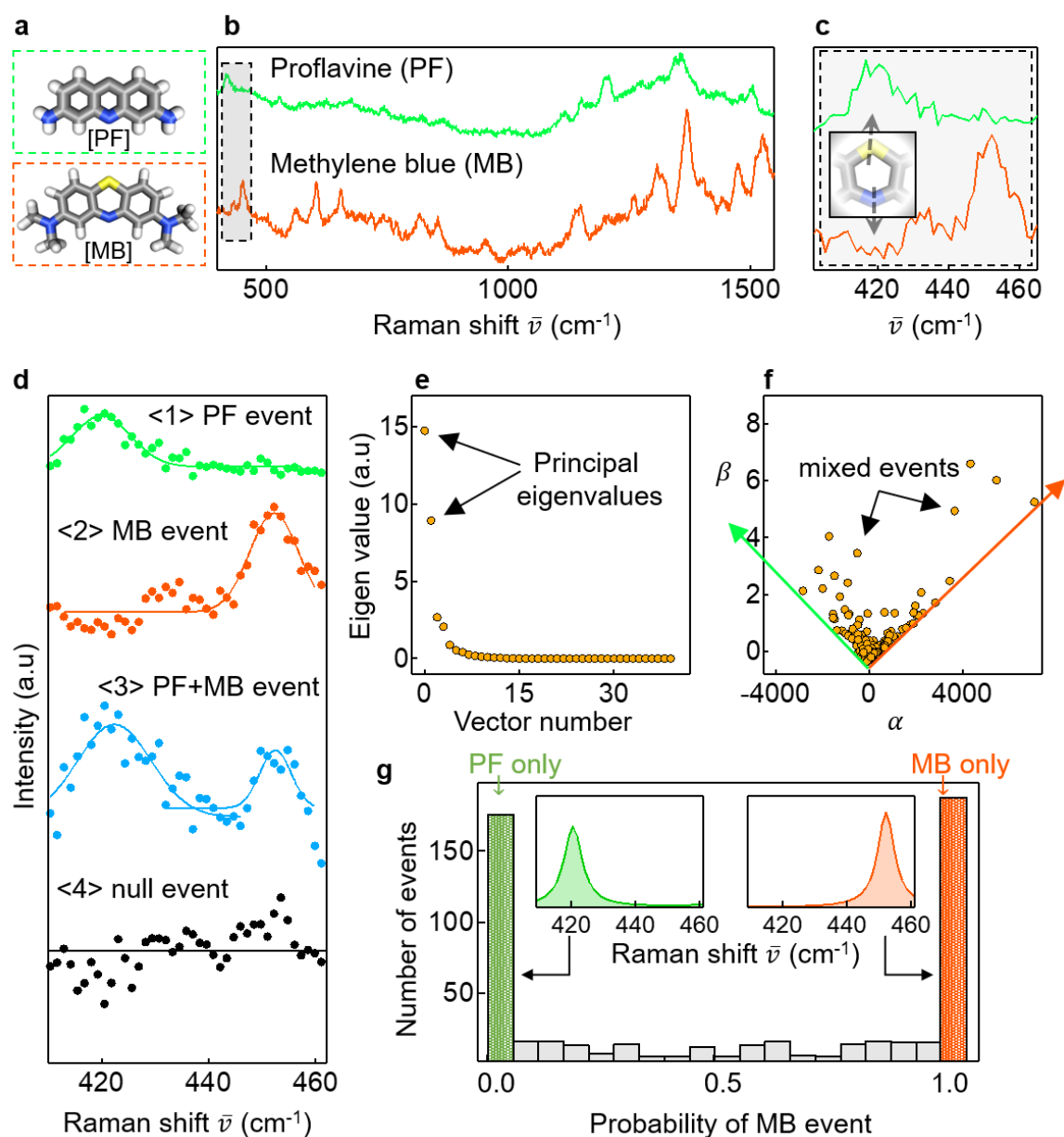


Figure 5.3: **Single-molecule SERS in NPoM.** (a) Chemical structure of methylene blue (MB) and proflavine (PF) used in bi-analyte SERS. (b) SERS spectra from MB and PF molecules collected in NPoM geometry with an integration time of 2s and with an excitation at 785 nm. (c) Selected wavenumbers in which MB and PF show distinct Raman peaks corresponding to central ring breathing mode, shown in inset. (d) Four possible bi-analyte SERS events. (e) SERS for more than 500 nanoparticles from NPoM geometry at the concentration of 1:100 (dye:CB) ratio, which gives  $\bar{n} = 0.2$  dye molecules per nanoparticle. This data was processed with rigorous modified principal component analysis (MPCA), to obtain covariance matrix and extract eigenvalues shown. (f) The coefficient matrix denotes the distribution of the dye signals which are distinguished from each other along the two orthogonal axis indicated through orange and green arrows. (g) Single-molecule probability histogram derived from MPCA analysis. Inset shows the signature of two different probabilities

**Step 7:** The final step is to get the probability distribution of events from the two analytes as a histogram, after getting rid of the noisy events for which an intensity threshold value is set. A variety of schemes can be used to determine this value, but here a standard thresholding is used. To calculate the probability histogram, consider  $I_1$  and  $I_2$  to be the intensities of SERS signals. The total intensity within a coefficient space with  $x$  and  $y$  co-ordinates is  $I_{\text{tot}} = (xI_1 + yI_2)$  and the fraction of analyte for a certain event in terms of intensity is  $xI_1/|I_{\text{tot}}|$ . Considering the experimental factors such as cross section and concentration, the probability of one analyte is calculated as,  $P_1 = \frac{|x|}{|x+y|} = \frac{1}{1+|\frac{y}{x}|}$ .

### 5.4.2 Bialytle SERS

I use methylene blue (MB) and proflavine (PF) as the molecular pair for bi-analyte experiments to quantify the number of molecules in the gap. These two molecules are very similar chemically and structurally (Fig. 5.3a), and bind inside CB[7] in the same way, at a concentration of  $\bar{n} = 0.2$  dye per 100 nm size nanoparticle. It is important to note that encapsulating MB, PF in CB[7] only one in each also avoids the problem of molecules bunching and giving misleading single-molecule events. MB and PF can be easily distinguished in the 400-460  $\text{cm}^{-1}$  region (Fig. 5.3b,c). The SERS signals of low concentration 50:50 MB:PF mixtures are measured for  $>500$  NPoMs, and the data are analyzed using principal component analysis to find the most distinguishable spectral components (Fig. 5.3d). At this concentration where  $\bar{n} = 0.2$ , the lowest two eigenmodes dominate, corresponding to each molecule alone (Fig. 5.3e,f). This allows us to construct a histogram (Fig. 5.3g) which gives the probability of the two molecular spectra being detected simultaneously in different fractions (right end corresponds to 100% MB, left to 100% PF). As evident, at these low concentrations I find that two molecules are almost never found at the same time, and we are truly in the single molecule regime. This data can be used to construct a 'chemical'  $g_{ch}^{(2)}$ , defined as the probability of detecting two different molecules at the same time, normalized by the probability of finding them both at 100% filling of the CBs (with all the CBs in the NPoM junction filled with either of the molecule). I find  $g_{ch}^{(2)} \sim 0.3$ , much less than 1, which provides a strong evidence for strong coupling with single-molecules. Similar histograms at higher concentrations show the gradual vanishing of single-molecule signatures (Fig. 5.4).

Experiments presented in Chapter 7 are done at  $\bar{n} = 0.2$  to  $\bar{n} = 10$ . Bi-analyte experiments at these concentrations reveal the probabilities of single- and few- molecule

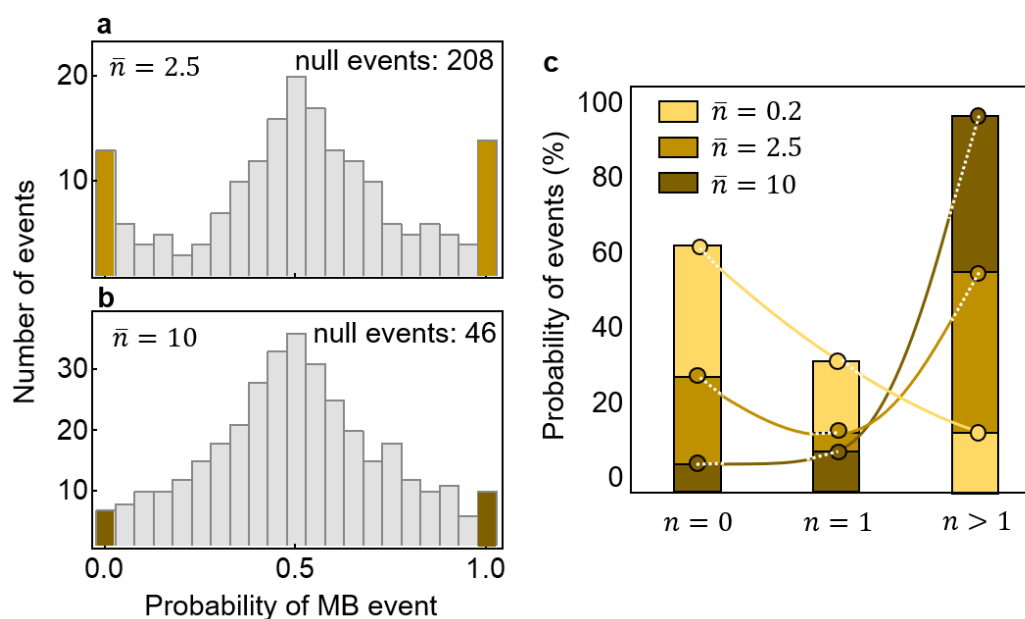


Figure 5.4: **Bi-analyte SERS at different concentrations.** Probability histograms derived from MPCA analysis for (a)  $\bar{n} = 2.5$  and (b)  $\bar{n} = 2.5$  dyes per nanoparticle. (c) Statistics of null events ( $n=0$ ), single-molecule events ( $n=1$ ), and few molecule events ( $n>1$ ) are compared from bi-analyte SERS experiments done at different concentrations. The solid lines connecting the bars are the estimated values from Poissonian statistics.

events (Fig. 5.4a,b). The statistics of null events ( $n=0$ ), single-molecule events ( $n=1$ ), and few molecule events ( $n>1$ ), as well as the levels that would be expected from Poissonian statistics are compared (Fig. 5.4c). For  $\bar{n} = 10$ , most of the nanoparticles seem to give more than one dye molecule as expected, although 20% of nanoparticles still do not show a discernible SERS signal (likely caused by incorrect nano-geometry or tuning, which are removed from the analysis). For  $\bar{n} = 2.5$ , I see the same trend of  $\bar{n} = 0$  nanoparticles both in SERS and dark-field, and the fraction which show single-molecule events is within a factor of 2 from the prediction by theory.

To summarize, for single-molecule SERS it is important to find the right SERS pair of molecules and robust sampling technique, so that the statistics is not biased. To this end, the bianalyte technique in combination with PCA analysis has evolved as the most adopted strategy for rigorously analyzing single-molecule SERS events with comprehensive statistics to confirm single-molecule SERS signatures with high precision. However, it is still hard to tell at the single-nanoparticle level, whether the junction has a single-molecule or not. At room-temperature, molecules undergo a certain degree of dynamics of bending and flexing in the gaps. Time-resolved SERS should ideally reveal this dynamics from

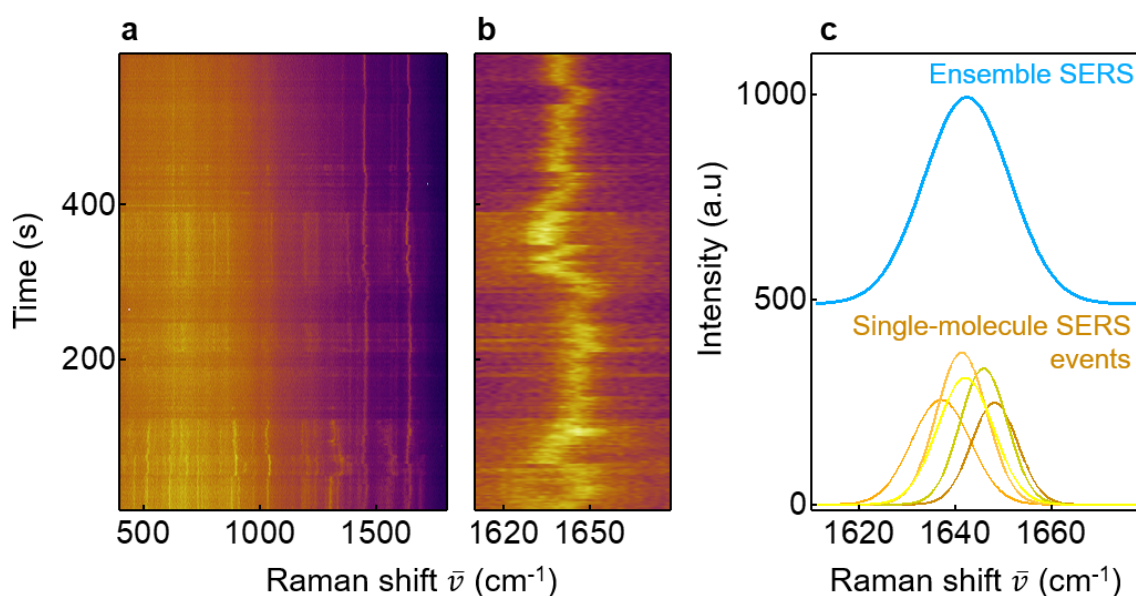


Figure 5.5: **Spectral diffusion of single-molecule SERS.** (a) Time dependent evolution of SERS signal from a CB[7]+MB NPoM which exhibited the signature of single-molecule. Each SERS spectrum is collected for 2 s. (b) Spectral diffusion of vibrational lines of MB is clearly evident, with correlations in the different lines implying their single-molecule origin. (c) SERS line-width of C=C bond strength for single-molecule events is much smaller compared to SERS line-width obtained from  $\bar{n} = 10$ .

fluctuating SERS intensities and peak position, which can only be resolved at the few molecule regime.

### 5.4.3 Time-resolved SERS

Time-series SERS spectra are recorded from NPoMs exhibiting single-molecule signatures at the  $\bar{n} = 2.5$  regime with a Raman pump laser at 633 nm. From the time-series scans (Fig. 5.5a,b) clear spectral diffusion of the vibrational peaks of single MB molecules is observed. Such spectral diffusion is well-studied and is a well-proven evidence of single-molecule events both in the fluorescence and SERS communities. The vibrational shifts for different bonds are seen to be correlated but they can be in opposite directions which can be accounted for, only if they are from individual molecules. This confirms the presence of single-molecules at room temperature. Note that this is completely different when comparing with gaps that are filled with many MB molecules (Fig. 5.5c), which shows no spectral wandering (averaging over many molecules), although some changes in the intensity are seen as molecules sporadically reorient and match the optical field.

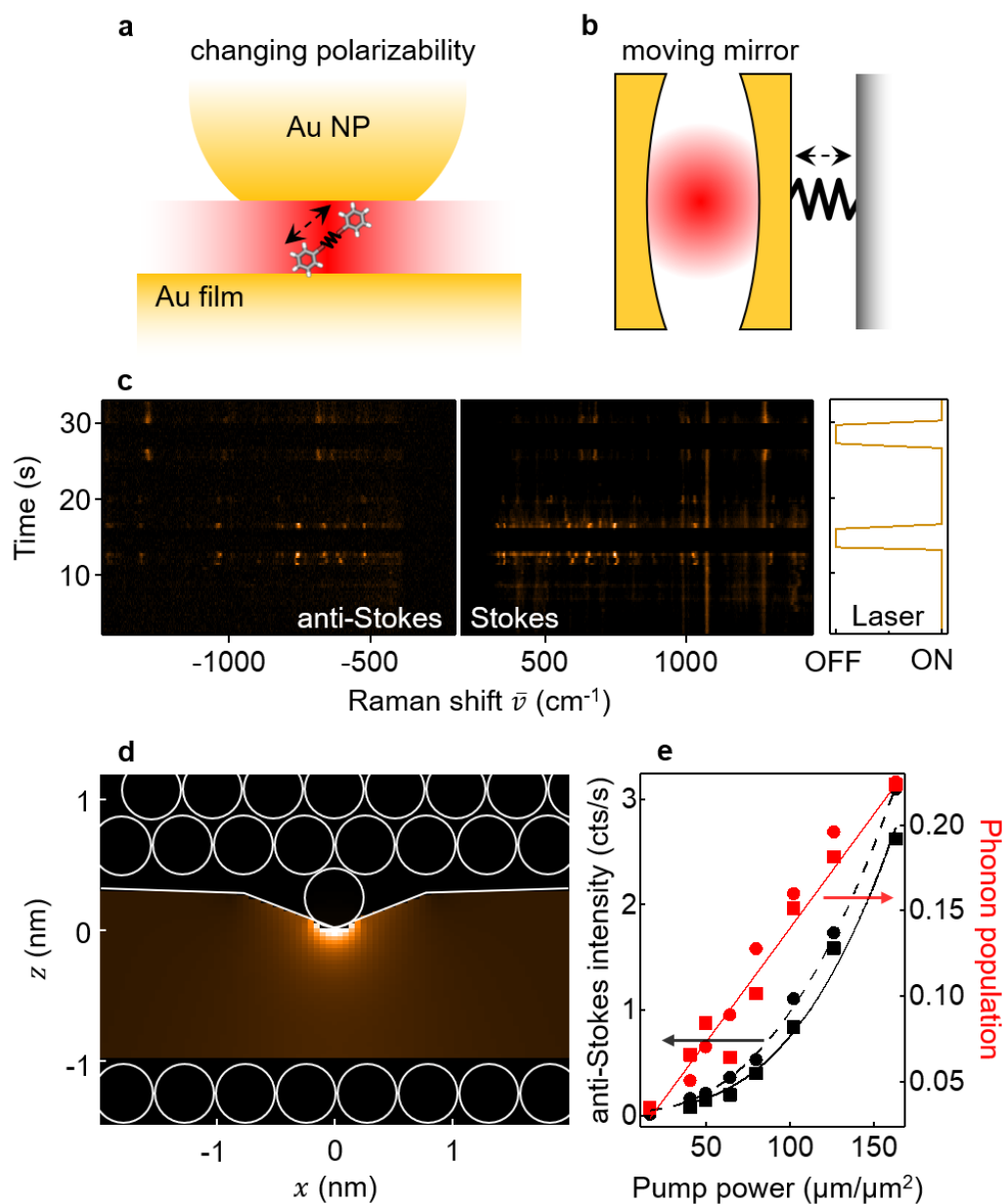


Figure 5.6: **Optomechanics of a single-molecule.** (a) Change in polarizability of a molecule as it vibrates in the plasmonic nanogaps which resembles (b) a vibrating spring in a conventional optomechanical system. (c) Time-series scan of anti-Stokes and Stokes SERS. Two set of lines are observed in Stokes scan. (i) Persistent lines that are ever-present in time and originate from many molecules in the larger nanocavity. (ii) Blinking lines that occasionally occurs over time and are the only modes observed in anti-Stokes scans. These blinking lines originate whenever the Au atoms are plucked from the surface, resulting in further concentration of electric fields as shown (d). (e) Intensity of anti-Stokes lines scales quadratically with the incident laser power, revealing the features of optomechanical pumping of vibrational states.



To further understand the origin of these fluctuation lines, we [174]<sup>5</sup> cooled the sample to 10 K with non-resonant benzene di-thiol (BPT) molecules self-assembled in the gap. The recorded time resolved Stokes and anti-Stokes SERS spectra had two different sets of lines. (i) persistent lines that are ever-present in time and originate from many molecules in the larger nanocavity. (ii) Blinking lines that occasionally occur over time and are the only modes observed in anti-Stokes scans (Fig. 5.6). With rigorous quantum-mechanical theory and density function theory (DFT) simulations it was concluded that the blinking lines originate from the fluctuation in the electromagnetic fields in the gap due to the light-driven mobility of Au atoms. These atoms confine the optical fields to atomic scale ('picocavity'). At room temperature, atoms move spontaneously and hence it is very hard to stop the SERS fluctuations. At 10 K fluctuating Raman lines can be arrested by lowering the input laser-power (Fig. 5.6c). The strong gradient fields around the atom (Fig. 5.6d) break the Raman selection rules and support non-linear pumping of anti-Stokes line (Fig. 5.6e). The intensity scaling of anti-Stokes lines and confined optical fields around an atom supports the theory of quantum optomechanics in which the change in polarizability of a bond as it vibrates act as the optomechanical back-action on cavity modes.

## 5.5 Conclusion

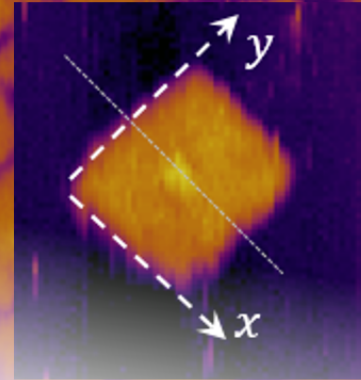
I have provided experimental proof for sensing vibrational fingerprints of single-molecules in plasmonic gaps. NPoMs with self-assembled molecules in the gap provide strong electromagnetic enhancement for SERS on the order of  $10^{10}$ , boosting Raman signatures of single-molecules. Combining guest-host assembly with statistical tools, I could show statistics of single-molecule events at different concentrations. Further, using time-resolved SERS, I could demonstrate signatures of single-molecules in the bending and flexing diffusion of SERS signals.

---

<sup>5</sup>Done in collaboration with Felix Benz, a former PhD student at NanoPhotonics Centre, University of Cambridge, UK



## 6 Mapping Nanoscale Hotspots using DNA-Origami



Fabricating nanocavities in which optically-active single quantum emitters are precisely positioned is crucial for building nanophotonic devices. In this chapter, I discuss self-assembly based on robust DNA-origami constructs that can precisely position single molecules laterally within sub-5 nm gaps between plasmonic substrates that support intense optical confinement. By placing single-molecules at the centre of a nanocavity, I show modification of the plasmon cavity resonance before and after bleaching the chromophore, further quantifying the fluorescence emission enhancements of  $\geq 4 \times 10^3$  with high quantum yield ( $\geq 50\%$ ). By varying the lateral position of the molecule in the gap, the spatial profile of the local density of optical states is mapped with a resolution of  $\pm 1.5$  nm.

## 6.1 Single-emitter in optical cavities

Coherent coupling of light and single-molecules at room temperature is one of the fundamental goals of nano-optics that would enable widespread adoption as a building block of nanophotonic devices. To achieve the desired coherent interaction, integrating optically-active materials (such as molecules, quantum dots, monolayer semiconductors, or diamond vacancy centres) into these cavities is of great importance [63, 175, 176]. Typically this is achieved either by fabricating the cavity around randomly located emitters such as quantum dots or nitrogen-vacancy centres, or randomly placing emitters inside the cavity. In realizing the promising hopes for molecules in plasmonic cavities, the major hurdles are, (i) robust assembly of plasmonic nanocavities with reliable nanogaps ( $d < 5$  nm) and (ii) precise integration of single-molecules into such cavities with a high degree of spatial control.

Here I construct a NPoM cavity with  $< 5$  nm gap between faceted gold nanoparticle and gold film, and show the freedom to place a single emitter at controlled positions inside it (Fig. 6.1a). The plasmonic coupling between the nanoparticle and the image charge in film enhances the electromagnetic field in the gap by nearly two orders of magnitude and tightly confines the fields to spatial volumes  $V_m < (6 \text{ nm})^3$  [74, 177], resulting in a high local density of optical states (LDOS) in the gap (Fig. 6.1b). In lateral directions ( $x, y$ ), the fields are strongly confined underneath the bottom facet of the nanoparticle of radius  $R$  to lateral intensity full-width  $\Delta_c \sim \sqrt{2Rd}/n$  with gap refractive index  $n$  [160] (Fig. 6.1c). These cavity fields have a strong radiative component delivering high coupling efficiency to the far-field,  $\eta \geq 0.5$  [59, 75]. A two-level emitter positioned in the gap experiences high LDOS and its emission is strongly enhanced ( $\propto 1/V_m$ ). An emitter can thus be used to map these confined fields. However, it is challenging to precisely position a single-emitter within gaps of  $< 5$  nm with nm lateral resolution.

Among various techniques used to assemble molecules in the cavity (discussed in Section 3.3), here I use a self-assembled DNA origami (DNAo) method. DNAo is programmed to assemble on a metal surface and bind a Au NP at specific coordinates, resulting in a NPoM cavity with DNAo spacer. Subsequently, a functionalizing DNAo spacer single-dye (Cy5) molecule is precisely positioned at the centre of nanogap. In such a system, I show that the coherent coupling of cavity and emitter results in the modulation of the cavity scattering spectrum. In addition, I map the LDOS with  $< 3$  nm precision by

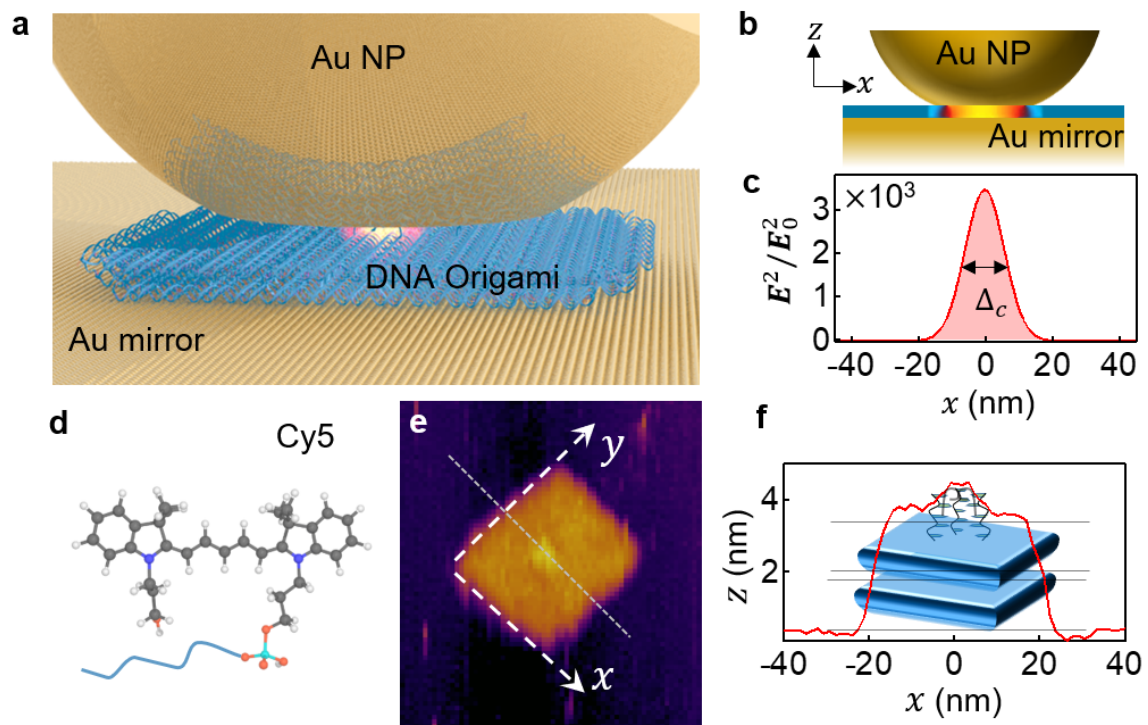


Figure 6.1: **Assembled plasmonic nanocavity with single-molecule DNA origami plates.** (a) NPoM with faceted nanoparticle and DNAo in the gap. (b) Nanoparticle-on-mirror (NPoM) cavity with strong optical field confinement in the gap (yellow). (c) Electric field enhancement in the gap along the  $x$ -direction, 80 nm diameter NP with 15 nm bottom facet. (d) Chemical structure of a Cy5 molecule positioned in the NPoM gap. (e) Zoomed AFM image of a single DNAo. (f) Line profile along the dotted white line shown in (e).

displacing the single-Cy5 molecule through the cavity in the lateral direction by varying the DNA binding site.

## 6.2 Assembly of a single-molecule in NPoM gaps

The DNAo is designed as a 2-layer plate. The bottom layer has 4 thiol modifications on specific staple strands which are used to bind the origami onto the flat Au mirror. The top layer contains 6 poly-A (10 adenine bases on the 3') overhangs that can bind to the nanoparticle. ssDNA-coated-nanoparticles hybridize to locate the centre of the nanoparticle bottom facet there. The AFM images of these DNAo on a Au surface confirm a uniform size distribution and high yield assembly (Fig. 6.1e). The zoomed AFM images (Fig. 6.1e) of individual structures show the clear features of these overhangs at the centre and

give the average thickness of the 2-layer plates as  $4.5\text{ nm}\pm 0.3\text{ nm}$  (Fig. 6.1f). The top plate is designed to bind Cy5-modified staples (chemical structure shown in Fig. 6.1d) which are 3' modified to locate them at coordinates divisible by 5 nm in the  $y$ -direction or internally modified stands to locate single Cy5 at  $\pm 2.5$  and  $\pm 7.5$  nm positions. The resultant assembly yields nanoparticles on a flat metal surface with the ultra-narrow gap (NPoM cavity) filled with DNA origami and a single-Cy5 molecule at the centre (Fig. 6.1d). The optical emission of Cy5 from such a cavity is enormously enhanced due to the high LDOS within the gap (Fig. 6.1b).

### 6.3 Optical characterization of nanocavities

The robustness of assembled NPoM cavities are characterized for  $>350$  nanoparticles using white-light dark-field nano-spectroscopy [51]. To first quantify the optical gap between the nanoparticle and Au mirror ( $d$ ) and the refractive index ( $n$ ), empty NPoMs without the Cy5 are constructed (Fig. 6.2a). Spectra of single NPoMs (Fig. 6.2b) show near identical peak positions, intensities and peak widths, further verifying the consistency of our robust nano-assembly.

A characteristic infrared resonance peak ( $\omega_c$ , empty cavity) is identified at  $1766\pm 40$  meV ( $702\pm 18$  nm) in the wavelength-dependent scattering spectra which corresponds to the NPoM coupled plasmon resonance. Spectral variations in the small peak around 530 nm indicate an average deviation in nanoparticle size of  $\pm 5$  nm [54]. The AFM-measured thickness is used in electromagnetic simulations allowing extraction of the effective refractive index of the DNAo, which is modelled as an infinitely-wide sheet to simplify the geometry. The simulated coupled mode resonance positions and linewidths for different refractive indices in the gap ( $n=1.9, 2.1, 2.3$  and  $2.5$ ) are plotted (green dots) along with the experimental data for  $>350$  individual NPoMs (Fig. 6.2c). The statistical variation in  $\omega_c$  and resonance full width at half maximum ( $\Gamma_c$ ) fits  $n=2.15$ , in good agreement with previous studies of DNAo in closer proximity to Au [178]. However, estimating the accurate value  $n$  is challenging as the thickness of DNAo in NPoM geometry can be different from the measured values using AFM. Such a deviation might arise due to variations in the vapour pressure of water in nanogaps, van der Waals forces between two Au surfaces or a change in local salt concentrations. A decrease in the DNAo thickness in NPoM by  $\leq 30\%$  can lead to an effective refractive index of DNAo in the range of 1.5–1.7. An increase in nanoparticle size would shift  $\omega_c$  to lower energy and increase  $\Gamma_c$ . Occasional linewidths

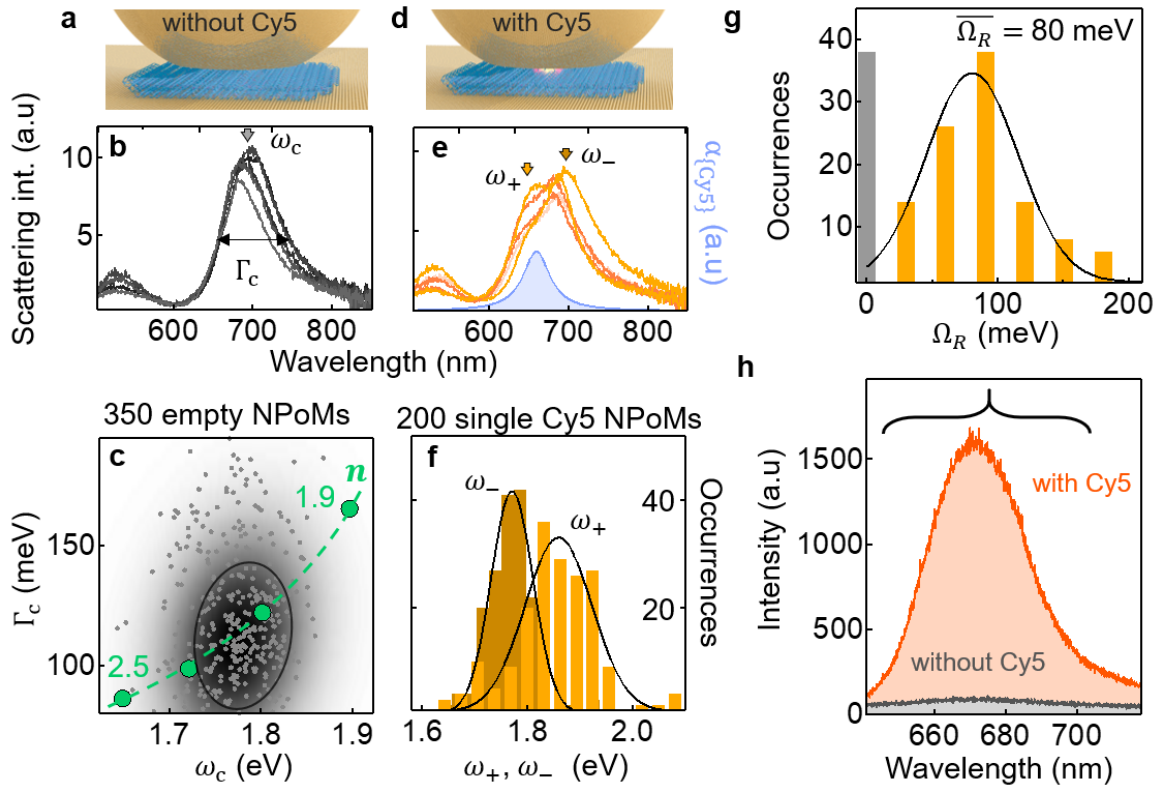


Figure 6.2: **Characterization and coherent coupling with single-Cy5 in NPoM.** (a,d) NPoM without and with Cy5 molecule in DNAo. (b,e) Experimental dark-field scattering of five individual NPoMs, with resonance peaks  $\omega_c$  and linewidths  $\Gamma_c$  marked. Absorption spectrum of Cy5 is also shown (blue). (c,f) Cavity resonances vs linewidths for  $>200$  NPoMs without (with) single Cy5 molecules. Background colour map is kernel density matrix indicating the distribution of NPoMs. Green dots are simulations for  $n=1.9$  to  $2.5$ . (g) Distribution of calculated Rabi couplings extracted from (f). Fraction of uncoupled NPoMs with  $g=0$  highlighted in grey bar. (h) Optical emission from NPoMs with and without Cy5 molecule in the DNAo, laser at 633 nm. Curly bracket denotes the spectral window used to integrate signal counts for enhancement factor.

$<80$  meV likely arise from the precise nano-geometry; the contact angle at the nanoparticle facet edge modulates the coupling strength between the cavity and radiating antenna modes [159]. The lack of correlation between  $(\omega_c, \Gamma_c)$  suggests that the nanoparticle size is uncorrelated to the facet morphology. The robustness of  $\omega_c$  and  $\Gamma_c$  for such large samples of DNAo nanocavities verify that this DNAo method allows for great control in the nanocavity formation, with uncertainties arising only from the fluctuations in nanoparticle shape and geometry.

## 6.4 Coherent coupling of NPoM with a single-Cy5 molecule

The NPoM cavity is designed with  $2R=80$  nm so that the absorption and emission from the Cy5 molecule spectrally overlaps with the plasmon resonance  $\omega_c$ . The simulations predict the field enhancements give large Purcell factors ( $F_P \propto Q/V_m$ ), up to 4000 for single-Cy5 molecules embedded in the gap region [59] (Fig. 6.1a). The largest enhancements occur for Cy5 located at the centre of the nanoparticle when the transition dipole is oriented vertically. Due to the unique plasmon mode hybridization in the NPoM nanocavity, this large field excitation is not quenched into non-radiative channels, as typically occurs when an emitter is placed close to a metal surface. Instead, in the NPoM nanocavity quenching is suppressed, leading to enhanced emission for the molecule that can be measured in the far-field.

By incorporating a single-Cy5 molecule into DNAo that assembles the NPoM (Fig. 6.2d), the optical scattering from the system is perturbed due to the presence of single-Cy5 molecules. The resulting cavity resonance coupled with the single-Cy5 now shows two peaks which can be clearly resolved ( $\omega_{\pm}$ ), and for which I obtain their distributions from  $>200$  NPoMs (Fig. 6.2f). Coherent coupling of the single-Cy5 absorption and emission (at  $\omega_0$ ) with the detuned NPoM cavity does not quite reach the strong coupling regime of clear peak splittings.

The emitter dephasing rate  $\Gamma_0$  at room temperature is estimated to be 25 meV ( $\sim k_B T$ ). The distribution of extracted coupling strengths for all NPoMs (Fig. 6.2g) gives a mean Rabi splitting  $\overline{\Omega_R}=80$  meV, so that indeed  $\Omega_R \sim (\Gamma_c + \Gamma_0)/2$  here (Fig. 6.3). This is at the transition between weak and strong coupling regimes. The system approaches strong coupling, but the spontaneous emission rate still follows a Purcell-like dependence proportional to  $g^2$  [179], valid for  $g/\omega_0 < 0.1$  (here  $g/\omega_0=0.03$ ). Compared to my other recent results presented in Chapter 7, the wider gap (4.5 nm vs 0.9 nm) but larger dipole strength of Cy5 ( $\mu=10.1$  D) [9] and twofold increase in damping (from the larger NP), gives a coupling rate  $g$  only slightly smaller than the coupling rate in narrow gaps. Recent related efforts to position single-molecules between plasmonic dimers with large gaps  $>10$  nm suppressed the  $g$  to small values and only weakly enhanced emission rates [135, 180, 181]. The range of extracted Rabi splittings seen in Fig. 6.2g can originate from fluctuations in orientation and position of the Cy5, but can also arise from a sub-population of bleached single Cy5 molecules, as discussed in the following section.



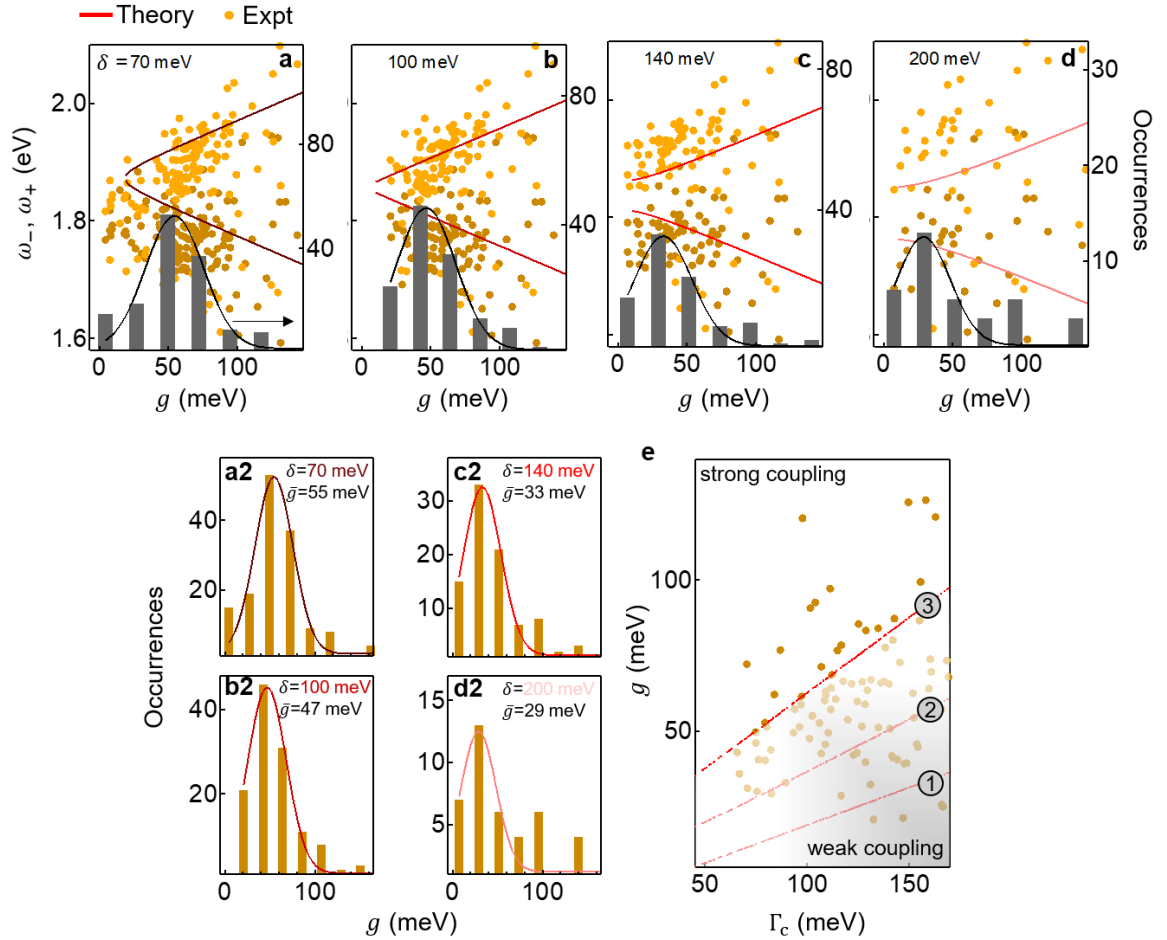


Figure 6.3: **Estimating coupling strength.** (a-d) Calculated dispersion of polariton modes (solid lines) as a function of coupling strength obtained from Eq. (2.18) for different detuning parameters ( $\delta = \omega_c - \omega_e$ ). Points show experimentally obtained energies of polariton modes by fitting double Gaussian to the scattering spectrum vs estimated. (a2-d2) (replotted for clarity) Histograms of coupling strength obtained from different detuning parameters, fitted with Gaussian (solid line, colour coded with (a-d) top) to estimate  $\bar{g}$ . (e) Dispersion of coupling strength vs cavity damping rate (points) for  $\delta = 100$  meV, the conditions for strong coupling obtained from equations 2.20, 2.21 and 2.22 shown as dashed lines numbered 1, 2 and 3 respectively. Points with values above the line 3 fall into strong coupling regime and below the line are weak coupling.

## 6.5 Emission from a single-Cy5 in NPoMs

The presence of a single-Cy5 not only perturbs the cavity scattering but also enhances the optical emission from the Cy5 molecule. To measure the emission from individual NPoMs, each cavity is pumped at 633 nm and all Stokes-shifted photons are collected. In the absence of Cy5 molecules in the nanogap, the emission spectrum of a single NPoM is dominated by the surface enhanced Raman scattering (SERS) of DNAo and the inelastic light scattering (ILS) of electrons in Au from the plasmon resonance [182, 183] (Fig. 6.2h, grey). The combined intensity of both the phenomena vary across different NPoMs. At relatively high pump powers  $>200 \mu\text{W}/\mu\text{m}^2$ , strong SERS signatures are identified at  $1500 \text{ cm}^{-1}$  corresponding to cytosine, and at  $1000 \text{ cm}^{-1}$  and  $730 \text{ cm}^{-1}$  corresponding to adenine of DNA-origami. When a single-Cy5 is present at the centre of the gap the emission from the NPoM is strongly enhanced (Fig. 6.2h, orange). Different NPoM constructs show only minor variations in peak emission wavelength and widths. The emission of Cy5 coupled to the plasmon mode enhances the decay rates and modifies the energy levels giving larger surface-enhanced fluorescence linewidths in comparison with the ensemble emission of molecules in solution (Fig. 6.2h, yellow).

Time series scans of the emission from NPoMs containing a single Cy5 show variations in peak position and intensity on timescales of seconds (Fig. 6.4a). The emission suddenly bleaches after a certain time, leaving only weak ILS and SERS from the NPoM ( $t > 21 \text{ s}$  in Fig. 6.4a) which is the same for the DNAo without Cy5 (Fig. 6.2h, grey). This confirms the presence of only one Cy5 molecule in each NPoM, as previously demonstrated for single emitters within DNAo inside plasmonic dimers [133, 135]. Scattering spectra obtained from the NPoM before (Fig. 6.4b, bottom) and after (Fig. 6.4b, top) the bleaching of the single-Cy5 show the expected collapse in the splitting. Intensity traces from fluorescence microscopy images of NPoMs also show these step-like features, in complete contrast to ensemble Cy5s on glass which show the gradual irreversible bleaching of molecules. We note that chemically binding Cy5 to DNA stands has been shown to increase the photo-stability of the molecules [73, 136, 184, 185]. The average bleaching time of Cy5-DNAo on glass is  $\bar{\tau}_b = 8.5 \text{ s}$ , whereas in these NPoMs we find  $\bar{\tau}_b > 13 \text{ s}$ , giving an additional two-fold increase in photo-stability. With NPoMs providing local intensity enhancements of  $I_{\text{gap}} \sim 2500$  in the gap (Fig. 6.1c) and  $\tau_b \propto 1/I_{\text{gap}}$ , the photobleaching is actually suppressed by more than three orders of magnitude. The total number of photons emitted from the single dye in each NPoM before it bleaches is estimated to be  $4 \times 10^6$ , resulting in an enhancement of total photon counts by factors  $>1000$  times

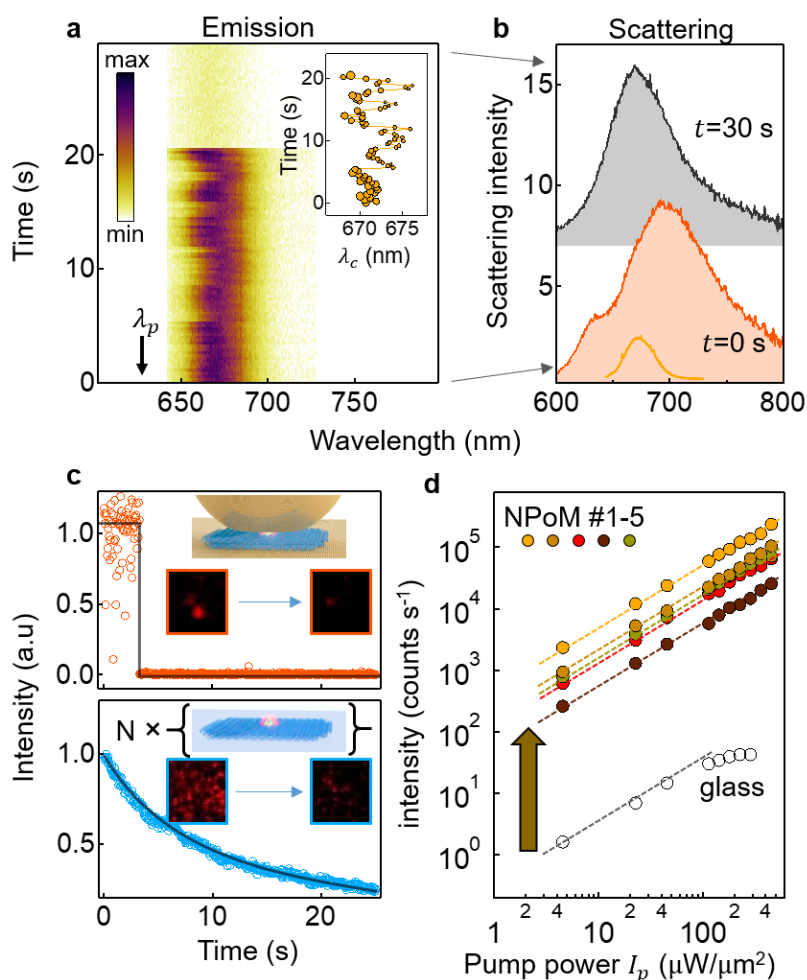


Figure 6.4: **Emission from NPoM with a single-Cy5.** (a) Time-series emission spectra from a NPoM with a single-Cy5 at the gap centre. Inset: extracted variation in peak  $\lambda$  and intensity (dot size) as a function of time. (b) Scattering spectra from the NPoM before ( $t=0$  s) and after bleaching ( $t=30$  s) the single-Cy5, with initial emission spectrum (orange). (c) Intensity over time extracted from fluorescence microscopy images (shown in inset) for single-Cy5 in NPoM (top) and ensemble Cy5 embedded in DNAo on glass (bottom). (d) Emission intensity as a function of pump power in five individual NPoMs and on glass.

compared to each Cy5 in DNAo on glass. This enhancement results from combined effects of enhanced radiative emission rates, better light collection from the NPoM antenna, and suppressed bleaching rates [136, 185]. These behaviors fully corroborate our evidence for single molecule emission.

To estimate the emission enhancement of Cy5 molecules in NPoMs I performed emission experiments for different pump powers. Emission from an ensemble of Cy5 molecules on glass exhibits saturation and bleaching at  $>100 \mu\text{W}/\mu\text{m}^2$  (Fig. 6.4d, black curve). The emission here is integrated over a range of wavelengths (curly bracket Fig. 6.2h) and normalized to the counts from Cy5s in DNAo on glass considering the excitation and collection efficiencies, to give the enhancement factor (EF). The radiative emission rate ( $\gamma_e/\gamma_0$ ) is found to be enhanced by  $\text{EF} > 2 \times 10^3$ . The coupling strength estimated from this single-Cy5 enhancement [12] using  $g^2 = F_P \gamma_0 \Gamma_c (1 + 2\delta/\Gamma_c)/4$  (with radiative linewidth  $\hbar/\gamma_0 = 1 \text{ ns}$  [186]) gives values  $g \sim 50 \text{ meV}$  which agree with those from the cavity linewidth in scattering (Fig. 6.2g). The emission intensity from a Cy5 coupled to a single NPoM shows linear scaling with excitation power density in the range  $4\text{--}400 \mu\text{W}/\mu\text{m}^2$  (Fig. 6.4d). The photon population in the NPoM is  $< 0.1$ , well below the critical cavity photon population [57] for non-linear effects. Pumping at higher excitation power densities instead gives irreversible photobleaching of the Cy5, before saturation of the excited state population can be reached. All subsequent measurements are thus conducted at excitation power densities of  $50 \mu\text{W}/\mu\text{m}^2$ .

## 6.6 Spatial mapping of local fields

The EF is measured for  $>100$  individual NPoMs for different assembled origamis. In successive designs, the spatial position  $x$  of the single-Cy5 is systematically scanned laterally within the gap (Fig. 6.5). As the Cy5 is moved towards the centre of the gap ( $x=0$ ) the emission intensity increases monotonically, evidencing that the centre of the NP on the DNAo is correctly defined within  $\pm 1 \text{ nm}$ , and that the optical field in the gap has a spatial fullwidth of  $\Delta_{\text{expt}} = 6.5 \pm 2 \text{ nm}$ . This measured intensity profile is similar to that from simulations  $\Delta_c \sim 8 \text{ nm}$  for facets  $w < 10 \text{ nm}$  (blue lines in Fig. 6.5) as well as the analytical estimate  $\sqrt{2Rd}/n \sim 9 \text{ nm}$ . The statistical variation of EFs for each design (shown with violin plots around each point) shows the deterministic assembly achieved here. To the best of my knowledge, this is the first time the optical field of plasmonic nanogaps is mapped deterministically with single-molecules. This measurement also confirms the accuracy of the

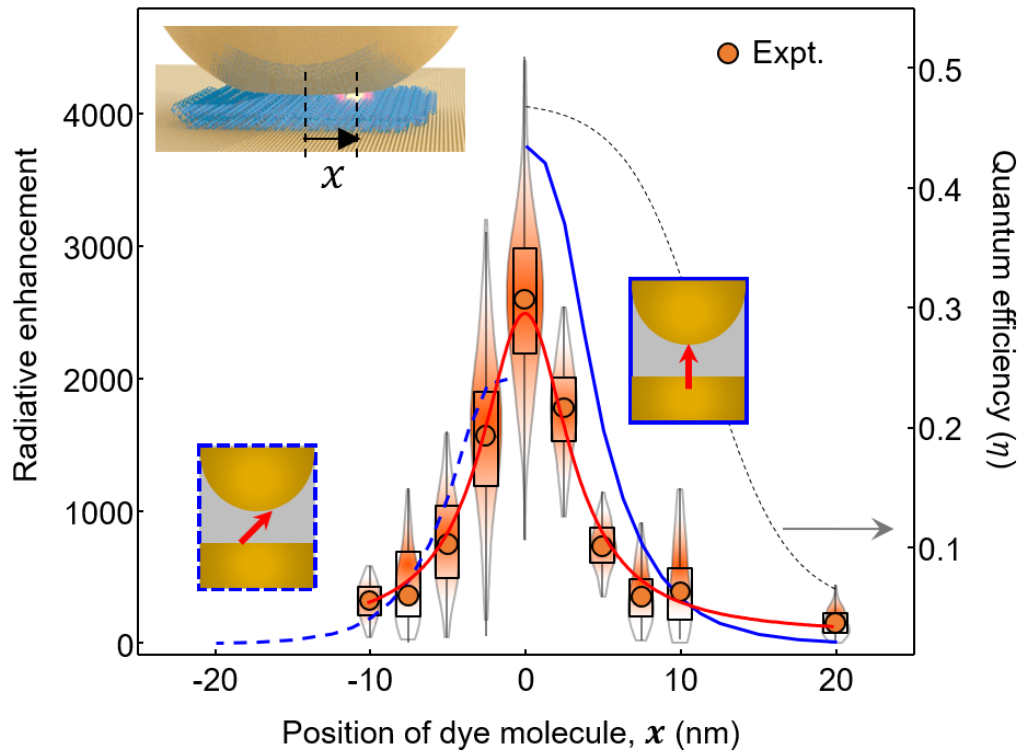


Figure 6.5: **Mapping the LDOS.** Experimental variation in the enhancement of emission intensity from NPoMs while laterally displacing the position of single dye molecules (orange dots), normalized to the emission of a single Cy5 in DNAo on glass. Grey box indicates standard error and statistical variations in emission intensity shown as violin plots. Solid red line is the Gaussian fit to the experimental data. Theoretically calculated emission enhancements are shown for vertical ( $90^\circ$ ) dipole (solid blue) and slanted ( $45^\circ$ ) dipole (dashed blue). Calculated quantum efficiency for vertical dipole is shown as dashed grey line.

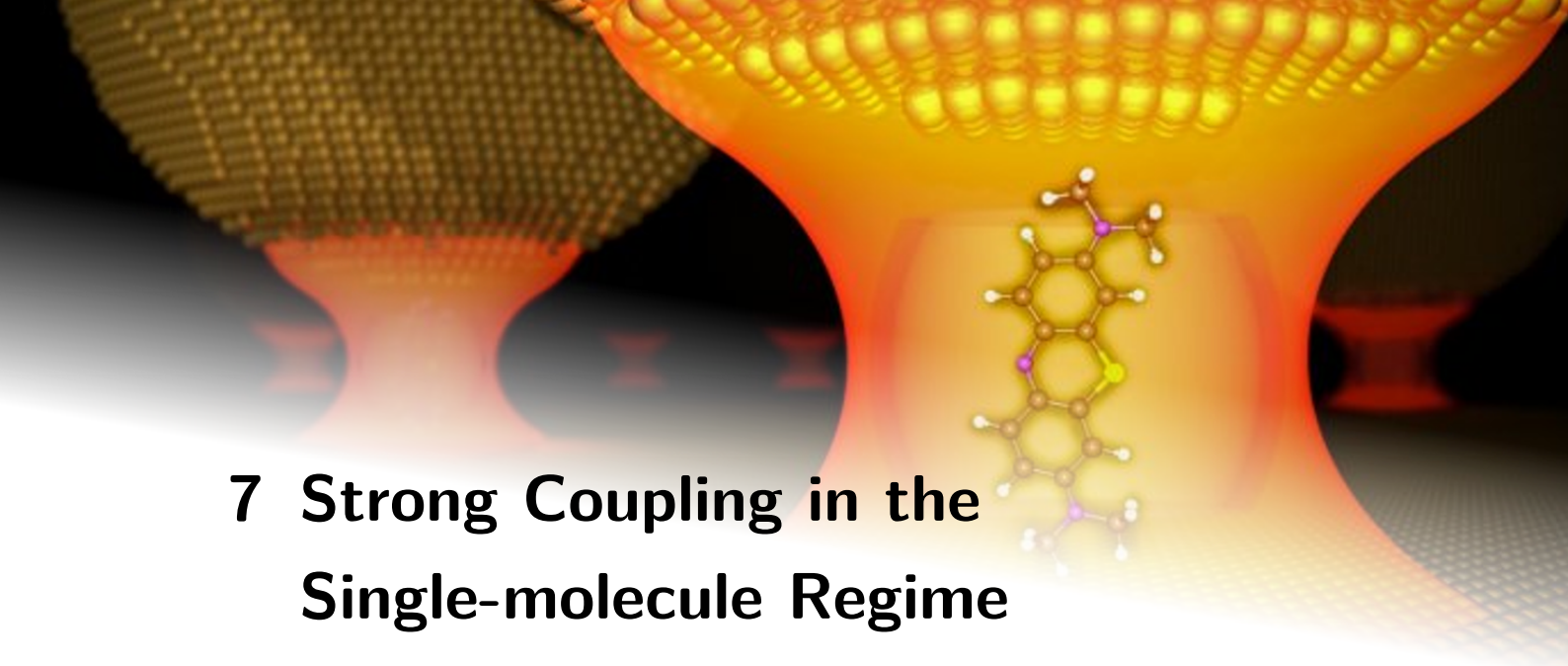
single-molecule Cy5 positioning within DNAo to  $<1.5$  nm (as this would otherwise blur out the spatial fullwidth further). Compared to near-field scanning microscopies with metal tips that strongly perturb the confined optical mode, the present technique for measuring cavity optical fields using deterministic placement through DNA origami is minimally invasive [187, 188].

The experimental data matches full 3D electromagnetic simulations for the radiative enhancement with two different dipole orientations ( $90^\circ$  and  $45^\circ$  shown in solid and dashed lines in Fig. 6.5). I find the best fit for dipole orientations of  $65^\circ \pm 15^\circ$ . Different DNA-origami folding results in slightly different dipole orientations, and partial melting of the double-stranded DNA together with slight imprecision in nanoparticle placement yields the uncertainty in emitter position.

It is evident from this data that an emitter in a plasmonic nanocavity does not quench when placed in the vicinity ( $<5$  nm) of the two Au surfaces. This is a consequence of the enhanced emission rate outstripping the absorption rate in the metal, as shown earlier [59]. Instead its emission rate is strongly enhanced when moved towards the centre of the nanocavity. It is important to note that this NPoM geometry is completely different from the case where quenching is observed when emitters are placed close to a *single* Au surface.

### 6.7 Conclusion

Integrating robust NPoM constructs with high precision DNA origami techniques, I show that a single-molecule deterministically positioned at the centre of a nanocavity interacts coherently with confined optical fields ( $\Omega_R \sim 80$  meV) producing splitting near the weak-to-strong coupling regime. Modification of the scattering spectra before and after bleaching each single-Cy5 shows the operation of 3 zJ energy switching at room temperature, which although currently irreversible can be explored with photochromic and electro-optic molecules. The optical emission from each single-molecule can be enhanced by  $>10^3$  showing that our NPoM constructs allow for strong fluorescence despite the close proximity of the dye to metal surfaces. Further, by systematically moving the position of the molecule through the cavity, I map the local field confinement with high accuracy. I believe that such robust systems are ideal for studying room-temperature single-molecule nano-optics, and have the potential for a variety of technological implementations.



## 7 Strong Coupling in the Single-molecule Regime

Emitters placed in an optical cavity experience an environment that changes how they are coupled to the surrounding light field. In the weak-coupling regime light extraction from the emitter is enhanced, but more profound effects emerge in the single-molecule strong-coupling regime where mixed light-matter states are produced [76, 189]. Individual two-level emitters in such cavities become non-linear for single photons, forming key building blocks for quantum information systems as well as ultra-low power switches and lasers [58, 190–192]. Such cavity quantum electrodynamics has until now been the preserve of low temperatures and complex fabrication, severely compromising their use [58, 193, 194]. However, the nanoparticle-on-mirror (NPoM) cavity can be utilized for strong mixing of an optical mode and exciton resonance of a single-molecule. This dressing of molecules with light can modify photochemistry, opening up the exploration of complex natural processes such as photosynthesis [195] and the possibility of manipulating chemical bonds [196].

## 7.1 Optical niche for strong-light matter coupling

Creating strongly-coupled mixed states from visible light and individual emitters is severely compromised by the hundred-fold difference in their spatial localization (Chapter 2). To overcome this, high-quality cavities are used to boost interaction times and enhance coupling strengths. However, in larger cavities the longer round trip for photons to return to the same emitter decreases the coupling, which scales as  $g \propto 1/\sqrt{V_m}$  with the effective cavity volume  $V_m$ . This coupling has to exceed both the cavity loss rate  $\gamma_c$  and the emitter scattering rate  $\gamma_e$ , in order for energy to cycle back and forth between matter and light components, requiring  $2g > \gamma_c, \gamma_e$  [56]. For cryogenic emitters [58, 192] (laser-cooled atoms, vacancies in diamond or semiconductor quantum dots), the suppressed emitter scattering allows large cavities (with high quality factor  $Q \propto \gamma_c^{-1}$ ) to reach strong coupling. Severe technical challenges however restrict energy, bandwidth, size and complexity of devices. Progress towards room temperature is limited by the unavoidable increase in emitter scattering and the difficulty of reducing the volume of dielectric-based microcavities at wavelength  $\lambda$  and refractive index  $n$  below  $V_\lambda = (\lambda/n)^3$ .

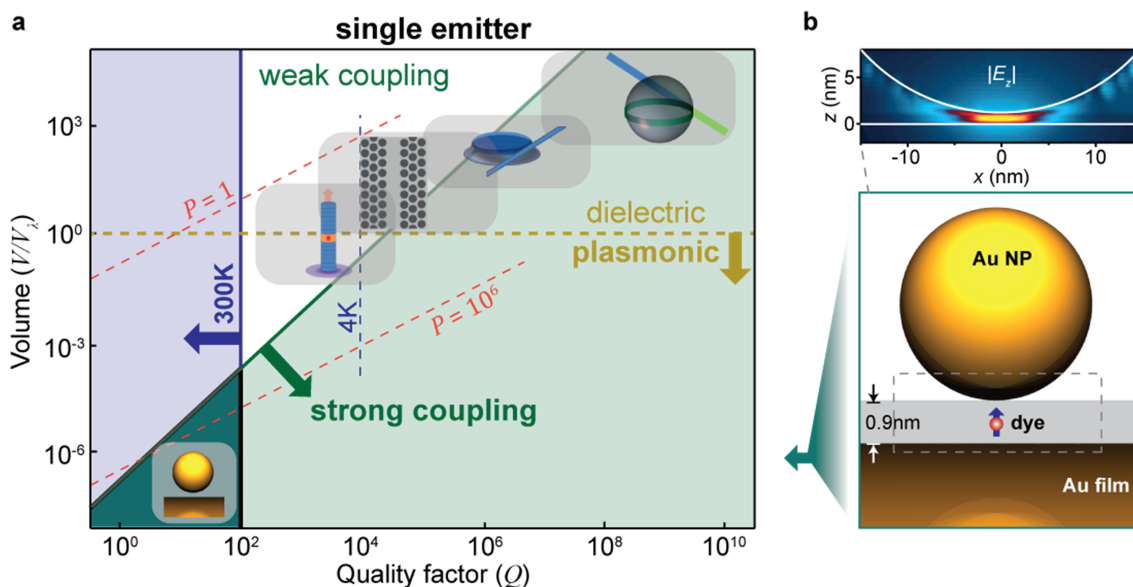


Figure 7.1: **Comparing single-molecule optical cavities.** (a) Cavity  $Q$ -factors and effective volumes (compared to  $V_\lambda = (\lambda/n)^3$ ), showing strong-coupling (green), room-temperature (blue), and plasmonic (orange) regimes for single emitters. Icons (from right) show whispering gallery sphere, microdisk, photonic crystal, micropillar, and nanoparticle on mirror geometry (NPoM), with Purcell factor  $P$  (red) in  $\mu\text{m}^{-3}$ . (b) Schematic of NPoM, blue arrow in gap locates emitter transition dipole moment. Inset: Simulated near-field of coupled gap plasmon in dashed box with maximum electric field enhancement  $\propto 400$ , oriented vertically ( $z$ ).



At room temperature  $T$ , typical scattering rates for embedded dipoles  $\gamma_e \sim k_B T$ , imply using  $Q < 100$  which then requires cavities where,  $V_m < 10^{-5} V_\lambda$  (Fig. 7.1a, dark green shaded) to maximize the coupling. Improved confinement uses localized surface plasmons (Fig. 7.1a) combining oscillations of free electrons in metals with electromagnetic waves [163]. While structured metal films can couple molecular aggregates of high oscillator strength, far too many molecules are involved for quantum optics [80, 81, 95].

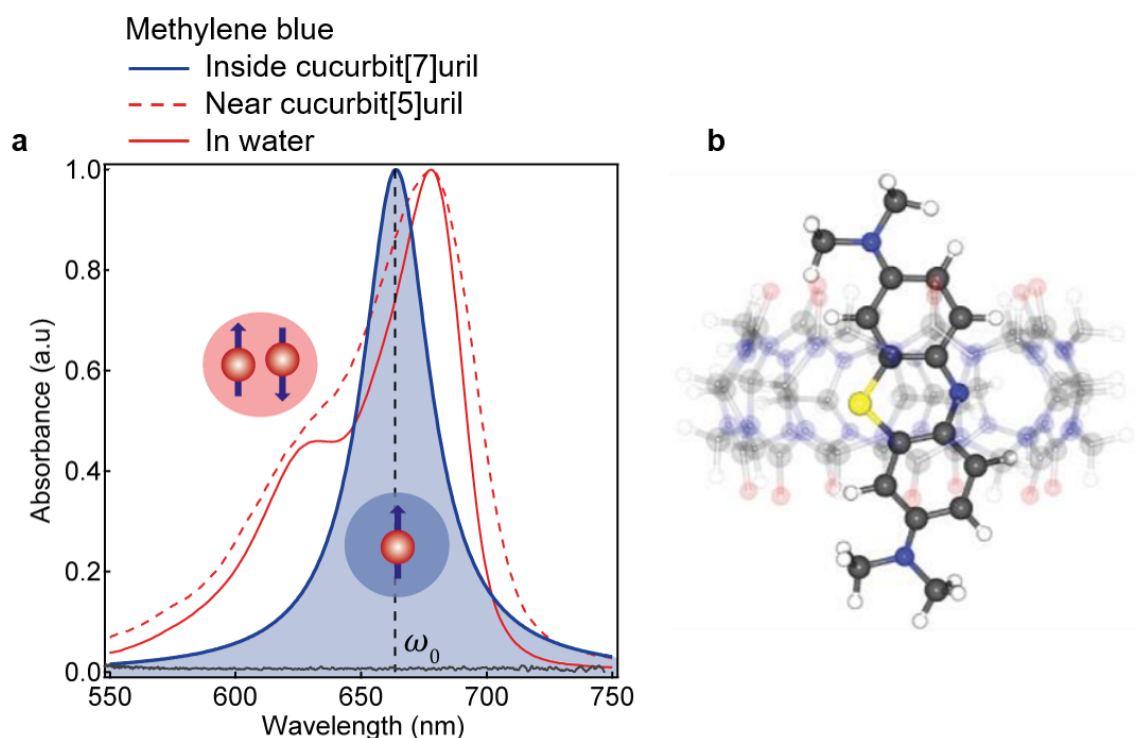


Figure 7.2: **Plasmonic nanocavity containing dye molecule.** (a) Absorption spectrum of methylene blue (MB) in water, with (blue) and without (red) encapsulation in CBs of different diameter. (b) Illustration of a MB molecule in cucurbit[7]uril guest.

## 7.2 Guest-host chemistry

To create such small nanocavities and orient single molecules precisely within them, I use bottom-up nano-assembly. Although field volumes of individual plasmonic nanostructures are too large [76, 189], stronger field enhancements occur within sub-nanometre gaps between paired plasmonic nanoparticles. I utilize the NPoM geometry [50], placing emitters in the gap between nanoparticles and a mirror underneath (Fig. 7.1b). This gap is

accurately controlled to sub-nanometre, easily made by depositing monodisperse metal nanoparticles onto a metal film [51, 148, 197]. The intense interaction between each nanoparticle and its image forms a dimer-like construct with enhancements  $|E|/|E_0| \simeq 10^3$  and an ultralow mode volume. I use 40 nm diameter gold nanoparticles (AuNP) on a 70 nm thick Au film, separated by a 0.9 nm molecular spacer (see below). The coupled plasmonic dipolar mode is localized in the gap (Fig. 7.1b), with electric field oriented vertically ( $z$ ). The resonant wavelength is determined by nanoparticle size and gap thickness, allowing it to be tuned from  $\lambda_c=600\text{--}1200$  nm [51].

Several key aspects are critical to position a quantum emitter inside these small gaps. One is to prevent molecular aggregation, which commonly occurs. Another is to ensure that the transition dipole  $\mu$  is perfectly aligned with the gap plasmon (along  $z$ ). I use a common dye molecule methylene blue (MB) with molecular transition at 665 nm, to which the plasmons are tuned. To avoid aggregation of the dye molecules and to assemble them in the proper orientation, I utilize the host-guest chemistry of macrocyclic cucurbit[ $n$ ]uril molecules, in which guest molecules can sit (Fig. 7.2b) [198, 199]. As discussed previously (Ch. 3.2) cucurbit[7]uril (CB[7]) is water soluble and can accommodate only one MB molecule inside. Encapsulation of MB inside CB[7] is confirmed from absorption spectroscopy (Fig. 7.2a) since MB dimers (additional peak at 625 nm, red) disappear on mixing low MB concentrations with CB[7] (1:10 molar ratio) (blue). Control experiments with smaller CB[5] molecules (into which MB cannot fit) do not remove this shoulder peak (dashed), ruling out parasitic binding. Placing single MB molecules in CB[7] thus avoids any aggregation. Carbonyl portals at either end of the 0.9 nm-high CB[ $n$ ] molecules bind with their rims flat onto the Au surface (Ch. 3.2). When a monolayer of CB[7] is first deposited on the gold mirror and suitably filled with MB molecules, Au NPs bind on top to form the desired filled nanocavity with the MB molecule aligned vertically in the gap. From the calibration of gap size, refractive index of the gap and the variation in nanoparticle size (Fig. 2.8), it is estimated that the empty CBs have a gap size of 0.9 nm with refractive index of 1.4 [51].

### 7.3 Few molecule strong coupling

Dark-field scattering spectra from individual NPoMs show the effect of aligning the emitter in different orientations (Fig. 7.3a). With  $\mu$  parallel to the mirror (top, without CB the MB lies flat on the metal surface), the resonant scattering plasmonic peak is identical to

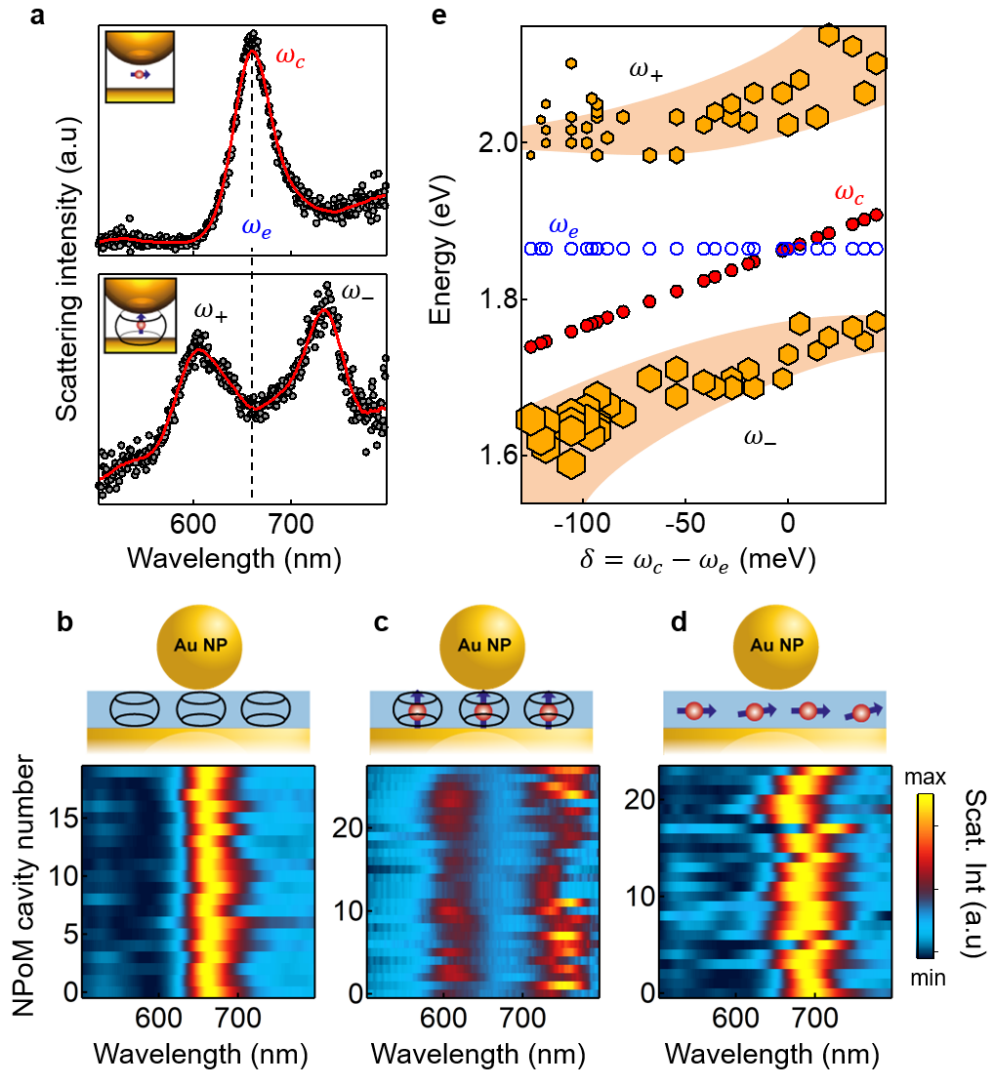


Figure 7.3: **Strong coupling seen in scattering spectra of individual NPoMs.** (a) Scattering spectra from isolated NPoM coupled with dye  $\mu_m$  oriented (top) perpendicular and (bottom) parallel to  $|E_z|$  of gap plasmon (blue dashed line indicates dye absorption wavelength). (b-d) Comparison of scattering spectra from different NPoMs (schematics top), with gaps filled by (b) CB[7] monolayer which are empty, (c) encapsulating MB dye molecules, and (d) MB molecules directly deposited on Au surface. (e) Resonant positions of MB ( $\omega_e$ ), plasmon ( $\omega_c$ ) and hybrid modes ( $\omega_+$  and  $\omega_-$ ) as a function of extracted detuning. Marker size depicts the amplitude in scattering spectra.

NPoMs without any emitters. Instead, with  $\mu$  perpendicular to the mirror (bottom), the spectra show two split peaks ( $\omega_+$  and  $\omega_-$ ) from the strong interaction between emitters and plasmon. I contrast three types of samples. Without dye (Fig. 7.3b, top), a consistent gap plasmon ( $\omega_p$ ) at  $660 \pm 10$  nm is seen. Small fluctuations in peak wavelength are associated with  $\pm 5$  nm variations in nanoparticle size. When this NPoM is partially filled with MB inside the CB[7], two peaks at 610 and 750 nm are seen either side of the absorption peak of MB at  $\omega_0$  (Fig. 7.3b, bottom), corresponding to formation of hybrid plasmon-exciton ( $\omega_{\pm}$ ) branches,  $\omega_{\pm} = \omega_0 \pm \Omega_R/2$ . This yields a Rabi frequency  $\Omega_R = 380$  meV, confirmed by full 3D finite-difference time-domain (FDTD) simulations. Unlike studies [81, 95] that show significant variations in  $\omega_{\pm}$ , I obtain highly consistent results with no spectral wandering observed on individual NPoMs. With dye molecules perpendicular to the plasmon field (without CBs), only a gap-plasmon is seen. Molecules of MB self-assembling on Au orient flat to the surface, due to  $\pi$ -stacking interactions between the conjugated phenyl rings and the metal film [200]. Such controlled studies are essential to prove molecular coupling to the gap plasmon.

To map the dispersion curve, I combine scattering spectra from different-sized nanoparticles plotted according to their detuning from the absorption (exciton) resonance. Simulations from 40-60 nm nanoparticles in NPoMs show gap plasmons tuning across the exciton. A simple coupled-oscillator model matches the quantum mechanical Jaynes-Cummings picture (Ch. 2.8 and Eq. 2.18) [56],

$$\omega_{\pm} = (1/2)(\omega_c + \omega_e) \pm (1/2)\sqrt{(\Omega_R^2 + \delta^2)} \quad (7.1)$$

with plasmon and exciton resonance energies  $\omega_c$  and  $\omega_e$ , and detuning  $\delta = \omega_c - \omega_e$ . Extracting  $\omega_{\pm}$  from the scattering spectra allows  $\omega_c$  to be calculated (knowing  $\omega_e$  which does not show any spectral wandering). This fitting reveals typical anticrossing behaviour (Fig. 7.3c) with  $\Omega_R = 305 \pm 8$  meV at  $\delta = 0$ . I find  $2g/\gamma_c \sim 5$ , far into the strong coupling regime. A key figure of merit is the Purcell factor  $F_P \propto Q/V_m$  characterizing different cavity systems (Fig. 7.1a). For these plasmonic nanocavities  $F_P \sim 3.5 \times 10^6$ , over an order of magnitude larger than state of the art photonic crystal cavities [58] which have reached  $10^5$ , while state-of-the-art planar micropillars [12, 57] attain  $3 \times 10^5$ . The ultralow cavity volume arises here because field penetration into the gold is strongly reduced for such nanometre gaps, as discussed in Chapter 4. Such Purcell factors imply photon emission times below 100 fs, seen as the  $\hbar/\Omega_R \sim 30$  fs Rabi flipping, but unfeasibly short to measure directly.

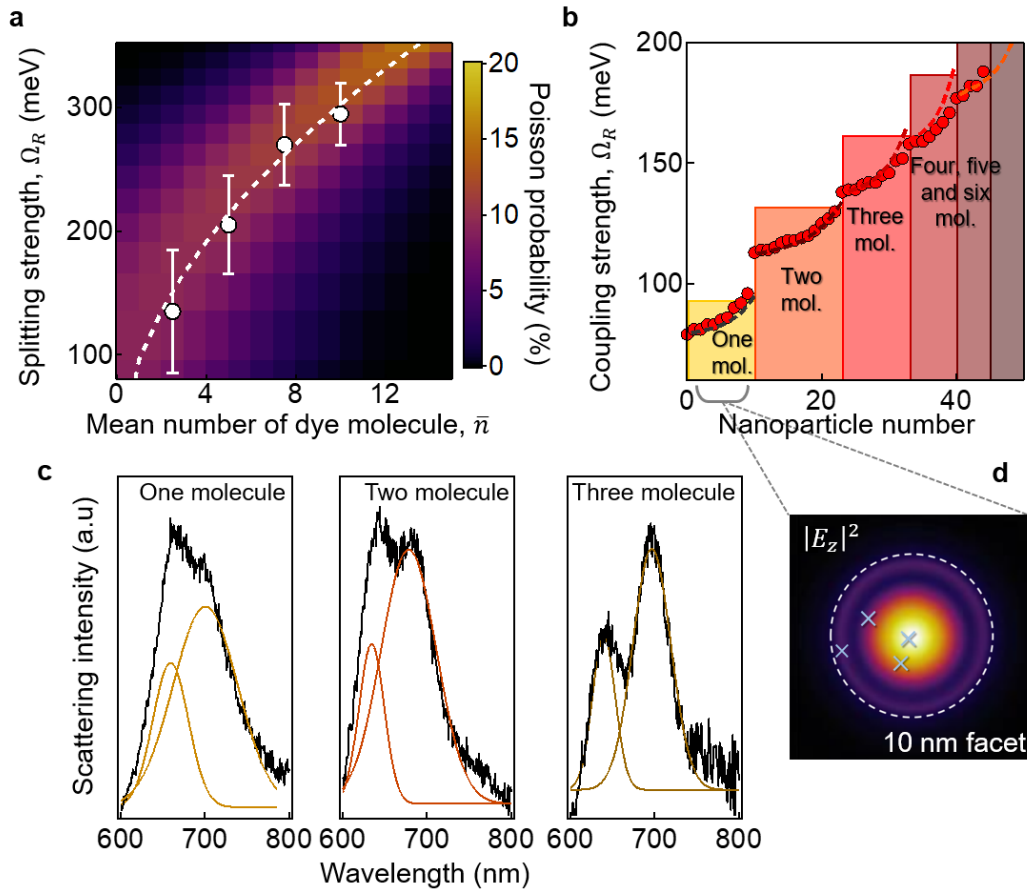


Figure 7.4: **Rabi splitting from few molecules.** (a) Energy of Rabi oscillations ( $g$ ) vs mean number of MB molecules ( $\bar{n}$ ). Experimental (white) points with range of measured coupling strengths (error bars) and theoretical curve (dashed), colours represent expectation from Poisson probability distribution of  $n$ . (b) Coupling strength extracted from different NPoMs in sample of  $\bar{n} = 2.5$ . Theoretical coupling strength in perfect model (shaded bars) and random placement model (dashed lines). (c) Scattering spectra for one, two and three molecules corresponding to (b), with fits. (d) In-plane vertical field distribution in the middle of the gap, 10nm facet marked as white dashed (random position of molecule are marked with  $\times$ ).

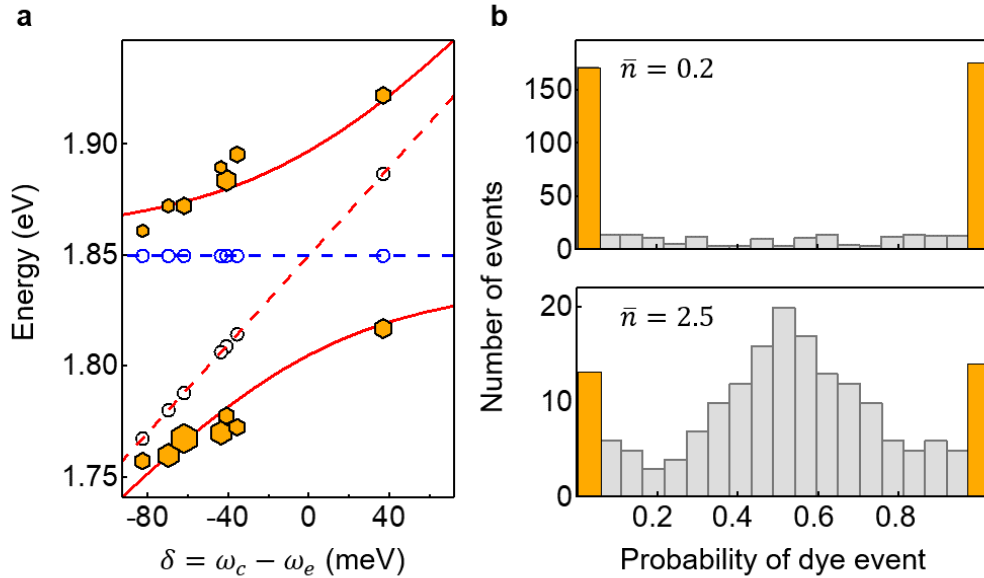


Figure 7.5: **Single-molecule strong coupling** (a) Anti-crossing obtained from single-molecule events, by isolating the data from Fig. 7.4b. (b) Single-molecule probability histograms for  $\bar{n}=0.2$  and 2.5, derived from modified principal-component analysis (Ch.5)

## 7.4 Single-molecule strong coupling

To probe single-molecule strong coupling, I systematically decrease the number of MB molecules by reducing the ratio of MB:CB[7]. Previous studies and simple area estimates imply  $\sim 100$  CB[7] molecules lie inside each nanocavity (Ch.3). With an initial 1:10 molar ratio of MB:CB[7] the mean number of MB molecules within each mode volume is thus  $\bar{n}=10$ . I explore many plasmonic nanocavities with this mean dye number or less (Fig. 7.4a). From the resulting spectra, I extract coupling strengths at different mean MB molecule numbers  $\bar{n}$ , and plot these along with the predicted coupling strength,

$$g_n = \mu \sqrt{(4\pi\hbar c / (\epsilon\epsilon_0 V_m))} \sqrt{\bar{n}} \quad (7.2)$$

where  $\mu=3.8D$  is the transition dipole moment of isolated MB molecules [110]. The probability of finding each coupling strength (Fig 7.4a, colour map) follows the Poisson distribution for  $n$  molecules under each nanoparticle. The range of Rabi splittings seen for  $\bar{n} = 2.5$  that exceed thermal- and cavity-loss rates at room temperature, are consistent

with this plasmonic nanocavity supporting single molecule strong coupling. Reassuringly the range of Rabi frequencies observed increases as the molecular concentration is reduced, as expected since  $\Delta g(\bar{n}) \propto \sqrt{(\bar{n} + \bar{n}^{1/2})} - \sqrt{(\bar{n} - \bar{n}^{1/2})}$  similarly increases as observed in Fig 7.4a colour map.

Direct proof of single-molecule strong coupling is seen from the coupling strengths extracted from the lowest density samples ( $\bar{n}=2.5$ ) which show distinct systematic jumps matching the expected increase of  $g_n$  from  $n=1-3$  molecules (Fig. 7.4b, NPoMs sorted by increasing Rabi splitting). The range in each  $g_n$  arises because single molecules are located at different lateral positions within the gap plasmon, thus coupling with different strengths (predictions shown as dashed lines). Molecules randomly located at the centre of the nanoparticle facet exhibit maximum  $g$ , as the molecule displaced from the centre experience weaker field enhancement and lower  $g$  (Fig. 7.4d). Experimentally, I find excellent agreement (with no fitting parameters) showing that a single MB molecule in these nanocavities gives 80-95 meV Rabi splittings. Further, I plot the scattering spectrum from  $n=1-3$  molecules exhibiting clear increases in coupling strength (Fig. 7.4c). Additional proof of the single-molecule strong coupling is seen from the anti-crossing of plasmon and exciton modes for the subset with  $n=1$  (Fig. 7.5a).

Fluorescence emitted by weakly coupled single-molecules should follow the Purcell factor [61–63]. However, such measurements fail here in the strong coupling regime, because resonantly pumping the molecular absorption also generates strong surface-enhanced resonant Raman scattering (SERRS) consisting of sharp lines with a strong background, that cannot be uniquely separated from photoluminescence. This also obscures  $g^{(2)}$  measurements typically used to confirm single-photon emission from individual chromophores. Here I find extremely strong emission even though the dye molecules are within 0.5 nm of absorptive gold [201], due to the high radiative efficiency of our nanocavities. I harvest these strong SERS peaks to construct ‘chemical’  $g_{ch}^{(2)}$  by using the well-established bianalyte technique with a second near-identical but distinguishable molecule to prove single-molecule statistics (Chapter 5). As evident, at the lowest concentrations two molecules are almost never found at the same time, and we are truly in the single-molecule regime (Fig. 7.5b). Although this does not guarantee direct correlation with single-molecule strong coupling situations, it proves the statistical probability of single-molecules at this concentration. Convincing proof of single-molecules is also seen from the spectral diffusion of vibrational lines in time-series SERRS scans from nanoparticles exhibiting single-molecule strong coupling (Ch. 5.4).

## **7.5 Conclusion**

I have succeeded in combining the gap plasmon with oriented host-guest chemistry in aqueous solution to create enormous numbers of strongly coupled, few-molecule nanocavities at room temperature, in ambient conditions, and which are optically addressable. I expect numerous applications in many fields, including ultra-fast single photon emitters, photon blockade [193], quantum chemistry [202–204], nonlinear optics, and molecular reactions.





## 8 Conclusion and Outlook

In conclusion, this thesis explored the coupling of single-molecules with light confined in a nanoscale optical cavity. These nanocavities are self-assembled by precisely incorporating the molecules of interest in plasmonic nanogaps, which are formed by the coupling between a nanoparticle and a planar metallic surface (NPoM). By utilizing supramolecular guest molecules and DNA origami breadboards, different optical and chemical components are pinned together in plasmonic gaps to study the effect of orientation and position of the molecule in the gap for optimized coupling with the cavity mode.

Light emission from molecules is enhanced in plasmonic cavities with gaps of  $<5$  nm. This radiative enhancement is used to map the confined optical fields by precisely changing the lateral position of single-molecules in the gap using DNA origami. The strength of the coupling ( $\Omega_R$ ) at an optical field maxima in this system is measured to be  $\sim 80$  meV smaller than the NPoM cavity ( $\gamma_c$ ) and molecular ( $\gamma_e$ ) losses. However, the coupling strength is large enough to perturb the light scattering by the NPoM cavity and this modification is monitored by bleaching the molecule.

The coupling strength is further enhanced by decreasing the gaps to  $<1$  nm and orientating the molecular dipoles along the optical field polarization, reaching the strong coupling regime ( $\Omega_R > \gamma_c, \gamma_e$ ) where light and molecular modes are indistinguishable. The non-linear scaling of  $\Omega_R \propto \sqrt{n}$  is measured by systematically varying the number of molecules in the gap,  $n$  from 1-10.

Having studied these effects, there are certain limitations:

- ⇒ The NPoM cavity is not a flexible substrate and hence it can not be easily integrated with biological systems for in-vivo studies.

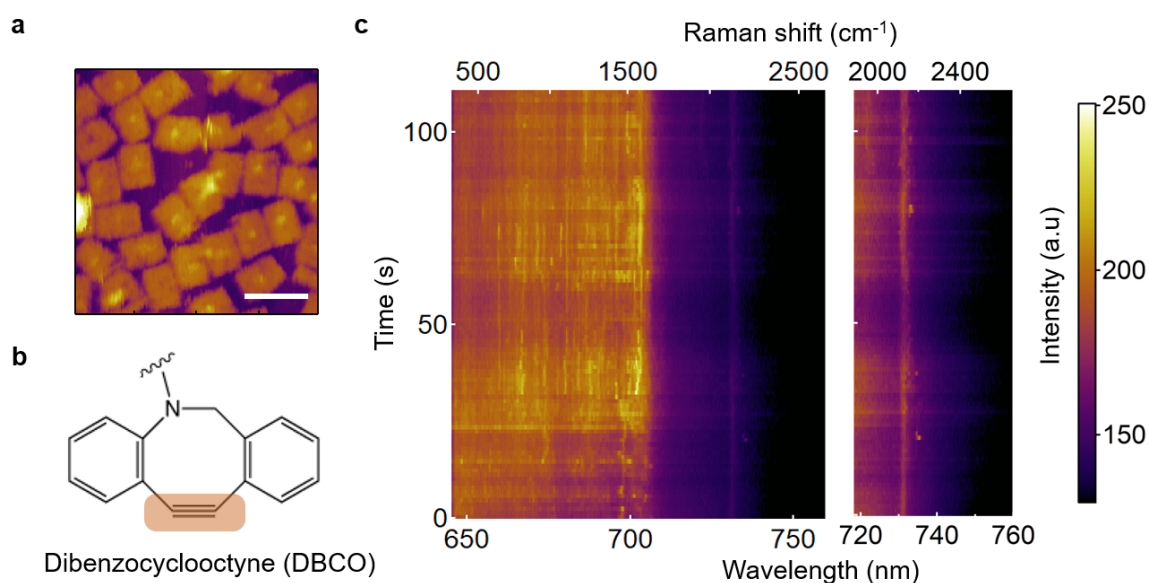


Figure 8.1: **SERS of a single C≡C bond.** (a) AFM image of DNAo tiles used to position a single-dibenzyloctyne (DBCO) molecule in the nanogaps of NPoM cavity. (b) Chemical structure of DBCO molecule, C≡C bond highlighted with orange box. (c) Time resolved SERS spectra of assembled single-DBCO molecule in the NPoM cavity. The Raman mode of C≡C bond in the region of  $2150\text{ cm}^{-1}$  enlarged on the right.

- ⇒ The small optical mode volume of NPoM cavities results in coupling with only a few emitters ( $<100$ ) which is not favourable for applications such as lasing and large scale chemical reactions.
- ⇒ Optical pumping of plasmonic cavities is significantly different from dielectric cavities. Ultrafast decay rates hamper climbing the JC ladder.
- ⇒ Pumping the NPoM cavity with high intensities results in deformation of the cavity due to the mobility of atoms on the surface.

Despite of all these limitations, light-molecule coupling in plasmonic cavities provide promising outlook for the following applications:

#### **Bright single-photon emission with high repetition rate:**

Single emitters (quantum dots, N-V centres or 2D-TMD defects) coupled to NPoM cavities can act as efficient systems for reliable single-photon sources. The rate of single-photon emission can be enhanced at least by a factor of  $10^4$  before reaching the strong coupling regime. This opens a promising route for the spectroscopy of other single-photon emitting systems and for quantum information processes [205, 206].

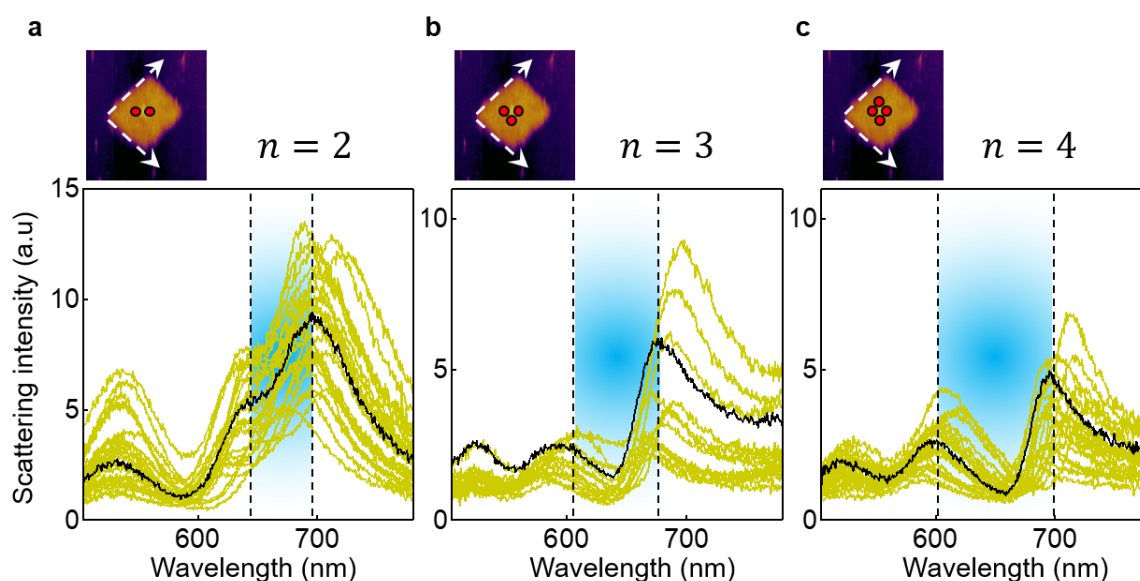


Figure 8.2: **Strong coupling from deterministic number of Cy-5 molecules.** (a-c) Scattering spectra from individual NPoM with (a) two, (b) three, and (c) four Cy-5 molecules resonantly coupled to the NPoM cavity. The molecules programmed to assemble in a square lattice with an edge length of 5 nm with each vertex point occupied by a single Cy-5 molecule, schematically shown on top.

### Making of single-molecule optical switches:

Certain sets of organic molecules undergo photo-isomerization resulting in a change in their resonance energy. These systems can be coupled with the resonance of a NPoM cavity and the scattering of the system can be modulated by changing the isomer form of the molecule. The energy required for such a switch can be as low as zJ with a switching rate of picoseconds.

### Optomechanics of a single-vibrational bond:

The vibrations of a single-chemical bond can be monitored in SERS spectra by precisely positioning the molecule in the NPoM gaps. In DNA origami spacers specifically, molecules with  $C\equiv C$  are tagged and a unique high energy Raman band at  $\sim 2150\text{ cm}^{-1}$  is identified (Fig. 8.1). This enables to study the effect of intense electric fields at the level of single-bond vibrations.

### Optical mixing of different molecules and energy transfer:

Transition from a weak- to strong-coupled system is achieved by increasing the number of Cy-5 molecules in the gap (Fig. 8.2). Energy transfer across spatially separated molecules

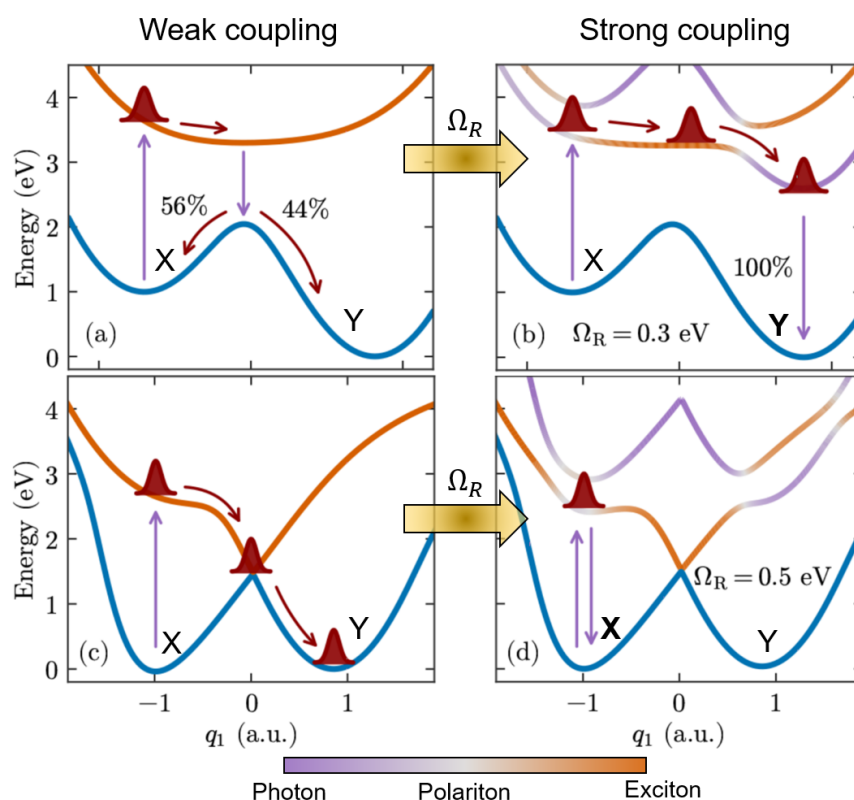


Figure 8.3: **Polaritonic potential energy surfaces (PES) of two model molecules that undergo transition between X and Y configurations in weak and strong coupling.** (a,c) Bare molecules with no light-matter interaction. (b) Strongly coupled molecules with  $\Omega_R=0.3$  eV and  $\Omega_R=0.5$  eV. The colour of polariton PES represents the photonic fraction of the state from purely excitonic (orange) through polaritonic (light grey) to purely photonic (purple). Reproduced from [207].

can be studied by systematically increasing the number of molecules at deterministic locations in the gap. Further, optically mixed states of different molecules can be achieved by resonantly mixing their energies with the cavity fields.

### Strong coupling for organic chemistry:

Excited state reactions of the molecules change, when the energy states of the molecules are strongly mixed with optical states of the cavity. Changes in the chemical dynamics can arise from the hybridized states that persist even at zero photon population in the cavity ( $g \propto \sqrt{1+N_{Ph}}$ ;  $N_{Ph}$  is the number of photons in the cavity). This has a great potential in pharmaceutical applications where the molecular stability needs to be enhanced. Recent theoretical studies [207–209] demonstrated the effect of strong coupling on stabilizing specific isomer forms of certain molecule (Fig. 8.3). It is worth putting efforts in making

---

cavities with resonances in UV (100-400nm), where the resonances of small organic molecules lie.

To conclude, plasmonic cavities have opened the new avenues of quantum manipulation of light-molecule coupling at room temperature. The NPoM cavities with large radiative components facilitate enhanced light extraction. The strong field confinement results in strong optical feedback with coherent coupling from single-molecules. A system encompassing both these functionalities will have promising implications in quantum information and quantum photochemistry.



# Bibliography

- [1] Y. Kaluzny, P. Goy, M. Gross, J. M. Raimond, and S. Haroche. Observation of Self-Induced Rabi Oscillations in Two-Level Atoms Excited Inside a Resonant Cavity: The Ringing Regime of Superradiance. *Physical Review Letters*, 51(13):1175–1178, September 1983.
- [2] M. G. Raizen, R. J. Thompson, R. J. Brecha, H. J. Kimble, and H. J. Carmichael. Normal-mode splitting and linewidth averaging for two-state atoms in an optical cavity. *Physical Review Letters*, 63(3):240–243, July 1989.
- [3] R. J. Thompson, G. Rempe, and H. J. Kimble. Observation of normal-mode splitting for an atom in an optical cavity. *Physical Review Letters*, 68(8):1132–1135, February 1992.
- [4] Serge Haroche. Nobel Lecture: Controlling photons in a box and exploring the quantum to classical boundary. *Reviews of Modern Physics*, 85(3):1083–1102, July 2013.
- [5] Daniel C. Harris and Michael D. Bertolucci. *Symmetry and Spectroscopy: An Introduction to Vibrational and Electronic Spectroscopy (Dover Books on Chemistry)*. Dover Publications, 1989.
- [6] Joseph R. Lakowicz. *Principles of Fluorescence Spectroscopy*. Springer, 2011.
- [7] G. Zumofen, N. M. Mojarad, V. Sandoghdar, and M. Agio. Perfect Reflection of Light by an Oscillating Dipole. *Physical Review Letters*, 101(18):180404, October 2008.
- [8] A. Ghanadzadeh Gilani, M. Salmanpour, and T. Ghorbanpour. Solvatochromism, dichroism and excited state dipole moment of azure A and methylene blue. *Journal of Molecular Liquids*, 179:118–123, March 2013.
- [9] Anu Bamgbelu, Jing Wang, and Jerzy Leszczynski. TDDFT study of the optical properties of Cy5 and its derivatives. *The Journal of Physical Chemistry A*,

- 114(10):3551–3555, 2010.
- [10] T Kobayashi. *J-Aggregates*. World Scientific, October 1996.
- [11] W. William Yu, Lianhua Qu, Wenzhuo Guo, and Xiaogang Peng. Experimental Determination of the Extinction Coefficient of CdTe, CdSe, and CdS Nanocrystals. *Chemistry of Materials*, 15(14):2854–2860, July 2003.
- [12] G. Khitrova, H. M. Gibbs, M. Kira, S. W. Koch, and A. Scherer. Vacuum Rabi splitting in semiconductors. *Nature Physics*, 2(2):81–90, February 2006.
- [13] Hualing Zeng and Xiaodong Cui. An optical spectroscopic study on two-dimensional group-VI transition metal dichalcogenides. *Chemical Society Reviews*, 44(9):2629–2642, April 2015.
- [14] Malte Selig, Gunnar Berghäuser, Archana Raja, Philipp Nagler, Christian Schuller, Tony F Heinz, Tobias Korn, Alexey Chernikov, Ermin Malic, and Andreas Knorr. Excitonic linewidth and coherence lifetime in monolayer transition metal dichalcogenides. *Nature communications*, 7:13279, 2016.
- [15] Robert C. Hilborn. Einstein coefficients, cross sections, f values, dipole moments, and all that. *American Journal of Physics*, 50(11):982–986, November 1982.
- [16] K. G. Lee, X. W. Chen, H. Eghlidi, P. Kukura, R. Lettow, A. Renn, V. Sandoghdar, and S. Gotzinger. A planar dielectric antenna for directional single-photon emission and near-unity collection efficiency. *Nature Photonics*, 5(3):166–169, March 2011.
- [17] T. H. Taminiau, F. D. Stefani, F. B. Segerink, and N. F. van Hulst. Optical antennas direct single-molecule emission. *Nature Photonics*, 2(4):234–237, April 2008.
- [18] Peter Lodahl, A. Floris van Driel, Ivan S. Nikolaev, Arie Irman, Karin Overgaag, Daniel Vanmaekelbergh, and Willem L. Vos. Controlling the dynamics of spontaneous emission from quantum dots by photonic crystals. *Nature*, 430(7000):654–657, August 2004.
- [19] Dirk Englund, David Fattal, Edo Waks, Glenn Solomon, Bingyang Zhang, Toshihiro Nakaoka, Yasuhiko Arakawa, Yoshihisa Yamamoto, and Jelena Vuckovic. Controlling the Spontaneous Emission Rate of Single Quantum Dots in a Two-Dimensional Photonic Crystal. *Physical Review Letters*, 95(1):013904, July 2005.
- [20] Matthew Pelton, Charles Santori, Jelena Vuckovic, Bingyang Zhang, Glenn S. Solomon, Jocelyn Plant, and Yoshihisa Yamamoto. Efficient Source of Single Photons: A Single Quantum Dot in a Micropost Microcavity. *Physical Review*



- Letters*, 89(23):233602, November 2002.
- [21] Matthew Pelton. Modified spontaneous emission in nanophotonic structures. *Nature Photonics*, 9(7):427–435, July 2015.
- [22] Jon A. Schuller, Edward S. Barnard, Wenshan Cai, Young Chul Jun, Justin S. White, and Mark L. Brongersma. Plasmonics for extreme light concentration and manipulation. *Nature Materials*, 9(3):193–204, March 2010.
- [23] Lukas Novotny and Niek van Hulst. Antennas for light. *Nature Photonics*, 5(2):83–90, February 2011.
- [24] Stefan Alexander Maier. *Plasmonics: Fundamentals and Applications*. Springer, 2007.
- [25] P. B. Johnson and R. W. Christy. Optical Constants of the Noble Metals. *Physical Review B*, 6(12):4370–4379, December 1972.
- [26] Edward D. Palik. *Handbook of Optical Constants of Solids*. Academic Press, 1998.
- [27] A. Huber, N. Ocelic, D. Kazantsev, and R. Hillenbrand. Near-field imaging of mid-infrared surface phonon polariton propagation. *Applied Physics Letters*, 87(8):081103, August 2005.
- [28] Martin J Gentile, S Núñez-Sánchez, and William L Barnes. Optical field-enhancement and subwavelength field-confinement using excitonic nanostructures. 2014.
- [29] Mark L. Brongersma, Yi Cui, and Shanhui Fan. Light management for photovoltaics using high-index nanostructures. *Nature Materials*, 13(5):451–460, May 2014.
- [30] E Kretschmann and H Raether. Radiative decay of nonradiative surface plasmons excited by light. *Z. Naturforsch. A*, 23:2135, 1968.
- [31] William L Barnes. Surface plasmon–polariton length scales: a route to sub-wavelength optics. *Journal of optics A: pure and applied optics*, 8(4):S87, 2006.
- [32] Alyson V Whitney, Jeffrey W Elam, Shengli Zou, Alex V Zinovev, Peter C Stair, George C Schatz, and Richard P Van Duyne. Localized surface plasmon resonance nanosensor: a high-resolution distance-dependence study using atomic layer deposition. *The Journal of Physical Chemistry B*, 109(43):20522–20528, 2005.
- [33] Philip Trøst Kristensen, Cole Van Vlack, and Stephen Hughes. Generalized effective mode volume for leaky optical cavities. *Optics letters*, 37(10):1649–1651, 2012.

- [34] Philip Trøst Kristensen and Stephen Hughes. Modes and mode volumes of leaky optical cavities and plasmonic nanoresonators. *arXiv preprint arXiv:1312.5769*, 2013.
- [35] Huigao Duan, Antonio I. Fernandez-Dominguez, Michel Bosman, Stefan A. Maier, and Joel K. W. Yang. Nanoplasmonics: Classical down to the Nanometer Scale. *Nano Letters*, 12(3):1683–1689, March 2012.
- [36] Daniel R. Ward, David A. Corley, James M. Tour, and Douglas Natelson. Vibrational and electronic heating in nanoscale junctions. *Nature Nanotechnology*, 6(1):33–38, January 2011.
- [37] Kevin J. Savage, Matthew M. Hawkeye, Ruben Esteban, Andrei G. Borisov, Javier Aizpurua, and Jeremy J. Baumberg. Revealing the quantum regime in tunnelling plasmonics. *Nature*, 491(7425):574–577, November 2012.
- [38] Lin Cheng, Jibin Song, Jun Yin, and Hongwei Duan. Self-Assembled Plasmonic Dimers of Amphiphilic Gold Nanocrystals. *The Journal of Physical Chemistry Letters*, 2(17):2258–2262, September 2011.
- [39] Gang Chen, Yong Wang, Li Huey Tan, Miaoxin Yang, Lee Siew Tan, Yuan Chen, and Hongyu Chen. High-Purity Separation of Gold Nanoparticle Dimers and Trimers. *Journal of the American Chemical Society*, 131(12):4218–4219, 2009.
- [40] C. Sauvan, J. P. Hugonin, I. S. Maksymov, and P. Lalanne. Theory of the Spontaneous Optical Emission of Nanosize Photonic and Plasmon Resonators. *Physical Review Letters*, 110(23):237401, June 2013.
- [41] A Femius Koenderink. On the use of purcell factors for plasmon antennas. *Optics letters*, 35(24):4208–4210, 2010.
- [42] R Ruppin. Electromagnetic energy density in a dispersive and absorptive material. *Physics letters A*, 299(2):309–312, 2002.
- [43] EA Muljarov and Wolfgang Langbein. Exact mode volume and purcell factor of open optical systems. *Physical Review B*, 94(23):235438, 2016.
- [44] Tigran V Shahbazyan. Mode volume, energy transfer, and spaser threshold in plasmonic systems with gain. *ACS Photonics*, 4(4):1003–1008, 2017.
- [45] Jung-Hoon Lee, Jwa-Min Nam, Ki-Seok Jeon, Dong-Kwon Lim, Hyoki Kim, Sung-hoon Kwon, Haemi Lee, and Yung Doug Suh. Tuning and Maximizing the Single-Molecule Surface-Enhanced Raman Scattering from DNA-Tethered Nanodumbbells. *ACS Nano*, 6(11):9574–9584, November 2012.

- [46] P. K. Aravind and Horia Metiu. The effects of the interaction between resonances in the electromagnetic response of a sphere-plane structure; applications to surface enhanced spectroscopy. *Surface Science*, 124(2):506–528, January 1983.
- [47] P. K. Aravind and Horia Metiu. Use of a perfectly conducting sphere to excite the plasmon of a flat surface. 1. Calculation of the local field with applications to surface-enhanced spectroscopy. *The Journal of Physical Chemistry*, 86(26):5076–5084, December 1982.
- [48] P. Nordlander, C. Oubre, E. Prodan, K. Li, and M. I. Stockman. Plasmon Hybridization in Nanoparticle Dimers. *Nano Letters*, 4(5):899–903, 2004.
- [49] C. Tserkezis, R. Esteban, D. O. Sigle, J. Mertens, L. O. Herrmann, J. J. Baumberg, and J. Aizpurua. Hybridization of plasmonic antenna and cavity modes: Extreme optics of nanoparticle-on-mirror nanogaps. *Physical Review A*, 92(5):053811, November 2015.
- [50] C Ciraci, RT Hill, JJ Mock, Y Urzhumov, AI Fernández-Domínguez, SA Maier, JB Pendry, A Chilkoti, and DR Smith. Probing the ultimate limits of plasmonic enhancement. *Science*, 337(6098):1072–1074, 2012.
- [51] Bart de Nijs, Richard W Bowman, Lars O Herrmann, Felix Benz, Steve J Barrow, Jan Mertens, Daniel O Sigle, Rohit Chikkaraddy, Anna Eiden, Andrea Ferrari, et al. Unfolding the contents of sub-nm plasmonic gaps using normalising plasmon resonance spectroscopy. *Faraday discussions*, 178:185–193, 2015.
- [52] Ryan T Hill, Jack J Mock, Angus Hucknall, Scott D Wolter, Nan M Jokerst, David R Smith, and Ashutosh Chilkoti. Plasmon ruler with angstrom length resolution. *ACS nano*, 6(10):9237–9246, 2012.
- [53] Benjamin Gallinet, Thomas Siegfried, Hans Sigg, Peter Nordlander, and Olivier JF Martin. Plasmonic radiance: probing structure at the ångstrom scale with visible light. *Nano letters*, 13(2):497–503, 2013.
- [54] Felix Benz, Rohit Chikkaraddy, Andrew Salmon, Hamid Ohadi, Bart de Nijs, Jan Mertens, Cloudy Carnegie, Richard W. Bowman, and Jeremy J. Baumberg. SERS of Individual Nanoparticles on a Mirror: Size Does Matter, but so Does Shape. *The Journal of Physical Chemistry Letters*, 7(12):2264–2269, June 2016.
- [55] Daniel O. Sigle, Jan Mertens, Lars O. Herrmann, Richard W. Bowman, Sandrine Ithurria, Benoit Dubertret, Yumeng Shi, Hui Ying Yang, Christos Tserkezis, Javier

- Aizpurua, and Jeremy J. Baumberg. Monitoring Morphological Changes in 2d Monolayer Semiconductors Using Atom-Thick Plasmonic Nanocavities. *ACS Nano*, 9(1):825–830, January 2015.
- [56] P. Torma and W. L. Barnes. Strong coupling between surface plasmon polaritons and emitters: a review. *Reports on Progress in Physics*, 78(1):013901, January 2015.
- [57] Kerry J. Vahala. Optical microcavities. *Nature*, 424(6950):839–846, August 2003.
- [58] T. Yoshie, A. Scherer, J. Hendrickson, G. Khitrova, H. M. Gibbs, G. Rupper, C. Ell, O. B. Shchekin, and D. G. Deppe. Vacuum Rabi splitting with a single quantum dot in a photonic crystal nanocavity. *Nature*, 432(7014):200–203, November 2004.
- [59] Nuttawut Kongsuwan, Angela Demetriadou, Rohit Chikkaraddy, Felix Benz, Vladimir A. Turek, Ulrich F. Keyser, Jeremy J. Baumberg, and Ortwin Hess. Suppressed Quenching and Strong Coupling of Purcell-Enhanced Single-Molecule Emission in Plasmonic Nanocavities. *arXiv:1612.02611 [physics]*, December 2016. arXiv: 1612.02611.
- [60] Edward Mills Purcell. Spontaneous emission probabilities at radio frequencies. *Physical Review*, 69(11-12):681, June 1946.
- [61] Pascal Anger, Palash Bharadwaj, and Lukas Novotny. Enhancement and Quenching of Single-Molecule Fluorescence. *Physical Review Letters*, 96(11):113002, March 2006.
- [62] Anika Kinkhabwala, Zongfu Yu, Shanhui Fan, Yuri Avlasevich, Klaus Mullen, and W. E. Moerner. Large single-molecule fluorescence enhancements produced by a bowtie nanoantenna. *Nature Photonics*, 3(11):654–657, November 2009.
- [63] Gleb M Akselrod, Christos Argyropoulos, Thang B Hoang, Cristian Ciraci, Chao Fang, Jiani Huang, David R Smith, and Maiken H Mikkelsen. Probing the mechanisms of large purcell enhancement in plasmonic nanoantennas. *Nature Photonics*, 8(11):835–840, 2014.
- [64] A. V. Akimov, A. Mukherjee, C. L. Yu, D. E. Chang, A. S. Zibrov, P. R. Hemmer, H. Park, and M. D. Lukin. Generation of single optical plasmons in metallic nanowires coupled to quantum dots. *Nature*, 450(7168):402–406, November 2007.
- [65] Mark L. Brongersma, Naomi J. Halas, and Peter Nordlander. Plasmon-induced hot carrier science and technology. *Nature Nanotechnology*, 10(1):25–34, January 2015.

- [66] Remi Faggiani, Jianji Yang, and Philippe Lalanne. Quenching, Plasmonic, and Radiative Decays in Nanogap Emitting Devices. *ACS Photonics*, 2(12):1739–1744, December 2015.
- [67] Jianji Yang, Remi Faggiani, and Philippe Lalanne. Light emission in nanogaps: overcoming quenching. *Nanoscale Horizons*, 1(1):11–13, 2016.
- [68] M Ringler, A Schwemer, M Wunderlich, A Nichtl, K Kürzinger, TA Klar, and J Feldmann. Shaping emission spectra of fluorescent molecules with single plasmonic nanoresonators. *Physical review letters*, 100(20):203002, 2008.
- [69] Kasey J. Russell, Tsung-Li Liu, Shanying Cui, and Evelyn L. Hu. Large spontaneous emission enhancement in plasmonic nanocavities. *Nature Photonics*, 6(7):459–462, July 2012.
- [70] Alec Rose, Thang B Hoang, Felicia McGuire, Jack J Mock, Cristian Ciraci, David R Smith, and Maiken H Mikkelsen. Control of radiative processes using tunable plasmonic nanopatch antennas. *Nano letters*, 14(8):4797–4802, 2014.
- [71] Sergei Kuhn, Ulf Hakanson, Lavinia Rogobete, and Vahid Sandoghdar. Enhancement of Single-Molecule Fluorescence Using a Gold Nanoparticle as an Optical Nanoantenna. *Physical Review Letters*, 97(1):017402, July 2006.
- [72] Jérôme Wenger, Davy Gérard, José Dintinger, Oussama Mahboub, Nicolas Bonod, Evgeny Popov, Thomas W Ebbesen, and Hervé Rigneault. Emission and excitation contributions to enhanced single molecule fluorescence by gold nanometric apertures. *Optics Express*, 16(5):3008–3020, 2008.
- [73] Hu Cang, Yongmin Liu, Yuan Wang, Xiaobo Yin, and Xiang Zhang. Giant Suppression of Photobleaching for Single Molecule Detection via the Purcell Effect. *Nano Letters*, 13(12):5949–5953, December 2013.
- [74] Thang B. Hoang, Gleb M. Akselrod, and Maiken H. Mikkelsen. Ultrafast Room-Temperature Single Photon Emission from Quantum Dots Coupled to Plasmonic Nanocavities. *Nano Letters*, 16(1):270–275, January 2016.
- [75] Thang B. Hoang, Gleb M. Akselrod, Christos Argyropoulos, Jiani Huang, David R. Smith, and Maiken H. Mikkelsen. Ultrafast spontaneous emission source using plasmonic nanoantennas. *Nature Communications*, 6, July 2015.
- [76] M. S. Tame, K. R. McEnery, K. Ozdemir, J. Lee, S. A. Maier, and M. S. Kim. Quantum plasmonics. *Nature Physics*, 9(6):329–340, June 2013.

- [77] Kevin M Birnbaum, Andreea Boca, Russell Miller, Allen D Boozer, Tracy E Northup, and H Jeff Kimble. Photon blockade in an optical cavity with one trapped atom. *Nature*, 436(7047):87–90, 2005.
- [78] JM Fink, M Göppl, M Baur, R Bianchetti, PJ Leek, Alexandre Blais, and Andreas Wallraff. Climbing the jaynes–cummings ladder and observing its nonlinearity in a cavity qed system. *Nature*, 454(7202):315–318, 2008.
- [79] Jacek Kasprzak, S Reitzenstein, Egor A Muljarov, C Kistner, C Schneider, M Strauss, S Höfling, A Forchel, and W Langbein. Up on the jaynes-cummings ladder of a quantum-dot/microcavity system. *Nature materials*, 9(4):304–308, 2010.
- [80] Andrea E. Schlather, Nicolas Large, Alexander S. Urban, Peter Nordlander, and Naomi J. Halas. Near-Field Mediated Plexcitonic Coupling and Giant Rabi Splitting in Individual Metallic Dimers. *Nano Letters*, 13(7):3281–3286, 2013.
- [81] Gulis Zengin, Martin Wersall, Sara Nilsson, Tomasz J. Antosiewicz, Mikael Kall, and Timur Shegai. Realizing Strong Light-Matter Interactions between Single-Nanoparticle Plasmons and Molecular Excitons at Ambient Conditions. *Physical Review Letters*, 114(15):157401, April 2015.
- [82] Yao Zhang, Qiu-Shi Meng, Li Zhang, Yang Luo, Yun-Jie Yu, Ben Yang, Yang Zhang, Ruben Esteban, Javier Aizpurua, Yi Luo, et al. Sub-nanometre control of the coherent interaction between a single molecule and a plasmonic nanocavity. *Nature Communications*, 8, 2017.
- [83] Kotni Santhosh, Ora Bitton, Lev Chuntonov, and Gilad Haran. Vacuum rabi splitting in a plasmonic cavity at the single quantum emitter limit. *Nature communications*, 7, 2016.
- [84] Y. Sugawara, T. A. Kelf, J. J. Baumberg, M. E Abdelsalam, and P. N. Bartlett. Strong Coupling between Localized Plasmons and Organic Excitons in Metal Nanovoids. *Physical Review Letters*, 97(26):266808, December 2006.
- [85] Tobias Ambjornsson, Gautam Mukhopadhyay, S. Peter Apell, and Mikael Kall. Resonant coupling between localized plasmons and anisotropic molecular coatings in ellipsoidal metal nanoparticles. *Physical Review B*, 73(8):085412, February 2006.
- [86] T. K. Hakala, J. J. Toppari, A. Kuzyk, M. Pettersson, H. Tikkanen, H. Kunttu, and P. Torma. Vacuum Rabi Splitting and Strong-Coupling Dynamics for Surface-Plasmon Polaritons and Rhodamine 6g Molecules. *Physical Review Letters*,

- 103(5):053602, July 2009.
- [87] Fumika Nagasawa, Mai Takase, and Kei Murakoshi. Raman Enhancement via Polariton States Produced by Strong Coupling between a Localized Surface Plasmon and Dye Excitons at Metal Nanogaps. *The Journal of Physical Chemistry Letters*, 5(1):14–19, 2013.
- [88] Federico Valmorra, Markus Broll, Stephan Schwaiger, Nadine Welzel, Detlef Heitmann, and Stefan Mendach. Strong coupling between surface plasmon polariton and laser dye rhodamine 800. *Applied Physics Letters*, 99(5):051110, August 2011.
- [89] Svitlana V. Baieva, Tommi K. Hakala, and Jussi J. Toppari. Strong coupling between surface plasmon polaritons and Sulforhodamine 101 dye. *Nanoscale Research Letters*, 7(1):191, March 2012.
- [90] Mikko A. Koponen, Ulrich Hohenester, Tommi K. Hakala, and J. Jussi Toppari. Absence of mutual polariton scattering for strongly coupled surface plasmon polaritons and dye molecules with a large Stokes shift. *Physical Review B*, 88(8):085425, August 2013.
- [91] Svitlana Baieva, JA Ihalainen, and JJ Toppari. Strong coupling between surface plasmon polaritons and  $\beta$ -carotene in nanolayered system. *The Journal of chemical physics*, 138(4):044707, 2013.
- [92] T. Schwartz, J. A. Hutchison, C. Genet, and T. W. Ebbesen. Reversible Switching of Ultrastrong Light-Molecule Coupling. *Physical Review Letters*, 106(19):196405, May 2011.
- [93] Jino George, Shaojun Wang, Thibault Chervy, Antoine Canaguier-Durand, Gael Schaeffer, Jean-Marie Lehn, James A Hutchison, Cyriaque Genet, and Thomas W Ebbesen. Ultra-strong coupling of molecular materials: spectroscopy and dynamics. *Faraday discussions*, 178:281–294, 2015.
- [94] Jeremy Baumberg, Mikhail Noginov, Javier Aizpurua, Kaiqiang Lin, Thomas Ebbesen, Alexei A Kornyshev, Riccardo Sapienza, Niek van Hulst, Santhosh Kotni, F Javier García de Abajo, et al. Quantum plasmonics, gain and spasers: general discussion. *Faraday discussions*, 178:325–334, 2015.
- [95] Gulis Zengin, Goran Johansson, Peter Johansson, Tomasz J. Antosiewicz, Mikael Kall, and Timur Shegai. Approaching the strong coupling limit in single plasmonic nanorods interacting with J-aggregates. *Scientific Reports*, 3, October 2013.

- [96] Nche T. Fofang, Nathaniel K. Grady, Zhiyuan Fan, Alexander O. Govorov, and Naomi J. Halas. Plexciton Dynamics: Exciton–Plasmon Coupling in a J-Aggregate–Au Nanoshell Complex Provides a Mechanism for Nonlinearity. *Nano Letters*, 11(4):1556–1560, 2011.
- [97] W. Andrew Murray, James. R. Suckling, and William L. Barnes. Overlayers on Silver Nanotriangles: Field Confinement and Spectral Position of Localized Surface Plasmon Resonances. *Nano Letters*, 6(8):1772–1777, 2006.
- [98] Martin Wersall, Jorge Cuadra, Tomasz J Antosiewicz, Sinan Balci, and Timur Shegai. Observation of mode splitting in photoluminescence of individual plasmonic nanoparticles strongly coupled to molecular excitons. *Nano letters*, 17(1):551–558, 2016.
- [99] Tomasz J Antosiewicz, S Peter Apell, and Timur Shegai. Plasmon–exciton interactions in a core–shell geometry: from enhanced absorption to strong coupling. *Acs Photonics*, 1(5):454–463, 2014.
- [100] J Christopher Love, Lara A Estroff, Jennah K Kriebel, Ralph G Nuzzo, and George M Whitesides. Self-assembled monolayers of thiolates on metals as a form of nanotechnology. *Chem. rev*, 105(4):1103–1170, 2005.
- [101] Ralph G Nuzzo and David L Allara. Adsorption of bifunctional organic disulfides on gold surfaces. *Journal of the American Chemical Society*, 105(13):4481–4483, 1983.
- [102] WC Bigelow, DL Pickett, and WA Zisman. Oleophobic monolayers: I. films adsorbed from solution in non-polar liquids. *Journal of Colloid Science*, 1(6):513–538, 1946.
- [103] George M Whitesides, Colin D Bain, EB Troughton, Yu-Tai Tao, and Joseph Evall. Formation of monolayer films by the spontaneous assembly of organic thiols from solution onto gold. Technical report, HARVARD UNIV CAMBRIDGE MA DEPT OF CHEMISTRY, 1988.
- [104] A Lio, C Morant, DF Ogletree, and M Salmeron. Atomic force microscopy study of the pressure-dependent structural and frictional properties of n-alkanethiols on gold. *The Journal of Physical Chemistry B*, 101(24):4767–4773, 1997.
- [105] Colin D Bain and George M Whitesides. Molecular-level control over surface order in self-assembled monolayer films of thiols on gold. *Science*, 240(4848):62–64, 1988.
- [106] Daniel K Schwartz. Mechanisms and kinetics of self-assembled monolayer formation. *Annual Review of Physical Chemistry*, 52(1):107–137, 2001.



- [107] Khaleel I Assaf and Werner M Nau. Cucurbiturils: from synthesis to high-affinity binding and catalysis. *Chemical Society Reviews*, 44(2):394–418, 2015.
- [108] Steven J Barrow, Setu Kasera, Matthew J Rowland, Jesus del Barrio, and Oren A Scherman. Cucurbituril-based molecular recognition. *Chem. Rev*, 115(22):12320–12406, 2015.
- [109] Eric Masson, Xiaoxi Ling, Roymon Joseph, Lawrence Kyeremeh-Mensah, and Xiaoyong Lu. Cucurbituril chemistry: a tale of supramolecular success. *Rsc Advances*, 2(4):1213–1247, 2012.
- [110] Kesharsingh Patil, Rajesh Pawar, and Pandurang Talap. Self-aggregation of Methylene Blue in aqueous medium and aqueous solutions of Bu<sub>4</sub>nbr and urea. *Physical Chemistry Chemical Physics*, 2(19):4313–4317, January 2000.
- [111] Apurba L. Koner and Werner M. Nau. Cucurbituril Encapsulation of Fluorescent Dyes. *Supramolecular Chemistry*, 19(1-2):55–66, March 2007.
- [112] Pedro Montes-Navajas, Avelino Corma, and Hermenegildo Garcia. Complexation and Fluorescence of Tricyclic Basic Dyes Encapsulated in Cucurbiturils. *ChemPhysChem*, 9(5):713–720, April 2008.
- [113] Nilotpal Barooah, Jyotirmayee Mohanty, and Achikanath C. Bhasikuttan. Cucurbit[8]uril-templated H and J dimers of bichromophoric coumarin dyes: origin of contrasting emission. *Chemical Communications*, 51(67):13225–13228, 2015.
- [114] Lars O Herrmann, Ventsislav K Valev, Christos Tserkezis, Jonathan S Barnard, Setu Kasera, Oren A Scherman, Javier Aizpurua, and Jeremy J Baumberg. Threading plasmonic nanoparticle strings with light. *Nature communications*, 5, 2014.
- [115] Qi An, Guangtao Li, Chengan Tao, Yan Li, Yiguang Wu, and Weixia Zhang. A general and efficient method to form self-assembled cucurbit[n]uril monolayers on gold surfaces. *Chemical Communications*, 17:1989–1991, April 2008.
- [116] Richard W. Taylor, Tung-Chun Lee, Oren A. Scherman, Ruben Esteban, Javier Aizpurua, Fu Min Huang, Jeremy J. Baumberg, and Sumeet Mahajan. Precise Subnanometer Plasmonic Junctions for SERS within Gold Nanoparticle Assemblies Using Cucurbit[n]uril “Glue”. *ACS Nano*, 5(5):3878–3887, May 2011.
- [117] Oliver Benson. Assembly of hybrid photonic architectures from nanophotonic constituents. *Nature*, 480(7376):193–199, December 2011.

- [118] S. K. Kufer, E. M. Puchner, H. Gump, T. Liedl, and H. E. Gaub. Single-Molecule Cut-and-Paste Surface Assembly. *Science*, 319(5863):594–596, February 2008.
- [119] Madhavi Krishnan, Nassiredin Mojarad, Philipp Kukura, and Vahid Sandoghdar. Geometry-induced electrostatic trapping of nanometric objects in a fluid. *Nature*, 467(7316):692–695, October 2010.
- [120] Min Hu, Fung Suong Ou, Wei Wu, Ivan Naumov, Xuema Li, Alexander M. Bratkovsky, R. Stanley Williams, and Zhiyong Li. Gold Nanofingers for Molecule Trapping and Detection. *Journal of the American Chemical Society*, 132(37):12820–12822, September 2010.
- [121] Yuanhui Zheng, Alexander H. Soeriyadi, Lorenzo Rosa, Soon Hock Ng, Udo Bach, and J. Justin Gooding. Reversible gating of smart plasmonic molecular traps using thermoresponsive polymers for single-molecule detection. *Nature Communications*, 6:8797, November 2015.
- [122] Ramon A. Alvarez-Puebla, Rafael Contreras-Caceres, Isabel Pastoriza-Santos, Jorge Perez-Juste, and Luis M. Liz-Marzan. Au@pNIPAM Colloids as Molecular Traps for Surface-Enhanced, Spectroscopic, Ultra-Sensitive Analysis. *Angewandte Chemie International Edition*, 48(1):138–143, January 2009.
- [123] Nadrian C. Seeman. Nucleic acid junctions and lattices. *Journal of Theoretical Biology*, 99(2):237–247, November 1982.
- [124] Junghuei Chen and Nadrian C. Seeman. Synthesis from DNA of a molecule with the connectivity of a cube. *Nature*, 350(6319):631–633, April 1991.
- [125] Paul W. K. Rothmund. Folding DNA to create nanoscale shapes and patterns. *Nature*, 440(7082):297–302, March 2006.
- [126] Ebbe S. Andersen, Mingdong Dong, Morten M. Nielsen, Kasper Jahn, Ramesh Subramani, Wael Mamdouh, Monika M. Golas, Bjoern Sander, Holger Stark, Cristiano L. P. Oliveira, Jan Skov Pedersen, Victoria Birkedal, Flemming Besenbacher, Kurt V. Gothelf, and Jørgen Kjems. Self-assembly of a nanoscale DNA box with a controllable lid. *Nature*, 459(7243):73–76, May 2009.
- [127] Ryan J. Kershner, Luisa D. Bozano, Christine M. Micheel, Albert M. Hung, Ann R. Fornof, Jennifer N. Cha, Charles T. Rettner, Marco Bersani, Jane Frommer, Paul W. K. Rothmund, and Gregory M. Wallraff. Placement and orientation of individual DNA shapes on lithographically patterned surfaces. *Nature Nanotechnology*,

- 4(9):557–561, September 2009.
- [128] Albert M. Hung, Christine M. Micheel, Luisa D. Bozano, Lucas W. Osterbur, Greg M. Wallraff, and Jennifer N. Cha. Large-area spatially ordered arrays of gold nanoparticles directed by lithographically confined DNA origami. *Nature Nanotechnology*, 5(2):121–126, February 2010.
- [129] Thomas Topping, Niels V. Voigt, Jeanette Nangreave, Hao Yan, and Kurt V. Gothelf. DNA origami: a quantum leap for self-assembly of complex structures. *Chemical Society Reviews*, 40(12):5636–5646, 2011.
- [130] Niels V. Voigt, Thomas Topping, Alexandru Rotaru, Mikkel F. Jacobsen, Jens B. Ravnsbak, Ramesh Subramani, Wael Mamdouh, Jorgen Kjems, Andriy Mokhir, Flemming Besenbacher, and Kurt Vestreger Gothelf. Single-molecule chemical reactions on DNA origami. *Nature Nanotechnology*, 5(3):200–203, March 2010.
- [131] Ashwin Gopinath, Evan Miyazono, Andrei Faraon, and Paul W. K. Rothemund. Engineering and mapping nanocavity emission via precision placement of DNA origami. *Nature*, 535(7612):401–405, July 2016.
- [132] Yonggang Ke, Stuart Lindsay, Yung Chang, Yan Liu, and Hao Yan. Self-Assembled Water-Soluble Nucleic Acid Probe Tiles for Label-Free RNA Hybridization Assays. *Science*, 319(5860):180–183, January 2008.
- [133] G. P. Acuna, F. M. Moller, P. Holzmeister, S. Beater, B. Lalkens, and P. Tinnefeld. Fluorescence Enhancement at Docking Sites of DNA-Directed Self-Assembled Nanoantennas. *Science*, 338(6106):506–510, October 2012.
- [134] Phil Holzmeister, Enrico Pibiri, Jurgen J. Schmied, Tapasi Sen, Guillermo P. Acuna, and Philip Tinnefeld. Quantum yield and excitation rate of single molecules close to metallic nanostructures. *Nature Communications*, 5:5356, November 2014.
- [135] Sabrina Simoncelli, Eva-Maria Roller, Patrick Urban, Robert Schreiber, Andrew J. Turberfield, Tim Liedl, and Theobald Lohmuller. Quantitative Single-Molecule Surface-Enhanced Raman Scattering by Optothermal Tuning of DNA Origami-Assembled Plasmonic Nanoantennas. *ACS nano*, 10(11):9809–9815, 2016.
- [136] Jesica V. Pellegrotti, Guillermo P. Acuna, Anastasiya Puchkova, Phil Holzmeister, Andreas Gietl, Birka Lalkens, Fernando D. Stefani, and Philip Tinnefeld. Controlled Reduction of Photobleaching in DNA Origami-Gold Nanoparticle Hybrids. *Nano Letters*, 14(5):2831–2836, May 2014.

- [137] Sebastien Bidault, Alexis Devilez, Vincent Maillard, Laurent Lermusiaux, Jean-Michel Guigner, Nicolas Bonod, and Jerome Wenger. Picosecond Lifetimes with High Quantum Yields from Single-Photon-Emitting Colloidal Nanostructures at Room Temperature. *ACS Nano*, 10(4):4806–4815, April 2016.
- [138] Shawn M. Douglas, Adam H. Marblestone, Surat Teerapittayanon, Alejandro Vazquez, George M. Church, and William M. Shih. Rapid prototyping of 3d DNA-origami shapes with caDNAo. *Nucleic Acids Research*, 37(15):5001–5006, August 2009.
- [139] Nicholas A. W. Bell, Christian. R. Engst, Marc Ablay, Giorgio Divitini, Caterina Ducati, Tim Liedl, and Ulrich F. Keyser. DNA Origami Nanopores. *Nano Letters*, 12(1):512–517, January 2012.
- [140] Alexandros Emboras, Jens Niegemann, Ping Ma, Christian Haffner, Andreas Pedersen, Mathieu Luisier, Christian Hafner, Thomas Schimmel, and Juerg Leuthold. Atomic Scale Plasmonic Switch. *Nano Letters*, 16(1):709–714, January 2016.
- [141] Martin Kuttge, Wei Cai, F. Javier Garcia de Abajo, and Albert Polman. Dispersion of metal-insulator-metal plasmon polaritons probed by cathodoluminescence imaging spectroscopy. *Physical Review B*, 80(3):033409, July 2009.
- [142] Sergey I. Bozhevolnyi and Thomas Sondergaard. General properties of slow-plasmon resonant nanostructures: nano-antennas and resonators. *Optics Express*, 15(17):10869–10877, August 2007.
- [143] Ewold Verhagen, Jennifer A. Dionne, L. (Kobus) Kuipers, Harry A. Atwater, and Albert Polman. Near-Field Visualization of Strongly Confined Surface Plasmon Polaritons in Metal-Insulator-Metal Waveguides. *Nano Letters*, 8(9):2925–2929, September 2008.
- [144] EN Economou. Surface plasmons in thin films. *Physical review*, 182(2):539, 1969.
- [145] Hideki T Miyazaki and Yoichi Kurokawa. Squeezing visible light waves into a 3-nm-thick and 55-nm-long plasmon cavity. *Physical review letters*, 96(9):097401, 2006.
- [146] Yoichi Kurokawa and Hideki T Miyazaki. Metal-insulator-metal plasmon nanocavities: Analysis of optical properties. *Physical Review B*, 75(3):035411, 2007.
- [147] JA Dionne, LA Sweatlock, HA Atwater, and A Polman. Plasmon slot waveguides: Towards chip-scale propagation with subwavelength-scale localization. *Physical Review B*, 73(3):035407, 2006.

- [148] J. Mertens, A. Demetriadou, R. W. Bowman, F. Benz, M.-E. Kleemann, C. Tserkezis, Y. Shi, H. Y. Yang, O. Hess, J. Aizpurua, and J. J. Baumberg. Tracking Optical Welding through Groove Modes in Plasmonic Nanocavities. *Nano Letters*, 16(9):5605–5611, September 2016.
- [149] Rohit Chikkaraddy, Bart de Nijs, Felix Benz, Steven J. Barrow, Oren A. Scherman, Ortwin Hess, and Jeremy J. Baumberg. Single-molecule Rabi oscillations with single plasmonic nanocavity resonance at room temperature. Gordon Research Conference: Plasmonics and Nanophotonics, Newry ME, USA, 2016.
- [150] J Britt Lassiter, Felicia McGuire, Jack J Mock, Cristian Ciraci, Ryan T Hill, Benjamin J Wiley, Ashutosh Chilkoti, and David R Smith. Plasmonic waveguide modes of film-coupled metallic nanocubes. *Nano letters*, 13(12):5866–5872, 2013.
- [151] F. J. Garc a de Abajo and A. Howie. Retarded field calculation of electron energy loss in inhomogeneous dielectrics. *Physical Review B*, 65(11):115418, March 2002.
- [152] Ulrich Hohenester. Simulating electron energy loss spectroscopy with the MNPBEM toolbox. *Computer Physics Communications*, 185(3):1177–1187, March 2014.
- [153] Ulrich Hohenester and Andreas Trugler. Mnpbem â a matlab toolbox for the simulation of plasmonic nanoparticles. *Computer Physics Communications*, 183(2):370–381, February 2012.
- [154] Jurgen Waxenegger, Andreas Trugler, and Ulrich Hohenester. Plasmonics simulations with the MNPBEM toolbox: Consideration of substrates and layer structures. *Computer Physics Communications*, 193:138–150, August 2015.
- [155] G. A. E. Vandenbosch and A. R. Van de Capelle. Mixed-potential integral expression formulation of the electric field in a stratified dielectric medium-application to the case of a probe current source. *IEEE Transactions on Antennas and Propagation*, 40(7):806–817, July 1992.
- [156] X. Zheng, N. Verellen, D. Vercruyse, V. Volskiy, P. Van Dorpe, G. A. E. Vandenbosch, and V. Moshchalkov. On the Use of Group Theory in Understanding the Optical Response of a Nanoantenna. *IEEE Transactions on Antennas and Propagation*, 63(4):1589–1602, April 2015.
- [157] Anna Lombardi, Angela Demetriadou, Lee Weller, Patrick Andrae, Felix Benz, Rohit Chikkaraddy, Javier Aizpurua, and Jeremy J. Baumberg. Anomalous Spectral Shift of Near- and Far-Field Plasmonic Resonances in Nanogaps. *ACS Photonics*, 3(3):471–

- 477, March 2016.
- [158] Antoine Moreau, Cristian Ciraci, Jack J Mock, Ryan T Hill, Qiang Wang, Benjamin J Wiley, Ashutosh Chilkoti, and David R Smith. Controlled-reflectance surfaces with film-coupled colloidal nanoantennas. *Nature*, 492(7427):86–89, 2012.
- [159] Marie-Elena Kleemann, Jan Mertens, Xuezhi Zheng, Sean Cormier, Vladimir Turek, Felix Benz, Rohit Chikkaraddy, William Deacon, Anna Lombardi, Victor V. Moshchalkov, Guy A. E. Vandenbosch, and Jeremy J. Baumberg. Revealing Nanostructures through Plasmon Polarimetry. *ACS Nano*, 11(1):850–855, January 2017.
- [160] Felix Benz, Bart de Nijs, Christos Tserkezis, Rohit Chikkaraddy, Daniel O. Sigle, Laurynas Pukenas, Stephen D. Evans, Javier Aizpurua, and Jeremy J. Baumberg. Generalized circuit model for coupled plasmonic systems. *Optics Express*, 23(26):33255, December 2015.
- [161] W. E. Moerner. A Dozen Years of Single-Molecule Spectroscopy in Physics, Chemistry, and Biophysics. *The Journal of Physical Chemistry B*, 106(5):910–927, February 2002.
- [162] Florian Kulzer and Michel Orrit. Single-molecule optics. *Annual Review of Physical Chemistry*, 55(1):585–611, April 2004.
- [163] Lukas Novotny and Bert Hecht. *Principles of nano-optics*. Cambridge university press, 2012.
- [164] Eric Le Ru and Pablo Etchegoin. *Principles of Surface-Enhanced Raman Spectroscopy: and related plasmonic effects*. Elsevier, 2008.
- [165] Ricardo Aroca. Surface-Enhanced Raman Scattering. In *Surface-Enhanced Vibrational Spectroscopy*, pages 73–106. John Wiley & Sons, Ltd, 2006. DOI: 10.1002/9780470035641.ch3.
- [166] C. V. Raman. A new radiation [Reproduced from Indian J. Phys., 1928, 2, 387–398]. *Current Science*, 74(4):382–386, 1998.
- [167] C.V. Raman and K. S. Krishnan. A New Type of Secondary Radiation. *Nature*, 121:501–502.
- [168] M. Fleischmann, P. J. Hendra, and A. J. McQuillan. Raman spectra of pyridine adsorbed at a silver electrode. *Chemical Physics Letters*, 26(2):163–166, May 1974.

- [169] A. James McQuillan. The discovery of surface-enhanced Raman scattering. *Notes and Records*, 63(1):105–109, March 2009.
- [170] Eric C. Le Ru and Pablo G. Etchegoin. Single-Molecule Surface-Enhanced Raman Spectroscopy. *Annual Review of Physical Chemistry*, 63(1):65–87, 2012.
- [171] Eric C. Le Ru and Pablo G. Etchegoin. Quantifying SERS enhancements. *MRS Bulletin*, 38(08):631–640, August 2013.
- [172] Pablo G. Etchegoin, Eric C. Le Ru, and A. Fainstein. Bi-analyte single molecule SERS technique with simultaneous spatial resolution. *Physical Chemistry Chemical Physics*, 13(10):4500–4506, February 2011.
- [173] E. C. Le Ru, M. Meyer, and P. G. Etchegoin. Proof of Single-Molecule Sensitivity in Surface Enhanced Raman Scattering (SERS) by Means of a Two-Analyte Technique. *The Journal of Physical Chemistry B*, 110(4):1944–1948, February 2006.
- [174] Felix Benz, Mikolaj K. Schmidt, Alexander Dreismann, Rohit Chikkaraddy, Yao Zhang, Angela Demetriadou, Cloudy Carnegie, Hamid Ohadi, Bart de Nijs, Ruben Esteban, Javier Aizpurua, and Jeremy J. Baumberg. Single-molecule optomechanics in âpicocavitiesâ. *Science*, 354(6313):726–729, November 2016.
- [175] K. Hennessy, A. Badolato, M. Winger, D. Gerace, M. Atature, S. Gulde, S. Falt, E. L. Hu, and A. Imamoglu. Quantum nature of a strongly coupled single quantum dot cavity system. *Nature*, 445(7130):896–899, February 2007.
- [176] Hong-Gyu Park, Carl J. Barrelet, Yongning Wu, Bozhi Tian, Fang Qian, and Charles M. Lieber. A wavelength-selective photonic-crystal waveguide coupled to a nanowire light source. *Nature Photonics*, 2(10):622–626, October 2008.
- [177] Ryan T. Hill, Jack J. Mock, Angus Hucknall, Scott D. Wolter, Nan M. Jokerst, David R. Smith, and Ashutosh Chilkoti. Plasmon Ruler with Angstrom Length Resolution. *ACS Nano*, 6(10):9237–9246, October 2012.
- [178] Vivek V. Thacker, Lars O. Herrmann, Daniel O. Sigle, Tao Zhang, Tim Liedl, Jeremy J. Baumberg, and Ulrich F. Keyser. DNA origami based assembly of gold nanoparticle dimers for surface-enhanced Raman scattering. *Nature Communications*, 5:ncomms4448, March 2014.
- [179] Simone De Liberato. Light-Matter Decoupling in the Deep Strong Coupling Regime: The Breakdown of the Purcell Effect. *Physical Review Letters*, 112(1):016401, January 2014.

- [180] Mickael P. Busson and Sebastien Bidault. Selective Excitation of Single Molecules Coupled to the Bright Mode of a Plasmonic Cavity. *Nano Letters*, 14(1):284–288, January 2014.
- [181] Carolin Vietz, Izabela Kaminska, Maria Sanz Paz, Philip Tinnefeld, and Guillermo P. Acuna. Broadband Fluorescence Enhancement with Self-Assembled Silver Nanoparticle Optical Antennas. *ACS Nano*, 11(5):4969–4975, May 2017.
- [182] Jan Mertens, Marie-Elena Kleemann, Rohit Chikkaraddy, Prineha Narang, and Jeremy J. Baumberg. How Light Is Emitted by Plasmonic Metals. *Nano Letters*, 17(4):2568–2574, April 2017.
- [183] James T. Hugall and Jeremy J. Baumberg. Demonstrating Photoluminescence from Au is Electronic Inelastic Light Scattering of a Plasmonic Metal: The Origin of SERS Backgrounds. *Nano Letters*, 15(4):2600–2604, April 2015.
- [184] Roger B. Altman, Daniel S. Terry, Zhou Zhou, Qinsi Zheng, Peter Geggier, Rachel A. Kolster, Yongfang Zhao, Jonathan A. Javitch, J. David Warren, and Scott C. Blanchard. Cyanine fluorophore derivatives with enhanced photostability. *Nature Methods*, 9(1):68–71, January 2012.
- [185] Emilie Wientjes, Jan Renger, Richard Cogdell, and Niek F. van Hulst. Pushing the Photon Limit: Nanoantennas Increase Maximal Photon Stream and Total Photon Number. *The Journal of Physical Chemistry Letters*, 7(9):1604–1609, May 2016.
- [186] Ute Resch-Genger, Markus Grabolle, Sara Cavaliere-Jaricot, Roland Nitschke, and Thomas Nann. Quantum dots versus organic dyes as fluorescent labels. *Nature Methods*, 5(9):763–775, September 2008.
- [187] Patryk Kusch, Stefan Mastel, Niclas S. Mueller, Nieves Morquillas Azpiazu, Sebastian Heeg, Roman Gorbachev, Fredrik Schedin, Uwe Hubner, Jose I. Pascual, Stephanie Reich, and Rainer Hillenbrand. Dual-Scattering Near-Field Microscope for Correlative Nanoimaging of SERS and Electromagnetic Hotspots. *Nano Letters*, 17(4):2667–2673, April 2017.
- [188] N. Rotenberg and L. Kuipers. Mapping nanoscale light fields. *Nature Photonics*, 8(12):919–926, December 2014.
- [189] A Femius Koenderink, Andrea Alù, and Albert Polman. Nanophotonics: Shrinking light-based technology. *Science*, 348(6234):516–521, 2015.



- 
- [190] Yoshiya Sato, Yoshinori Tanaka, Jeremy Upham, Yasushi Takahashi, Takashi Asano, and Susumu Noda. Strong coupling between distant photonic nanocavities and its dynamic control. *Nature Photonics*, 6(1):56–61, January 2012.
- [191] Xiaoze Liu, Tal Galfsky, Zheng Sun, Fengnian Xia, Erh-chen Lin, Yi-Hsien Lee, Stephane Kena-Cohen, and Vinod M. Menon. Strong light-matter coupling in two-dimensional atomic crystals. *Nature Photonics*, 9(1):30–34, January 2015.
- [192] J. D. Thompson, T. G. Tiecke, N. P. de Leon, J. Feist, A. V. Akimov, M. Gullans, A. S. Zibrov, V. Vuletić, and M. D. Lukin. Coupling a Single Trapped Atom to a Nanoscale Optical Cavity. *Science*, 340(6137):1202–1205, June 2013.
- [193] Andrei Faraon, Ilya Fushman, Dirk Englund, Nick Stoltz, Pierre Petroff, and Jelena Vučković. Coherent generation of non-classical light on a chip via photon-induced tunnelling and blockade. *Nature Physics*, 4(11):859–863, November 2008.
- [194] Simon Groblacher, Tomasz Paterek, Rainer Kaltenbaek, Caslav Brukner, Marek Zukowski, Markus Aspelmeyer, and Anton Zeilinger. An experimental test of non-local realism. *Nature*, 446(7138):871–875, April 2007.
- [195] David M. Coles, Yanshen Yang, Yaya Wang, Richard T. Grant, Robert A. Taylor, Semion K. Saikin, Alan Aspuru-Guzik, David G. Lidzey, Joseph Kuo-Hsiang Tang, and Jason M. Smith. Strong coupling between chlorosomes of photosynthetic bacteria and a confined optical cavity mode. *Nature Communications*, 5, November 2014.
- [196] A. Shalabney, J. George, J. Hutchison, G. Pupillo, C. Genet, and T. W. Ebbesen. Coherent coupling of molecular resonators with a microcavity mode. *Nature Communications*, 6, January 2015.
- [197] Felix Benz, Christos Tserkezis, Lars O. Herrmann, Bart de Nijs, Alan Sanders, Daniel O. Sigle, Laurynas Pukenas, Stephen D. Evans, Javier Aizpurua, and Jeremy J. Baumberg. Nanooptics of Molecular-Shunted Plasmonic Nanojunctions. *Nano Letters*, 15(1):669–674, January 2015.
- [198] Setu Kasera, Frank Biedermann, Jeremy J. Baumberg, Oren A. Scherman, and Sumeet Mahajan. Quantitative SERS Using the Sequestration of Small Molecules Inside Precise Plasmonic Nanoconstructs. *Nano Letters*, 12(11):5924–5928, November 2012.

- [199] Setu Kasera, Lars O. Herrmann, Jesus del Barrio, Jeremy J. Baumberg, and Oren A. Scherman. Quantitative multiplexing with nano-self-assemblies in SERS. *Scientific Reports*, 4, October 2014.
- [200] Falko P. Netzer and Michael G. Ramsey. Structure and orientation of organic molecules on metal surfaces. *Critical Reviews in Solid State and Materials Sciences*, 17(5):397–475, January 1992.
- [201] Vasily Kravtsov, Samuel Berweger, Joanna M. Atkin, and Markus B. Raschke. Control of Plasmon Emission and Dynamics at the Transition from Classical to Quantum Coupling. *Nano Letters*, 14(9):5270–5275, September 2014.
- [202] James A. Hutchison, Tal Schwartz, Cyriaque Genet, Eloise Devaux, and Thomas W. Ebbesen. Modifying Chemical Landscapes by Coupling to Vacuum Fields. *Angewandte Chemie International Edition*, 51(7):1592–1596, 2012.
- [203] Javier Galego, Francisco J. Garcia-Vidal, and Johannes Feist. Cavity-induced modifications of molecular structure in the strong coupling regime. *arXiv:1506.03331 [physics, physics:quant-ph]*, June 2015. arXiv: 1506.03331.
- [204] Johannes Feist and Francisco J. Garcia-Vidal. Extraordinary exciton conductance induced by strong coupling. *Physical Review Letters*, 114(19), May 2015. arXiv: 1409.2514.
- [205] Mark L Brongersma and Vladimir M Shalaev. The case for plasmonics. *Science*, 328(5977):440–441, 2010.
- [206] Sergey I Bozhevolnyi and Jacob B Khurgin. The case for quantum plasmonics. *Nature Photonics*, 11(7):398–400, 2017.
- [207] Johannes Feist, Javier Galego, and Francisco J Garcia-Vidal. Polaritonic chemistry with organic molecules. *ACS Photonics*, 2017.
- [208] Javier Galego, Francisco J. Garcia-Vidal, and Johannes Feist. Many-molecule reaction triggered by a single photon in polaritonic chemistry. *Phys. Rev. Lett.*, 119:136001, Sep 2017.
- [209] Javier Galego, Francisco J Garcia-Vidal, and Johannes Feist. Suppressing photochemical reactions with quantized light fields. *Nature communications*, 7, 2016.